# WIND-WAVE MEASUREMENTS IN A SHALLOW ESTUARY: TRINITY BAY, TEXAS

A Thesis

by

KEITH WADE DUPUIS

Submitted to the Office of Graduate Studies of
Texas A&M University
in partial fulfillment of the requirements for the degree of

MASTER OF SCIENCE

December 2006

Major Subject: Oceanography

# WIND-WAVE MEASUREMENTS IN A SHALLOW ESTUARY: TRINITY BAY, TEXAS

A Thesis

by

KEITH WADE DUPUIS

Submitted to the Office of Graduate Studies of
Texas A&M University
in partial fulfillment of the requirements for the degree of

MASTER OF SCIENCE

Approved by:

| | |
|---|---|
| Chair of Committee, | Ayal Anis |
| Committee Members, | Achim Stössel |
| | John Sweetman |
| Head of Department, | Robert Stickney |

December 2006

Major Subject: Oceanography

# ABSTRACT

Wind-Wave Measurements in a Shallow Estuary: Trinity Bay, Texas. (December 2006)

Keith Wade Dupuis, B.S., Texas A&M University at Galveston

Chair of Advisory Committee: Dr. Ayal Anis

Acoustic current meter data collected in the shallow ( 3m depth) Trinity Bay, (TB a sub-bay in Galveston Bay), TX, estuary were used to characterize locally generated wind-waves. Significant wave heights, periods, and directions were estimated from dynamic pressure time-series (P; near bottom) and horizontal current velocities (U, V). Surface wave spectra were calculated from the pressure time-series and fitted to the empirical shallow-water Texel, Marsen, and Arsloe wave spectrum. The mean shape parameters used to define the TB wave spectra were:$\alpha = 0.016$, $\gamma = 4.26$, $\sigma_a = 0.063$, $\sigma_b = 0.089$. Waves heights were also hindcast using empirical and numerical models. The empirical formulas were derived from fetch-limited shallow water observations and follow the current proposed asymptotic limit to wave growth in shallow depth. The depth range for this empirical formulation is extended from 0.5–2m out to 3.5m. The model does not work for wind speeds less than 1m/s and during rapid wind direction changes.

The Shallow WAves Nearshore numerical model was implemented in a Galveston Bay (GB; encompassing TB) computational domain. The model was forced with wind speeds and directions measured on-site and in four surrounding locations maintained by the NOAA PORTS. Currents measured on-site in TB and calculated bottom frictions were input homogeneously in space. The model was run in steady and unsteady conditions, and the modeled wave spectra were compared to the observations. The modeled wave spectra do not recreate the observed spectral shape for the steady and unsteady conditions. However, the total wave energy is represented in the unsteady conditions. In both the steady and unsteady cases, the wave period is underpredicted by one-half times the observed spectra and the model direction agrees with the observed wave directions.

# TABLE OF CONTENTS

Page

# LIST OF TABLES

# LIST OF FIGURES

FIGURE Page

FIGURE Page

# 1. INTRODUCTION

Waves in the ocean are a ubiquitous phenomenon spanning a large temporal and spatial range from small ripples to earthquake induced tsunamis and gravity induced tides. In the presence of wind, waves form from a suite of air-sea interactions and are called wind-waves. The ability to observe and forecast wind-waves is necessary in a wide field of applications: coastal and offshore engineering design, sediment transport models, biogeochemical nutrient modeling and turbulence modeling. These practical needs have led to observational studies using classic and innovative ocean observing technology to characterize wind-waves. In general, the task of observing and measuring wind-waves is unique and difficult because the objective is to measure a random constantly moving surface with, historically, the observer right on top. Aside from the sea-fareing observer, a wide assortment of wave measuring instruments have been developed. Examples include moored-floating devices (wire-gages, heave-pitch and roll buoys), bottom-mounted in-situ current meters and remote sensing instruments (land-based HF radar, and space orbiting satellites).

Oceans and enclosed shallow intertidal bodies of water with proper wind conditions (i.e. fetch and duration) will develop local wind-waves. This is opposed to swell, also generated by the wind, which is no longer in the presence of generating forces (wind). Swell can travel long distances away from its source of generation. The work presented in this manuscript is concerned with locally generated wind-waves and their energy propogating through the water column. It is this energy that impacts coastal and offshore structures, influences bottom boundary layers, effectively transports sediments and disperses chemicals and nutrients (either in sediment or in the water column). Forecasts and general knowledge of wind-waves in specific locations are important, and it is the details of the surface forcing

---

This thesis follows the style and format of the *Journal of Physical Oceanography.*

(e.g. wind) and the resulting wave energy that is most sought after in observational studies.

The physical processes governing shallow water wind-waves in unsteady conditions (i.e. changing winds, currents, tides) is actively researched through combined observational and modeling approaches (Gorman and Neilson, 1999; Smith, et al., 2001; Jin and Ji, 2001; Bottema, et al., 2002; Lin, et al., 2002; Rogers, et al., 2003; Chen, et al. 2005.) The work presented in this manuscript follows this approach to describe wind-waves in a shallow estuary under quasi-steady conditions. An introduction to previous wind-wave observations, the motivation and field site are presented in the following subsections followed by a description of the experimental methods and the data analysis methods in Section 2. The obervations and hindcast results from an empirical model are presented in Section 3. The Simulating WAves Nearshore (SWAN) model is briefly introduced followed by model hindcasts during steady wind directions are presented in section 4. Conclusions are presented in section 5.

### *a. Previous Wave Observations*

The state-of-the-art instruments used to observe wind-waves generally measure a representative parameter of the sea surface elevation as a function of time. The wind-wave sea-surface time-series are random, requiring statistical tools for their analysis. The wave spectrum is the most widely used and accepted tool used to study wind-waves. Assuming that the random sea-surface is composed of many different wave components in time and space, the wave spectrum represents a decomposition of these components into specific frequency and direction bands. This is similar to white light decomposed into different wavelengths/colors. A directional frequency power spectrum, $\mathrm{F}(f, \theta)$, is thus obtained and in short yields the wave energy and its direction of propagation, $\theta$, for a specific frequency,

$f[Hz]$. This is presented as a product of the sea-surface variance spectrum, $E(f, x, d)$, and a directional spreading function, D($f$, $\theta$):

$$F(f, \theta) = E(f, U, x, d) D(f, \theta), \tag{1}$$

where

$$\int_0^{2\pi} D(f, \theta) dx = 1. \tag{2}$$

and $U[m/s]$ is wind speed, $x$ is the fetch length $[m]$ and $d$ is depth $[m]$.

Empirical spectral models have been developed to conform to observational spectra from parameters such as wind speed, fetch and wave height. Wave spectra characteristic of a specific location are useful aids in the design of coastal and offshore structures (Chakrabarti, 1987). The development of common operational spectra used in Oceanography and Ocean Engineering is credited to Phillips' (1958) work applied to fully-developed wind-waves. Phillips' proposed an asymptotic limit to the shape of the high-frequency spectral tail (the region of the wave spectrum beyond the spectral peak) on the assumption that dissipation of wave energy through white-capping of sharp wave crests occurs in the high-frequency region. In other words, he proposed that regions of the wave spectra are separated into generation and dissipation processes (Kitaigorodskii, 1983). The physical process of whitecapping is no longer subject to viscous forces, and the acceleration of gravity is assumed the only significant physical parameter (Phillips,1958). Based on dimensional arguments Phillips proposed a power-law form for the high-frequency spectral tail:

$$E_P = \alpha g^2 (2\pi)^{-4} f^n, \tag{3}$$

where $g[\mathrm{m}^2\mathrm{s}^{-1}]$ is the acceleration due to gravitaty and the constants $\alpha = 8 \times 10^{-3}$ and $n = -5$. Equation 3 was verified from observational data (Phillips, 1958; Burling,1959;

Kinsman,1960).Since 1958, newer observational experiments found the high-frequency spectral tail to vary between $-3.5 < n < -5$ (Kitaigorodskii et al. 1975; Mitsuyasu et al.,1975; Forristal, 1981; Donelan et al.,1985; Knowles,1985).

Further work aimed at describing wave frequency spectra are the result of the self-similar theory applied to wind-waves. The theory utilizes non-dimensional parameters relevant to the physical processes of concern. When plotted appropriately, non-dimensionalized quanitities will yield a similar shape. This is useful when comparing different conditions. Application of self-similar theory to wind-wave analysis was first proposed by Kitaigorodskii (1962). This method has since been used to compare both deep and shallow water wave spectra for a variety of wind speeds and fetch lengths. The relevant non-dimensionalized quantities used in this manuscript are summarized as:

- non-dimensional energy $\epsilon = g^2 \frac{E}{U^4}$
- non-dimensional frequency $\nu = f_p \frac{U}{g}$
- non-dimensional fetches $\chi = g \frac{x}{U^2}$
- non-dimensional depth $\delta = g \frac{d}{U^2}$

where $E$ is the wave energy $[m^2 s]$, $f_p$ is the frequency of the spectral peak and $U = U_{10}$ is the wind-speed adjusted to a height of 10 m. The non-dimensional forms developed from relationships between Kitaigorodskii's parameters have evolved into operational wave spectra. As a necessary background, the landmark proposals of specific spectral forms are briefly described in the following sections.

### *Pierson Moskowitz Spectrum*

Pierson and Moskowitz (PM,1964) proposed a spectral form based on the application of self-similar theory to wave analysis. The PM spectral form is presented in Equation 4 and follows Phillips' (1958) $f^{-5}$ spectral tail for "fully-developed" waves that are fetch-independant. In other words, a steady wind was blowing over a fixed fetch for a duration such that the wave energy reaches a state of equilibrium, where wave generation is balanced by dissipation due to whitecapping and breaking:

$$\Phi_{PM} = E_P \exp\left[-\beta\left(\frac{f}{f_p}\right)^{-4}\right], \tag{4}$$

where $E_p$ is the Phillips equilibrium range given in (3).

### *JONSWAP*

The JONSWAP wave spectrum represents actively growing wind-waves in the deep ocean. It is a modification of the PM spectrum and combines the PM fully-developed spectral form, ($\Phi_{PM}$), and the JONSWAP peak shape function, ($\Phi_J$) derived from observations in the North Sea. The JONSWAP frequency spectra is expressed as:

$$F(f) = \Phi_{PM}\Phi_J, \tag{5}$$

where

$$\Phi_J = \gamma \exp\frac{-(f-f_p)^2}{2\sigma^2 f_p^2}, \tag{6}$$

and $\gamma = 3.3$, $\sigma = 0.07$ for $f \leq f_p$ and $\sigma = 0.09$ for $f > f_p$ are constants. The constant $\alpha$ (in 3) was determined to vary as a function of the non-dimensional fetch ($\chi$).

### *TMA*

Bouws et al. (1985) proposed the TMA shallow water spectral shape. In their spectral formulation, Bouws et al. (1985) modify the JONSWAP spectral form by adding a depth ($h$) and frequency ($\omega$) dependant “reduction” factor, $\Theta\left(\omega,h\right)$, proposed by Kitaigorodskii et al. (1975). The TMA spectra is named after the Texel (Dutch North Sea), Marsen (German Bight) and Arsloe (US East Coast) data sets used to verify this shallow water wave spectra, and is given by:

$$F(f)=\Phi_J\Theta \tag{7}$$

where

$$\Theta=\kappa^{-2}\left[1+2\omega_h^2\frac{\kappa}{\sinh(2\omega_h^2\kappa)}\right]^{-1} \tag{8}$$

and $\omega_h=2\pi f\left(\frac{h}{g}\right)^{\frac{1}{2}}$. $\kappa$ is solved from $\kappa\tanh(\omega_h^2\kappa)=1$.

### *b. Field Site*

Galveston Bay (Fig.1), located in the Texas Gulf Coast, is a large subtropical shallow estuary with a surface area of 1600 km$^2$. It is divided into four sub-bays: Galveston Bay (GB), Trinity Bay, East Bay, and West Bay. The mean depth of the bay is 3m and it has simple bathymetry with the exception of the dredged Houston Ship Channel (dark line in Fig. 1). The bay is intertidal (range: 0.5m) with three inlets to the Gulf of Mexico (GOM) and two sources of freshwater from the San Jacinto and Trinity Rivers, respectively. GB provides the largest commercial fisheries market for seafood in Texas and is influenced by surrounding petro-chemical production facilities, wastewater drainage from large Metropolitan cities (Houston, Dallas/Fort Worth), and large commercial and recreational fishing vessels. Within the GB system, Trinity Bay (TB) is an estuary with the primary source of freshwater from the Trinity River, and the primary source of saline waters from an inlet to the GOM. It included the rounded NE section of the bay. In this manuscript TB and GB are considered equivalent. There are also many oil and gas platforms located throughout the bay.

Wind and wave data were collected in GB. The sampling location was not exposed to waves generated in the GOM, and the Houston Ship Channel was far enough to prevent contamination from commercial ship wakes. Occasional wakes were produced by small recreational boats that passed nearby. The events were logged and not used in the analysis.

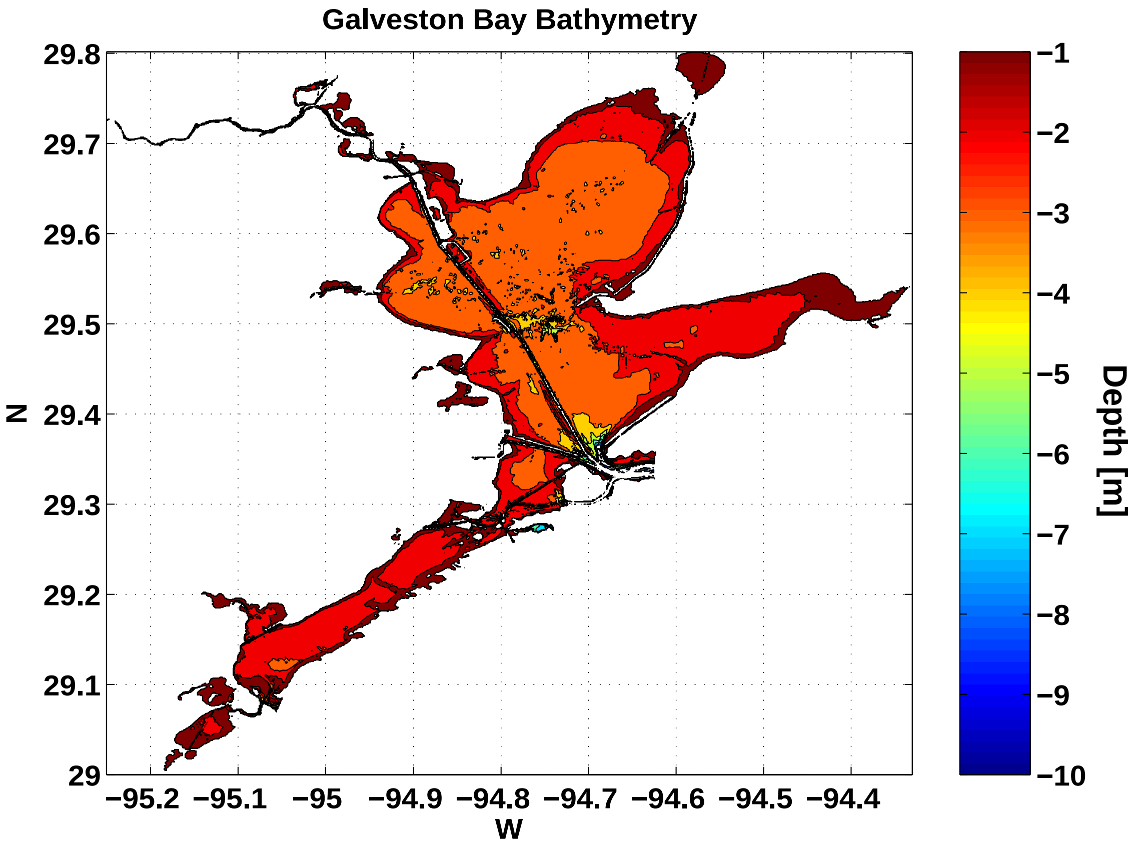

Fig. 1. Map of Galveston Bay with bathymetry contours. The mean depth of the bay is 3m except in the Houston Ship Channel (solid black line transecting the bay).

Table 1. List of cruise dates and number of 8.5 minute realizations of dynamic pressure and currents measured by the ADV and ADCP. The cruises were scheduled to coincide as close as possible to the neap or spring tidal cycle. These are listed in column five with the observed tidal range listed in column six.

| Date | Location | Number of ADV Spectra | Number of ADCP Spectra | Moon Phase | Water Level change [m] |
|---|---|---|---|---|---|
| 05-06, August 2004 | $29.641^o N$ $94.791^o W$ | 101 | 25 | Neap | 0.23 |
| 12-13, August 2004 | $29.640^o N$ $94.791^o W$ | 76 | 27 | Spring | 0.52 |
| 02-03, September 2004 | $29.628^o N$ $94.803^o W$ | 106 | 27 | Neap | 0.26 |
| 06-07, November 2004 | $29.629^o N$ $94.803^o W$ | 104 | 26 | Neap | 0.34 |
| 13-14, November 2004 | $29.627^o N$ $94.806^o W$ | 86 | 22 | Spring | 0.58 |
| 15-16, January 2005 | $29.628^o N$ $94.804^o W$ | 103 | 26 | Neap | 0.34 |
| 04-05, February 2005 | $29.616^o N$ $94.800^o W$ | 100 | 25 | Spring | 0.48 |
| 25-26, March 2005 | $29.630^o N$ $94.805^o W$ | 100 | 25 | Neap | 0.32 |
| 02-03, April 2005 | $29.631^o N$ $94.805^o W$ | 103 | 26 | Spring | 0.64 |
| 25-26, May 2005 | $29.632^o N$ $94.803^o W$ | 104 | 26 | Spring | 0.50 |

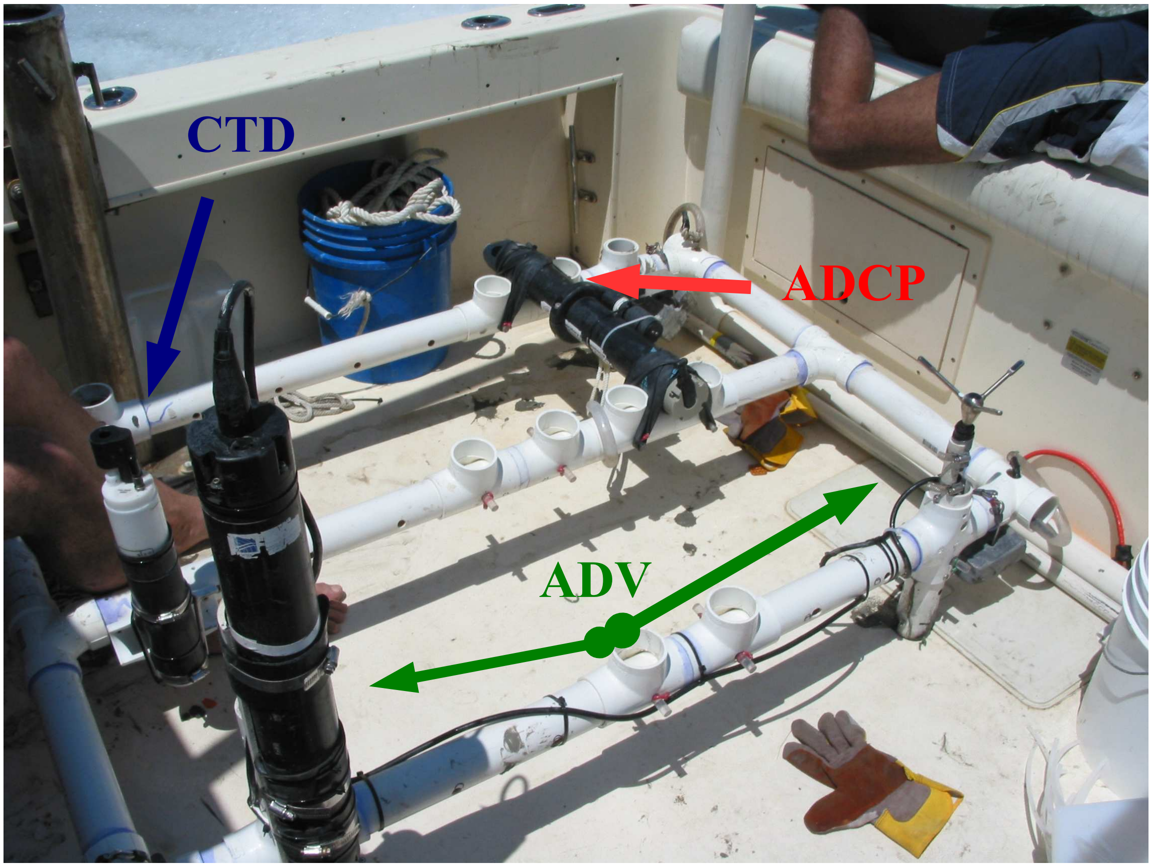

Fig. 2. Photograph of the PVC bottom pod with the two current meters (ADV and ADCP) and a mini-CTD (Conductivity-Temperature-Depth recorder). Care was taken to avoid contamination of the ADCP's and ADV's compass measurements and no magnetic materials were used in the pod's construction. 5 kg lead bricks, inserted into each of the pod's legs, assured it's stability when it was positioned on the bottom.

### *c. Motivation*

The experiment described in this manuscript follows a combined observational and model approach to describe wind-waves in a shallow estuary. It follows the general procedures outlined in recent shallow water experiments (e.g. Gorman and Neilson, 1999; Smith, et al., 2001; Jin and Ji, 2001; Bottema, et al.,2002; Lin, et al., 2002; Rogers, et al., 2003; Chen, et al. 2005.) The research carried out was funded to determine the relative energy contributions near the bottom-boundary layer due to currents (tidal and surface forced) and wind-waves. These processes are assumed to effectively transport nutrients bound within the GB bottom substrate. The results presented in this report allow for the determination of the energy near the bottom-bounday layer from surface wind-waves.

The results of this experiment are indirectly applicable to two current projects describing waves in GB. The first ia a marsh erosion project. The project investigator is designing an erosion resistant marsh in West Bay, and the relative contributions to sediment transport from tide-induced currents and wind-waves are important factors aiding their design (Ravens, 2006). The empirical model results presented in this thesis (Section 3c) are applicable for determining the wind-wave contribution to sediment transport in 0.5m depth.

The results of this project provide a second contribution to ongoing model research in GB. Forty-eight hour wave forecasts of significant wave height, peak period and wave direction are available online at the Texas A&M University at Galveston (TAMUG) Maritime Systems Engineering (MASE) website (MASE-SWAN). The model output covers the Gulf Coast off of Galveston Island and the entire GB system. Their model output has never been verified in GB. The observations from this experiment are the first comparison to the SWAN model output in GB. These are presented in Section 5.

# 2. DATA COLLECTION AND ANALYSIS

Current meter and wind observations were made at a single location on ten twenty-four hour cruises in Galveston Bay. The methods used to collect, estimate and analyze the wind-wave characteristics are described in the following sections.

## *a. Dynamic Pressure, $P$, and Orbital Wave Velocities, $U$ and $V$*

Dynamic pressure, $P$, and orbital wave velocities, $U$ and $V$ ($PUV$), were measured and recorded from two nearly collocated upward-looking acoustic current meters mounted on a bottom pod in Galveston Bay (Fig.2). The current meters used were an acoustic Doppler current profiler (ADCP; 1 MHz Aquadopp made by NortekAS) and an acoustic Doppler velocimeter (ADV; Vector made by NortekAS). The ADCP measures pressure and vertical profiles of water-currents at a maximum rate of 2Hz. The ADV samples pressure and 3-D currents at a single sampling volume at a maximum rate of 64 Hz. The current meters were deployed using the following sampling schemes:

- ADV - Sampled and recorded $PUV$ during 8.5-minute bursts at 32 Hz yielding 16,384 data points per burst. A burst occurred every 15 minutes. The sample volume is located 15mm above the instrument transducer. The pressure sensor range is 20 m with resolution of 0.005$\%$ and a minimum resolution equivalent to depth changes of 1 mm.

- ADCP - Sampled and recorded $PUV$ during 8.5-minute bursts at 2 Hz yielding 1024 data points per burst. A burst occurred every 60 minutes. The pressure sensor range is 50 m with a resolution of 0.005$\%$. The minimum range is equivalent to 2.5 mm depth change. While in burst mode, the ADCP sampled currents at 2.5m above the instrument. When the ADCP was not in burst mode it measured current profiles, with 15 bins 0.3m apart in the vertical, continuously at 1Hz. These were stored as 5 minute averages in the internal memory.

A mini-CTD (model XR-420 made by RBR), also mounted on the pod, measured pressure, conductivity, and temperature continuously at a rate of 1 Hz. The dates, sampling locations, tide phase (e.g. neap or sping) and observed tide changes are listed in Table - 1. The third and fourth columns represent the number of wave observations from each experiment.

Figure 3 shows time-history plots of depth [m] from all three pressure sensors for approximately twenty-four hours on 05-06 August 2004. The three nearly collocated pressure sensors provided for a consistency check between the instruments. Each pressure sensor was mounted on the bottom frame at a different height. The heights of the pressure sensors were measured from a flat surface in our laboratory and the distance from the lab floor to the pressure sensor was assumed the same when the bottom frame was deployed in Galveston Bay. The assumption of a solid bottom is, however, wrong since the bottom is actually made up of soft material the bottom pod legs penetrated. The pod was designed with cross-beams to provide greater surface area. The cross beams are assumed the limit of mud penetration (as noted by divers). The mean offset (applied in Fig. 3) for each instrument over the ten cruises was: ADV, 0.647m; ADCP 0.12m; Brancker CTD, 0.42m.

### *b. Meteorological Data*

Meteorological measurements were made on-site from a station mounted 3.4 m above the water surface on-board the small research vessel R/V Cavalla. Air-temperature and humidity (Campbell model CS500), water-surface temperature (ONSET Water Temp Pro - attached to a small surface float with the sensor tip at a depth of $\sim$0.1m), wind-speed (Campbell wind-anemometer model 03101-5) and direction (Campbell wind vane model

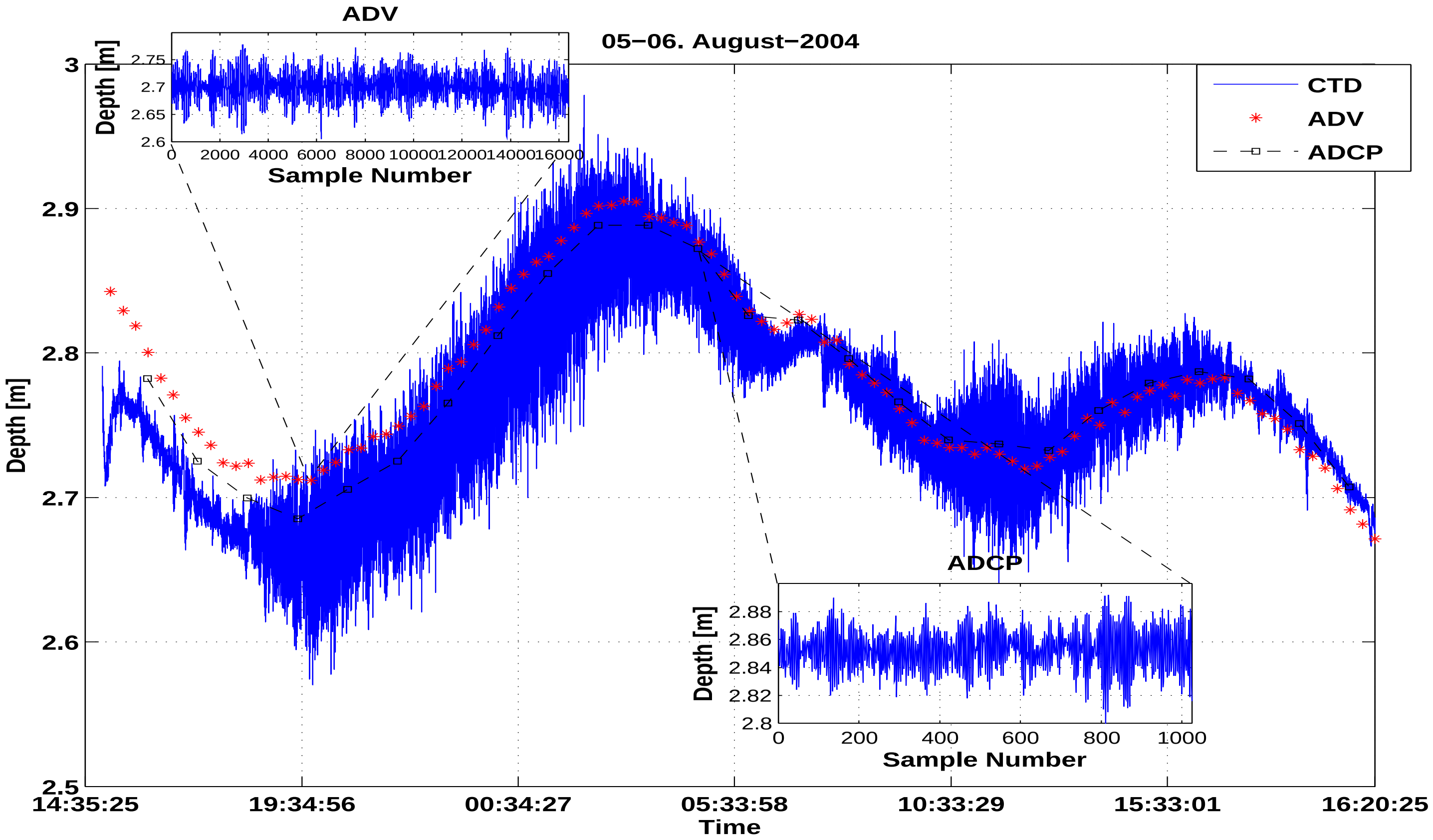

Fig. 3. Approximately 24–hours time-series of raw pressure signals from the ADV, ADCP and Brancker CTD. The ADV ($*$) pressure represents averages of 8.5 minute bursts sampled at 32Hz, taken every fifteen minutes. A sample burst is plotted in the upper left box with the dashed lines indicating when the burst was sampled. The ADCP pressure ($\diamond$) represent averages of 8.5 minutes bursts sampled at 2Hz every one hour (sample burst in lower right box), and the Brancker CTD (solid line) observed continuous pressure sampled at 1Hz. The variation of the CTD signal is due to changing wind speeds and changing surface variation.

03301-5), incoming solar radiation (Kipp & Zonen silicon pyranometer model SP Lite), incoming long wave solar radiation (Kipp & Zonen pyrgeometer model CG3), barometric pressure (Vaisala model PTA427), and rainfall rate (Texas Electronics tipping bucket rain gage model TE525) were measured. A Campbell Scientific data logger (model CR10) sampled each sensor every 5 seconds and data was stored as 10 minute averages throughout the period of each cruise.

The wind speed and direction are the most significant meteorological parameters for the local generation of wind-waves in Galveston Bay. To ensure accurate wind speed and direction measurements, the vessel was double anchored while pointing into the wind. Directions were also recorded manually with a handheld compass every half hour. In addition, winds were obtained from 3 surrounding coastal locations maintained by NOAA Physical Oceanographic Real Time System (PORTS). The PORTS near-real time measurements of meteorology, currents and water-levels are publicly accessible on the Houston/Galveston PORTS website from 1996 at 6-minute intervals (PORTS).

### *Wave Height and Period*

Wave heights and periods were estimated from dynamic pressure variance spectra converted to surface elevation variance spectra. The integrated surface elevation spectra (i.e. the zeroth-spectral moment, $m0$) is representative of the wave energy, and it is related to the significant wave height, $Hs$, by the relation $Hs = 4\sqrt{m0}$, where $Hs$ is the average of the highest one-third waves.

To compute the surface elevation spectra, each 8.5 minute burst of pressure time-series were sectioned into eight 50$\%$ overlapping segments, filtered with a Hamming window, and converted to the frequency domain using the Fast Fourier Transform (FFT). Spectral segments were then averaged together yielding variance spectra with 40 equivalent degrees of freedom (Emery and Thompson, 1997). Figure 4 (lower) shows an example of a pressure variance spectrum calculated using this procedure. Since pressure spectra are representative of the wave energy measured at the sensor depth, the bottom pressure spectra were converted to surface elevation spectra assuming first-order Stokes theory (i.e. linear theory). Derivation of this theory is described in many texts (e.g. Sorenson, 1978). The main result applied to the pressure spectra is presented here:

$$C_{\eta\eta p} = K_z \frac{C_{pp}}{\rho^2 g^2}, \tag{9}$$

where

$$K_z = \left[ \frac{\cosh kh}{\cosh(kz)}^2 \right]$$

is the linear theory conversion factor, $C_{pp}$ [m$^2$ s] is the measured pressure spectra, $z$ [m] is the height of the instrument above the seabed (positive upward) and $\rho$ is the water density. $k$ is the wavenumber obtained from the linear dispersion relation

$$\omega^2 = gk \tanh kh, \tag{10}$$

where $\omega = 2\pi f$ is the radian frequency.

The minor differences present in the pressure time-series (Figure 4 (upper)) are likely the result of the one meter horizontal separation between sensors, and the random undulating sea-surface. However, the calculated frequency spectra (Fig. 4 (lower)) show that both instruments measure the same energy up to the Nyquist sampling frequency limited by each instrument's sampling rate.

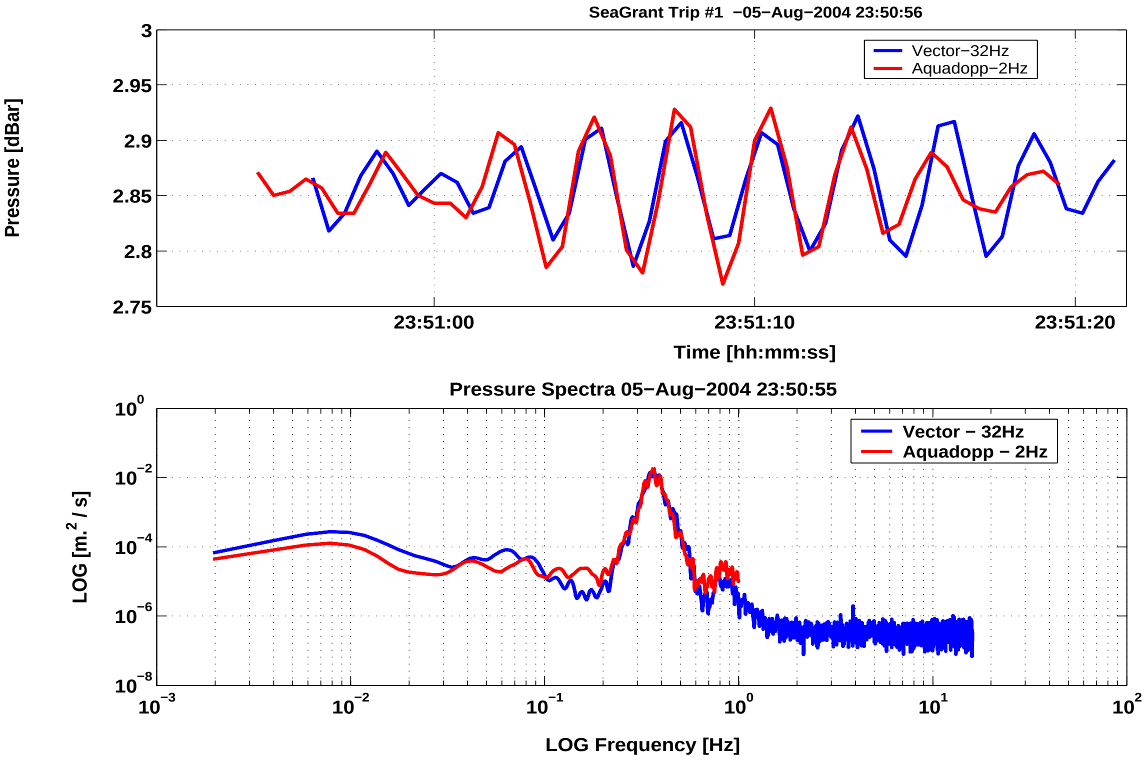

Fig. 4. a) Time series ( 30sec) of raw pressure from the ADCP and ADV, and b) their power spectra in the bottom panel. The peak frequency is the same for both instruments (bottom panel) and because they are nearly collocated they measure the same wave energy providing a consistency check.

### *Limitations*

Experimental results between bottom pressure sensor and surface elevation sensors (e.g. accelerometers) show wave height estimates from bottom pressure sensors and linear theory (9 are accurate to within $\pm 5\%$ (Bishop and Donelan, 1987; Smith, 2002). The limitations of estimating wave parameters from dynamic pressures include: 1) the instruments measuring capability (i.e.signal-to-noise ratio), 2) negligence of non-linear interactions and 3) wave-current interactions. The first two limitations are presented in this section along with the method applied to compare observed wave spectra with the empirical TMA spectra. The wave-current interactions and the limitations of measurement are presented in the next section (Wave Directions).

The ADV and ADCP pressure sensors, when positioned at 3m depth, are capable of resolving pressure changes equivalent to 1mm and 2.5mm undulations in surface elevation, respectively. However, according to Linear Theory, the pressure attenuation transfer function, $K_z$, increases with increasing wavenumbers (i.e. higher frequencies). $K_z$ is plotted vs. frequency in Figure 5 for depths ranging from 2.0 to 3.6 m. The conversion factor increases beyond $10^2$ at frequencies above 0.5 Hz for depths greater than 3m. Applying the conversion factor to the bottom pressure spectra yields discrepancies in the converted surface elevation spectra when the signal-to-noise ratio is low (Bishop and Donelan, 1987; Smith, 2002). Detection of this discrepency is noted by a sudden rise of spectral energy in the surface elevation spectra (Gordon and Lohrmann, 2001). An example of the phenomena is plotted from the GB ADV data in Figure 5. In such cases, it is common practice to employ a cut-off frequency and apply an empirical high-frequency tail (Bishop and Donelan, 1987; Gordon and Lorhman, 2001; Smith et al., 2001; Smith, 2002). In this experiment the sensors instrument noise was subtracted from the observed pressure spectra before apply-

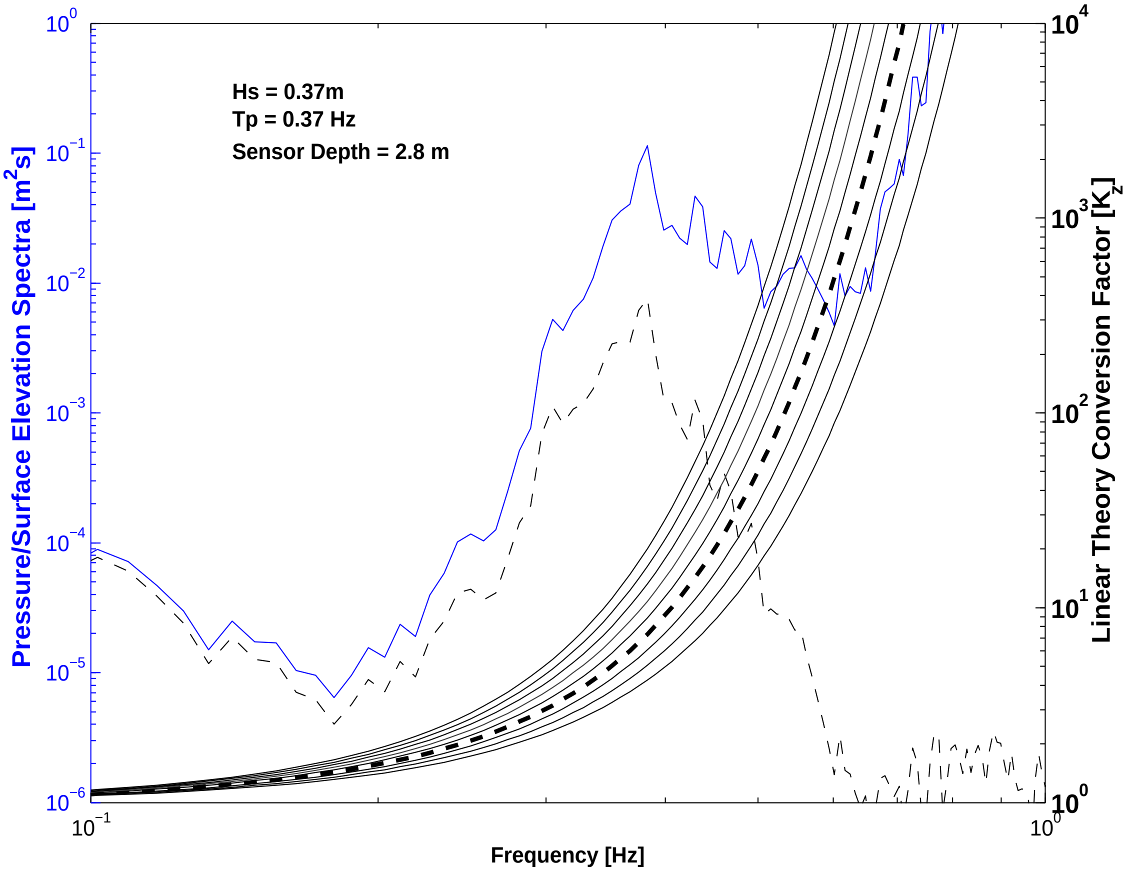

Fig. 5. Raw pressure spectra from the ADV at the instrument depth (dashed line) and the surface spectra (solid line) calculated from linear conversion factor in Eq. 9. The linear transfer function ($K_z$ in (9)) is also plotted (band of arching lines on the right vertical axes) vs. frequency for 2 – 3.6m depths. The transfer function is on the order of $10^2$ for a frequency of 0.6 Hz. Pressure noise (Fig.6b) is subtracted from the surface elevation spectra to reduce the low signal-to-noise ratio beyond 0.6 Hz and reduce the rise in spectral energy from the conversion factor.

ing the linear conversion factor (Bishop and Donelan, 1987). The data filtering techniques are described in the next paragraph.

Two methods were employed to ensure the quality of the data. The first method was a visual analysis of the individual wave spectra to determine whether a peak in the range of 0.1 - 1 Hz was clearly distinguishable from the assumed pressure sensor noise level. The “visual” filter excluded wave heights below 0.1m and correspond to wave spectra indistinguishable from the assumed instrument noise at 3m depth. The second quality control method was to find extremely calm conditions while the instruments were deployed, calculate the electronic “noise” level spectra and subtract this from the observed spectra before applying the linear theory. Calm conditions were described in our logbooks using the terms “calm winds” and “glassy seas.” Since two different ADCP’s were used over the ten cruises, noise levels were determined for both ADCPs. One noise level was determined for the ADV from the September 02–03 2004 cruise. The ADCP pressure noise levels from both instrument configurations during calm conditions (May 25–26 and September 02–03 for the 1 and 2 MHz ADCP’s, respectively) are plotted in Figure - 6(a), and the ADV noise level is plotted in Figure 6(b). The linear transfer function applied to each noise level yielded the equivalent-noise wave height. The ADCP with the 2MHz configuration yielded an equivalent-noise wave height of 0.08m. The ADCP with the 1MHz configuration yielded an equivalent-noise wave height of 0.16m, and the ADV’s equivalent noise wave height was 0.07m. Wave heights estimated below 0.1m were determined unreliable and subsequent wave frequency spectra were calculated, minus the instrument noise, and converted to surface elevation frequency spectra.

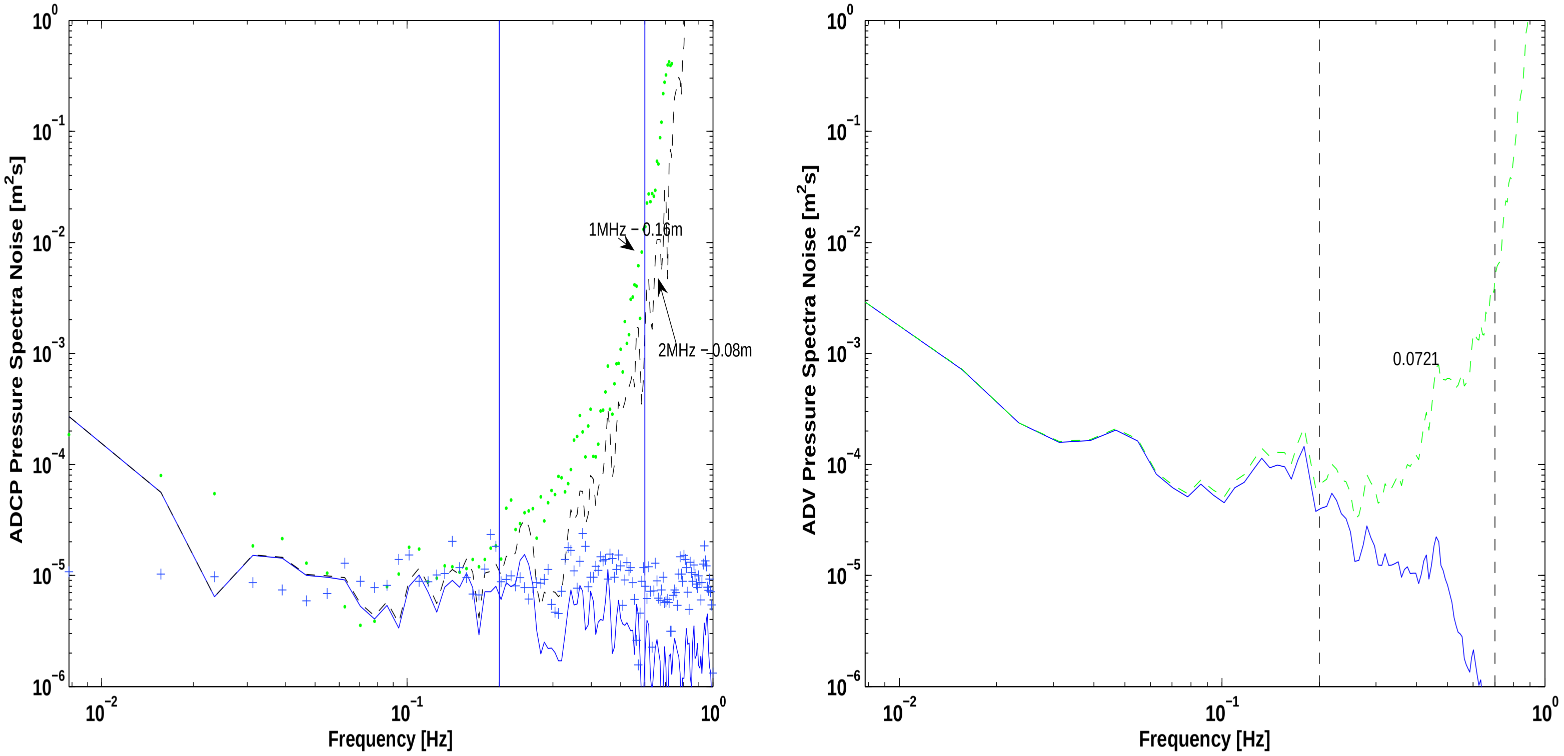

(a)

(b)

Fig. 6. a) Raw ADCP noise spectra with the converted surface elevation noise spectra. Two noise levels are plotted: one from the 1MHz ADCP configuration and the other for the 2MHz ADCP configuration. The equivalent-noise wave heights (written in figure) were estimated between the frequency range 0.2 – 0.7 Hz (vertical bars). The results are 0.16m and 0.08m for the 1 MHz and 2MHz configurations, respectively. b) The raw ADV noise with the converted surface elevation noise spectra. The equivalent-noise wave height was calculated between 0.2 - 0.7 Hz (vertical bars) and was determined to be 0.09m.

### *c. Spectral Tail*

The high-frequency spectral tail (beyond the spectral peak) was fit to the Phillips (1958) high-frequency form (3) using least squares algorithm. GB observations clearly do not follow Phillip's proposed form of a $f^{-5}$ tail. The Galveston Bay spectra follow a variable spectral form ranging from $f^{-2}$ to $f^{-10}$ according to a least squares analysis. $\alpha$ in (3) also varied over a large range.

Since the observed high-frequency tail does not follow the $f^{-5}$ form, the wave spectra were assumed to follow the variable, depth-dependant spectral tail proposed by Kitaigorodskii et al. (1975). This is a modification of the Phillip's theory. In addition to gravity influencing dissipation in the high-frequency tail, depth is assumed to influence whitecapping in shallow water (Kitaigorodskii, 1975). Subsequent analysis of the observed wave spectra are compared with the shallow water TMA spectra.

### *d. The TMA Fit*

GB surface elevation spectra were fitted and compared to the TMA shallow water spectra (7). Representative spectral shape parameters ($\alpha$, $\gamma$, $\sigma_a$, $\sigma_b$) fitted to wave spectra observed in depths ranging from 1.4 - 6m are listed in Table - 2. These parameters are based on the results of previous experiments in different shallow water bodies (e.g. Bouws et al., 1985; Liu, 1987; Young and Verhagen, 1996b) and were used to compare the fitted shape-parameters to GB observations.

The spectral fit was performed in the frequency range from 0 - 0.7 Hz using a non-linear least-squares fit of the TMA spectral equation written in terms of peak period and significant wave heights:

$$S(f) = \alpha H_s^2 T_p^{-4} f^{-5} \exp\left[-\frac{5}{4}\left(T_p f\right)^{-4}\right] \gamma^{\exp\frac{-(T_p f-1)^2}{2\sigma^2}} \tag{11}$$

$H_s$ and peak period, $T_p$ were determined from the observed spectra (see Wave Height and Period section). $95\%$ confidence intervals were calculated using the Bootstrap method for the entire data set, each cruise and during steady wind directions.

Examples of individual observed surface spectra from consecutive 15 minute intervals measured from the ADV pressure (from August 12, 2004 cruise) are plotted in Figure - 7. The $Hs$ and $Tp$ estimated from the spectra are written in each subplot. The TMA spectra are overplotted on each sub-graph and the corresponding shape parameters resulting from the least-squares fit are written in each subplot.

Table 2. A list of previously fit TMA spectral shape parameters in depths ranging from 1.4 - 6m, and the Galveston Bay spectral shape parameters.

| Date/Author(s) | Hs [m] | Depth [m] | $\alpha$ | $\gamma$ | $\sigma_a$ | $\sigma_b$ |
|---|---|---|---|---|---|---|
| Bouws et al.,1985 | 2.7 | 6 | 0.0135 | 2.12 | 0.127 | 0.058 |
| | 3 | 6 | 0.0133 | 2.68 | 0.101 | 0.101 |
| Liu,1987 | 0.99 | 1.4 | 0.051 | 2.23 | 0.2 | 0.2 |
| | 0.96 | 2.3 | 0.018 | 3.41 | 0.167 | 0.333 |
| | 0.62 | 2.8 | 0.009 | 3.64 | 0.286 | 0.286 |
| | 1.38 | 3.8 | 0.033 | 2.25 | 0.143 | 0.286 |
| Young and Verhagen, 1996b | 2 | 1.8 | 0.01 | 2.5 | 0.1 | 0.1 |

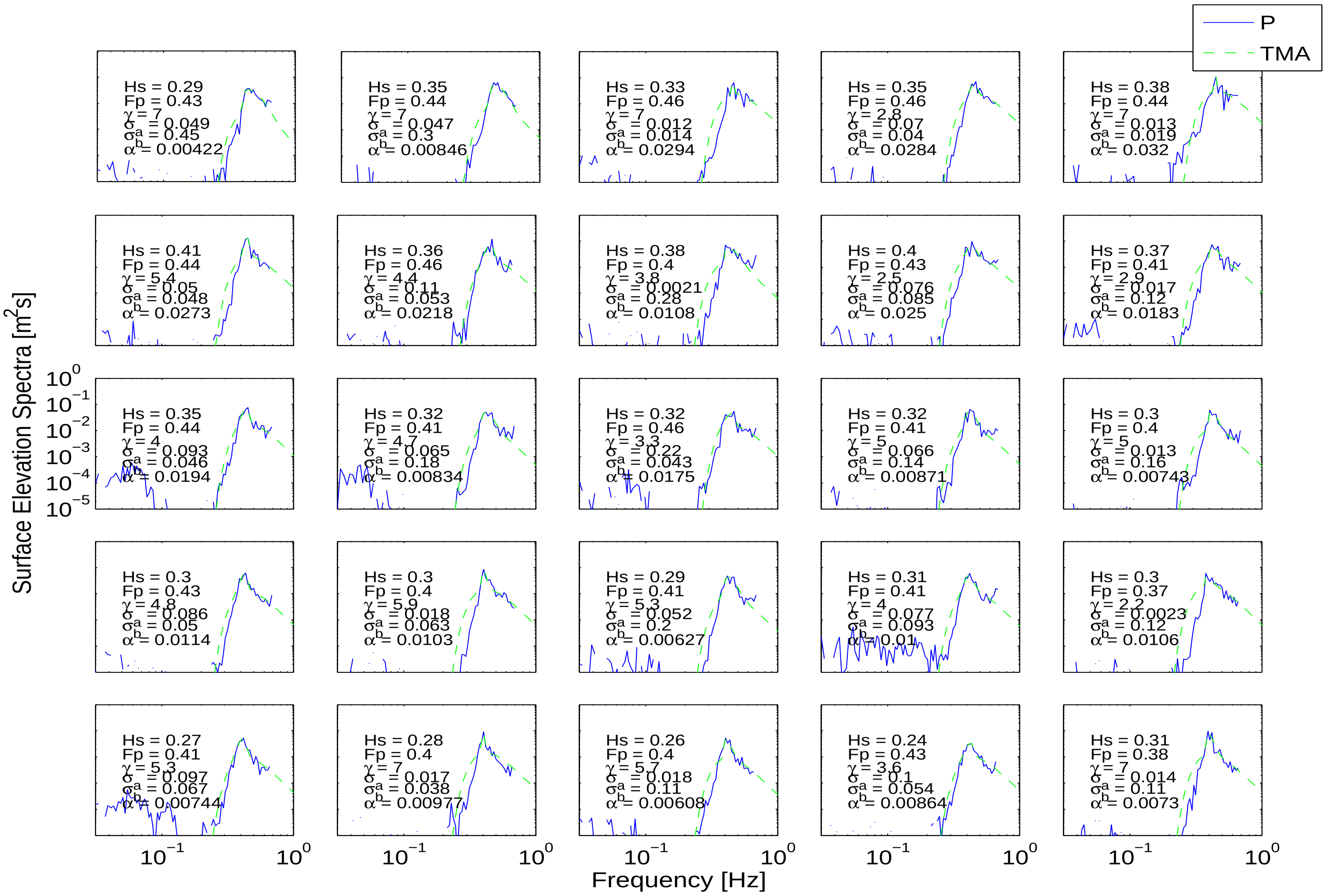

Fig. 7. Twenty five surface elevation spectra calculated from the ADV. The significant wave heights estimated from each spectra are indicated on the respective subplot using the zeroth spectral moment and the equation: $Hs = 4 * sqrt(m0)$. Using the $Hs$, peak period and the fitted spectral parameters listed in 2, the TMA empirical spectra were estimated and overplotted (green solid line).

### *Wave Direction*

Waves produce subsurface orbital velocities. The magnitude of the velocities are strongly attenuated with depth. The ADCP and ADV measure the orbital velocities which can be used to estimate wave direction. Figure 8(a) shows a time-series of pressure, and the $U$ and $V$ velocity components. Assuming the orbital velocities are in the same direction as the wave, the differences in horizontal velocity components (here a larger $V$-component) indicate a wave propogating in a NNE direction. Following the $PUV$ method (Gordon and Lohrmann,2001) direction, $D$, was calculated from the cross-spectra between the pressure and the $U$ and $V$ orbital velocity components:

$$D = atan2(C_{pu}, C_{pv}) \tag{12}$$

where $C_{pu}$ and $C_{pv}$ are the cross-spectra between $P$ and $U, V$ and $atan2$ is the four-quadrant arc-tangent. Figure 8(b) is an example of directional wave spectra and shows that most of the wave energy propagates toward the NNE with a period in the range of 2.5-3.5 seconds. The wave directions are in good agreement with the wind direction measured and from both current meters which measure currents differently.

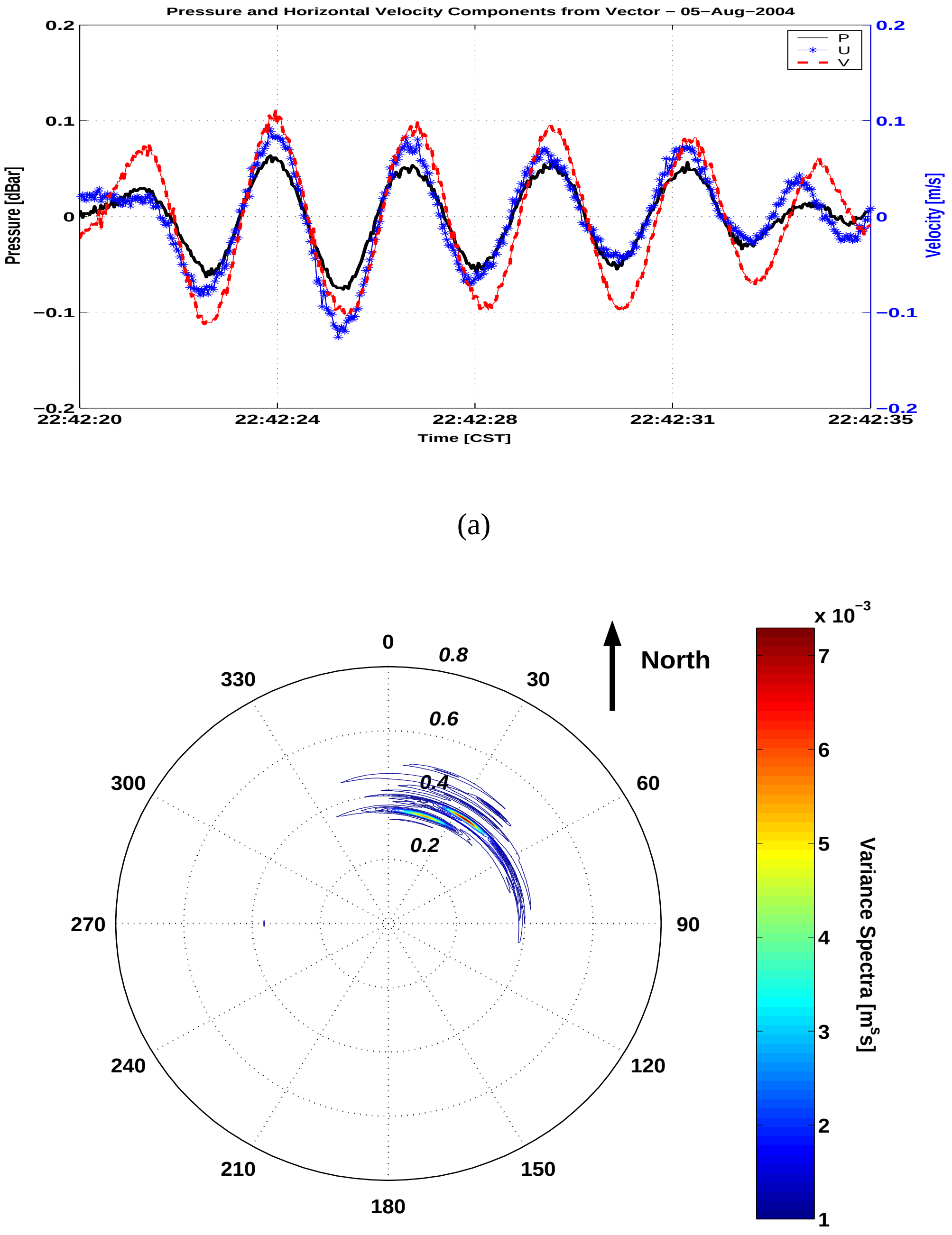

(a)

(b)

Fig. 8. a) 30 second time series of pressure and horizontal U,V current components. b) Directional wave spectra showing spectral energy, wave direction and the frequency [Hz] (inner radii) The units of the spectral energy (colorbar on right-hand side are [$m^2$s].)

# 3. RESULTS

The wave observations are presented in this section. A brief summary of the wind speed, wind directions, water levels and currents are presented first followed by comparison of the observed wave spectra to the empirical TMA spectra. The wave statistics (Hs, Tp and Direction) estimated from the wave spectra are then summarized. Finally, the data are compared to empirical growth relations proposed for fetch-limited finite-depth bodies of water. The GB data are combined with previous observations in a shallow lake to extend the currently proposed asymptotic limit of non-dimensional energy growth in shallow water. Sample results are presented as hindcasts to the observed wave heights using the proposed extension to the asymptotic growth limit.

## *a. Winds, Water Levels and Currents*

Summary histograms of the $U$,$V$ current velocity components are plotted in Fig. 9-a & b, respectively. The mean current magnitude observed over all cruises was $0.057$ m/s with a range from $0$ to $0.16$ m/s. Histograms of wind speeds ($U_{10}$) and directions are plotted in Figure 9-c & d, respectively. The wind speeds ranged from 0 - 11 m/s (Fig. 9-c) and a wide range of wind directions were observed (Fig. 9-d).

A time-series of wind speed vectors, current vectors and water levels are plotted in Figure 10 for the 02-03, April 2005 cruise (data from all cruises are plotted in the same format in Appendix B). The top panel shows wind vectors representing 10 minute averages. The second panel from the top shows the ADCP burst-averaged current vectors at 60 minute intervals. The third panel down shows the ADV current vectors, burst-averaged, at 15 minute intervals, and the bottom panel shows the burst-averaged water level measured from the ADV. At the start of the 02-03, April 2005 cruise, the wind was light and variable

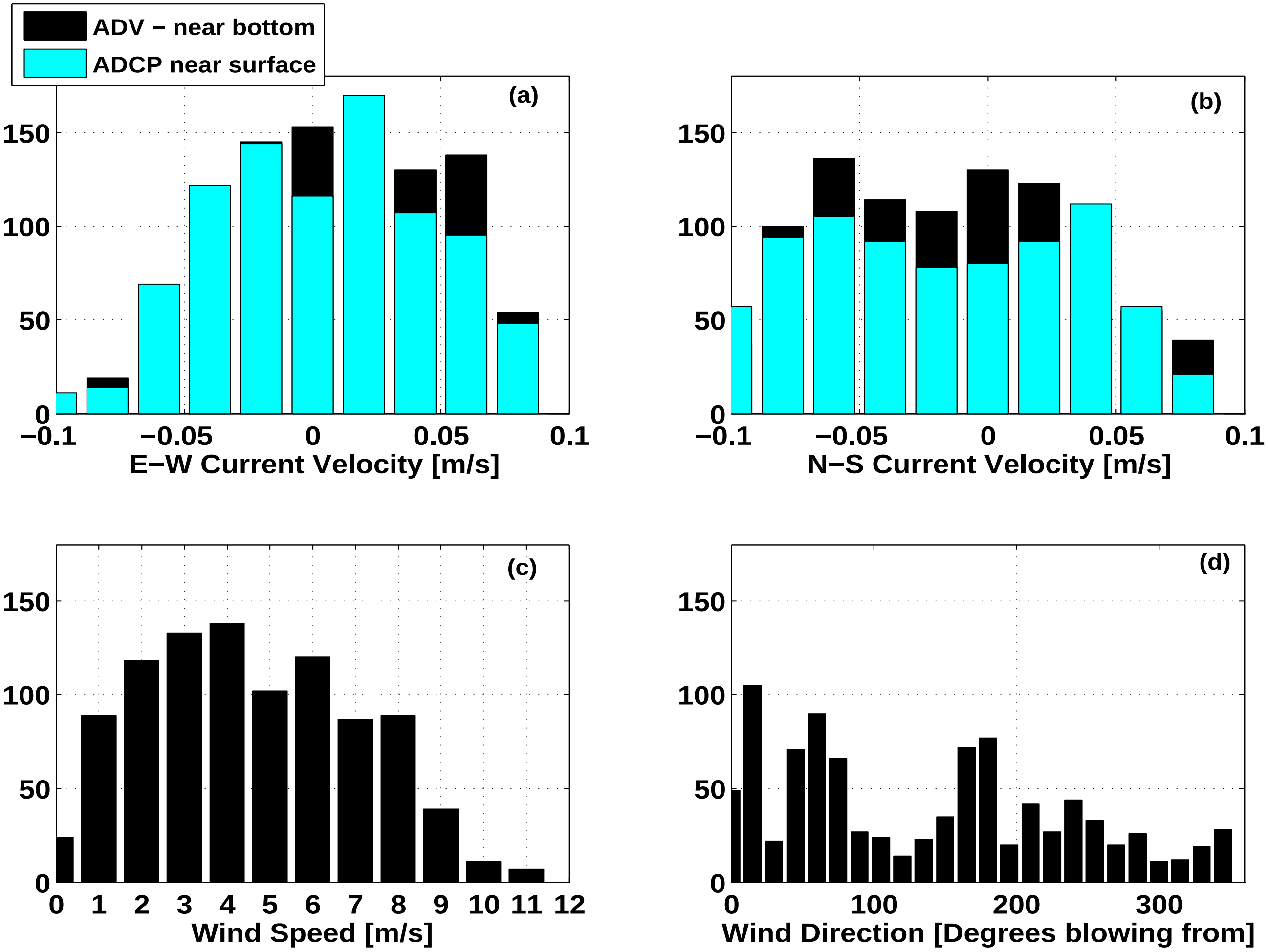

Fig. 9. a) Histogram of the E-W current velocity component measured from the ADCP (Dark) and ADV (Light). b) Histogram of the N-S current velocity component from the ADCP and ADV. c) Wind speeds [m/s] and d) wind directions [degrees from true North). The data are taken from all cruises.

shifting from north to southwest winds. After 1800 (Central Standard Time; CST) the wind speeds increased to about 6 m/s from the southwest, gradually decreased in magnitude and were light and variable by the end of the cruise. At 1200 [CST] till about 19:12, the surface and bottom currents directions were northerly and then became southerly (opposite to the wind). This change coincides with the maximum observed water level (tidal change). In general, the currents coincide with the water level changes for all cruises except cruise 5 (13-14, November 2004 - Fig. 29) when the wind blew from the same direction for the entire sampling period and gradually increased in magnitude from 6 to 11 m/s. In this case, the currents did not change directions with tidal changes, and the current direction was the same as the wind direction for the entire cruise period.

### *b. Wave Characteristics*

The observations of wave height, periods, and directions are summarized in this section. Figure 13 shows histograms of wave heights, peak frequencies and wave directions. The range of wave heights observed during ten cruises were calm to 0.64m, and the average peak frequency was 0.4 Hz with a range of 0.31 to 0.53 Hz for both the ADCP and ADV data sets. The mean, standard deviation and range of wave heights for each cruise and for all of the cruises combined are listed in Table 3. Time-series of wave estimates from the 15-16, January 2005 cruise are plotted in Fig. 12 and show the high correlation between the winds and waves. The upper panel shows Hs and $U_{10}$, the middle panel shows $T_p$, and the bottom panel shows wind and wave directions. The wind and wave time-series for all cruises are presented in Appendix C.

The Galveston Bay wave spectra are described by the empirical TMA wave spectra for $Hs = 0.1 - 0.64$m with the following mean spectral shape parameters : $\alpha = 0.016$,

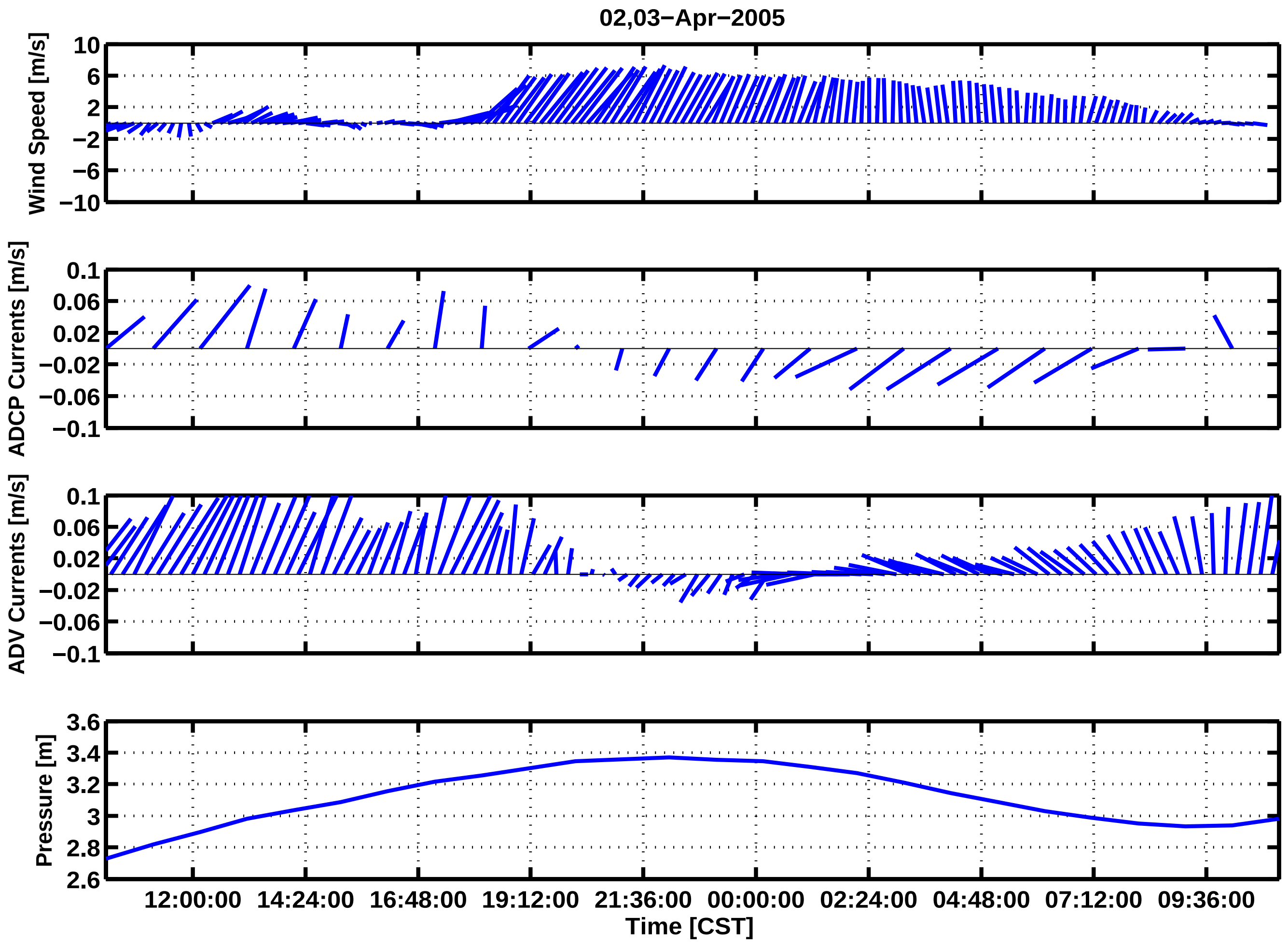

Fig. 10. Approximately 24-hour time-series of: (Upper panel) Wind vectors [m/s]; Middle panels are the current vectors from the ADCP (upper) and ADV (lower) and the bottom panel is the burst-averaged pressure from the ADV.

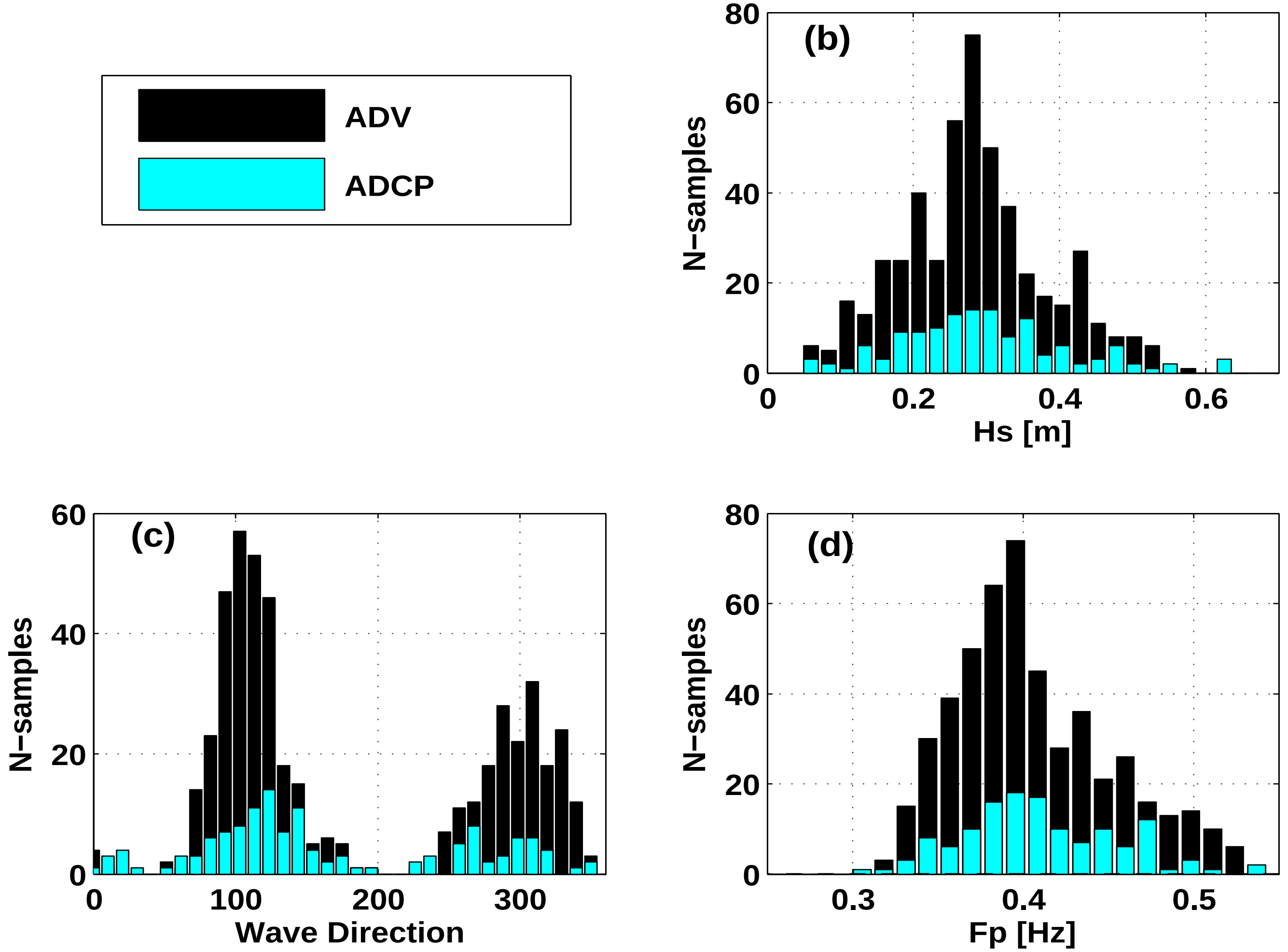

Fig. 11. b) Histogram of $Hs$, c) Histogram of wave directions and d) histogram of peak frequency. The histogram data are plotted from all cruises. The black bars represent ADV data, and the light shaded bars represent ADCP data.

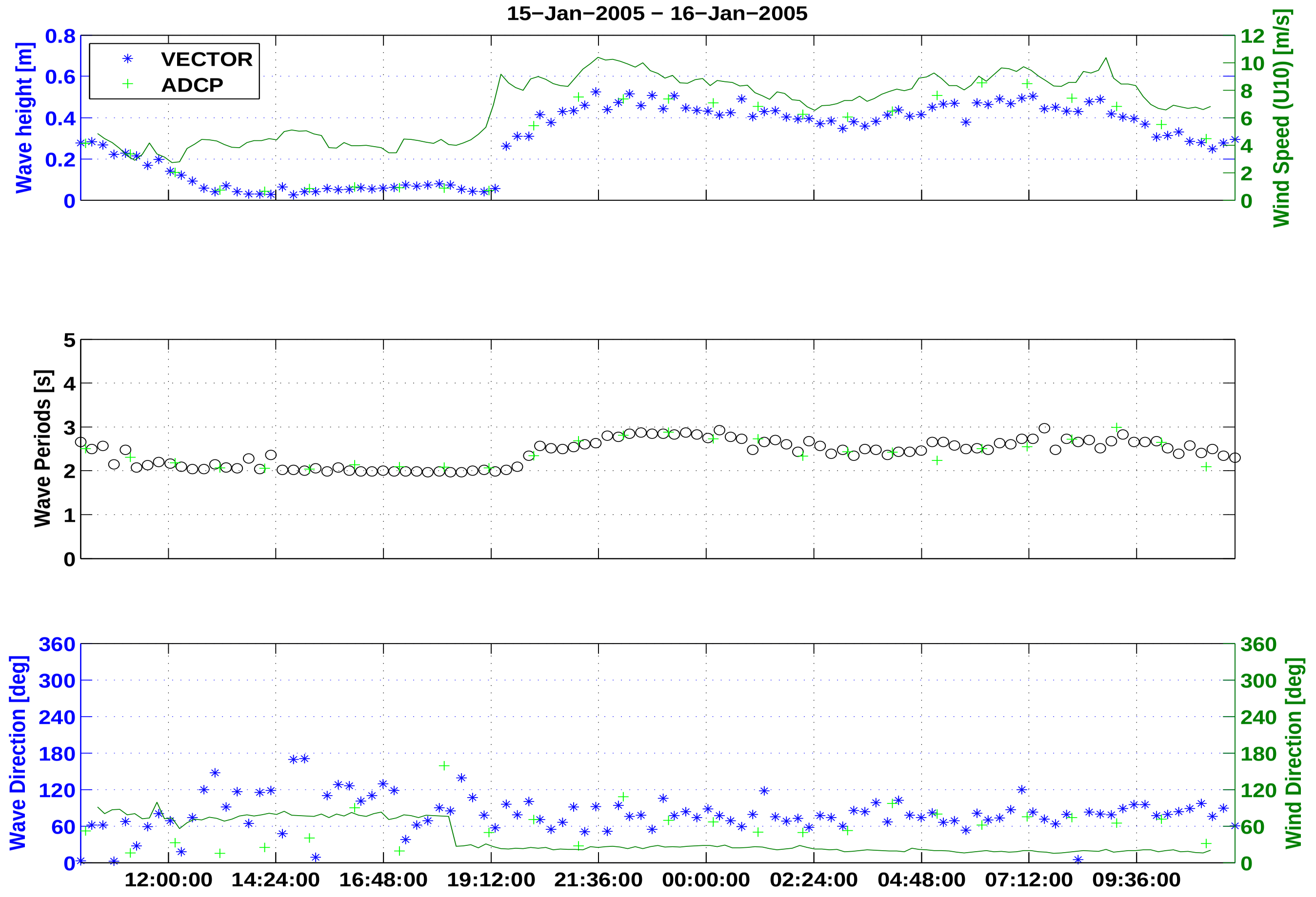

Fig. 12. Time series of wind speeds (solid line-right-hand axis) and $H_s$ (ADV,○;ADCP,+; Upper), peak period [s](middle), and wind (line) and wave directions (lower). The ADV and ADCP markers are the same for the direction subplot.

Table 3. Summary of significant wave heights for ten twenty-four hour cruises.

| | ADCP | | | ADV | | |
|---|---|---|---|---|---|---|
| Cruise Date | Mean. | Range | SD | Mean . | Range | SD |
| 05-06, August 2004 | 0.28 | 0.14-0.42 | 0.08 | 0.26 | 0.1 - 0.4 | 0.07 |
| 12-13, August 2004 | 0.3 | 0.21-0.37 | 0.04 | 0.3 | 0.24-0.37 | 0.03 |
| 02-03, September 2004 | 0.15 | 0.13-0.17 | 0.01 | 0.15 | 0.07-0.2 | 0.03 |
| 06-07, November 2004 | 0.21 | 0.1-0.3 | 0.06 | 0.24 | 0.18-0.29 | 0.03 |
| 13-14, November 2004 | 0.41 | 0.26-0.64 | 0.12 | 0.36 | 0.22-0.63 | 0.1 |
| 15-16, January 2005 | 0.43 | 0.22-0.57 | 0.1 | 0.4 | 0.14-0.52 | 0.09 |
| 04-05, February 2005 | 0.18 | 0.06-0.27 | 0.1 | 0.2 | 0.18-0.22 | 0.02 |
| 25-26, March 2005 | 0.18 | 0.07-0.27 | 0.08 | 0.21 | 0.07-0.34 | 0.08 |
| 02-03, April 2005 | 0.33 | 0.15-0.5 | 0.1 | 0.3 | 0.11-0.52 | 0.11 |
| 25-26, May 2005 | 0.28 | 0.18-0.36 | 0.06 | 0.25 | 0.1-0.36 | 0.08 |
| All Cruises | 0.3 | 0.06 - 0.64 | 0.12 | 0.31 | 0.07-0.63 | 0.1 |

$\gamma = 4.26$, $\sigma_a = 0.063$, $\sigma_b = 0.089$. The means and $95\%$ confidence intervals of the spectral shape parameters were calculated from a bootstrap analysis. An example of the mean observed wave spectra from November 13-14, 2005 is plotted with the TMA spectrum calculated with the mean significan wave height, period and fitted shape parameters specific to this cruise. The $95$% confidence intervals obtained from the bootstrap fit are overplotted. The mean fits from each individual cruise are listed in Table 4.

Spectral shape parameters from two quasi-steady physical settings are presented with the model empirical TMA spectra. The two physical scenarios are: 1) wave generation from increasing wind speed and constant direction and 2) wave dissipation during constant wind direction and decreasing wind speeds. In both cases, the variation of wind direction was $\pm 15^o$, and this was considered quasi-steady. The purpose of comparing these scenarios was to understand the limits of the mean shape parameters during changing wave energy without significant directional changes.

Figure 14 shows three subplots of spectra from the wave generation scenario. The left panel shows all of the filtered wave spectra observed from the 13-14, November 2004 (sg05) cruise. The wind was blowing from the same direction ($\pm 15^o$) for the entire cruise and gradually increased in wind speed. As the wind speed increased, wave height increased and peak frequency decreased. The middle panel has three spectra plotted at random to clearly see the "evolution" of the spectra with increasing wind speed. The TMA spectra were calculated from $H_s$, $T_p$ and the mean shape parameters listed for sg05 in Table 4 and are overplotted in the middle panel. The third panel shows the mean wave spectrum and the fitted TMA spectra with $95\%$ confidence intervals overplotted.

The decaying wind speed scenario was observed during 02-03, April 2005 (sg09) from about midnite till 0300. Figure 15 shows three subplots of the wave spectra taken from

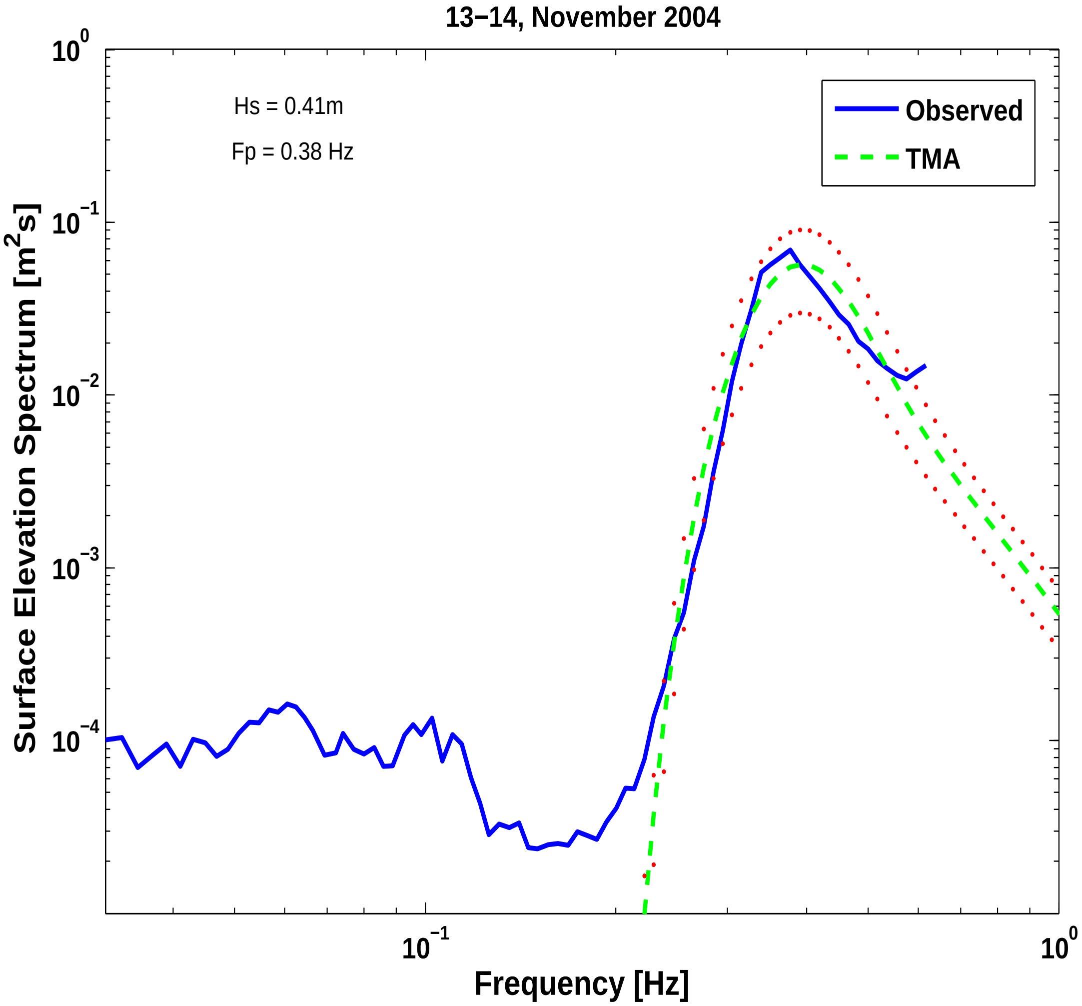

Fig. 13. The mean observed surface elevation spectra during constant wind direction from the 13-14, November 2004 cruise (solid line). The fitted TMA spectrum is overplotted (dashed line) with the mean significant wave height and peak frequency written to the side.

Table 4. A list of fitted TMA spectral shape parameters for each GB cruise.

| Date/Author(s) | $\alpha$ | $\gamma$ | $\sigma_a$ | $\sigma_b$ |
|---|---|---|---|---|
| 05-06, August 2004 | 0.0160 ± 0.0021 | 4.26 ± 0.28 | 0.0635 ± 0.0139 | 0.0891 ± 0.0166 |
| 12-13, August 2004 | 0.0137 ± 0.0023 | 4.72 ± 0.69 | 0.0669 ± 0.037 | 0.0669 ± 0.0237 |
| 02-03, September 2004 | 0.0141 ± 0.0051 | 3.57 ± 1.2 | 0.0914 ± 0.0704 | 0.0886 ± 0.0786 |
| 06-07, November 2004 | 0.0351 ± 0.0174 | 2.70 ± 1.08 | 0.0393 ± 0.0231 | 0.0783 ± 0.0858 |
| 13-14, November 2004 | 0.015 ± 0.0034 | 4.74 ± 0.56 | 0.0721 ± 0.0428 | 0.0898 ± 0.0320 |
| 15-16, January 2005 | 0.0248 ± 0.0062 | 4.20 ± 0.84 | 0.049 ± 0.0231 | 0.0752 ± 0.068 |
| 04-05, February 2005 | 0.0099 ± 0.0021 | 4.87 ± 0.63 | 0.0781 ± 0.0473 | 0.0867 ± 0.0378 |
| 25-26, March 2005 | 0.0195 ± 0.0151 | 3.75 ± 1.41 | 0.0365 ± 0.0321 | 0.295 ± 0.4215 |
| 02-03, April 2005 | 0.0099 ± 0.0021 | 4.87 ± 0.67 | 0.0785 ± 0.0496 | 0.0865 ± 0.0397 |
| 25-26, May 2005 | 0.0159 ± 0.0073 | 3.41 ± 0.921 | 0.0609 ± 0.0446 | 0.1017 ± 0.0751 |

the decaying period. The subplots follow the same format as Figure 14, and the observed spectral evolution (with time) is opposite to the spectral evolution during the wave growth scenario. The wave height decreases (i.e. spectral energy decreases) and peak period increases.

### c. *Empirical Wave Prediction Models*

Sverdrup and Munk proposed deep water wave-forecasting relations in the 1940's from nomographs of wave data converted to non-dimensional parameters: $H' = \frac{gHs}{U^2}$ vs. $F' = F\frac{g}{U^2}$ and $T' = \frac{gT}{U}$ vs. $F' = F\frac{g}{U^2}$ where $H'$ is non-dimensional significant wave height, $T'$, non-dimensional peak period and $F'$, non-dimensional fetch (Sverdrup and Munk, 1947). These "graphical" techniques were employed by Bretschneider (1958) who found asymptotic limits to wave growth with depth (i.e. $\epsilon$ vs. $\delta$ defined in the Introduction):

$$\epsilon = 1.4 \times 10^{-3}\delta^{1.5} \tag{13}$$

and

$$\nu = 0.16\delta^{-0.375} \tag{14}$$

Ijima and Tang (1966) proposed fetch limited finite depth growth curves based on the asymptotic growth limits of Bretschneider (1958) and accounted for bottom friction and percolation using the results of Bretschneider and Reid (1953). Their work was modified further in CERC (Coastal Engineering Research Center, 1984) to conform to the JONSWAP deep water observations. The result of this work is an empirical forecasting technique suitable for predicting and hindcasting wind-waves in shallow bodies of water when fetch lengths, wind speeds and depths are known. The non-dimensional forecasting equa-

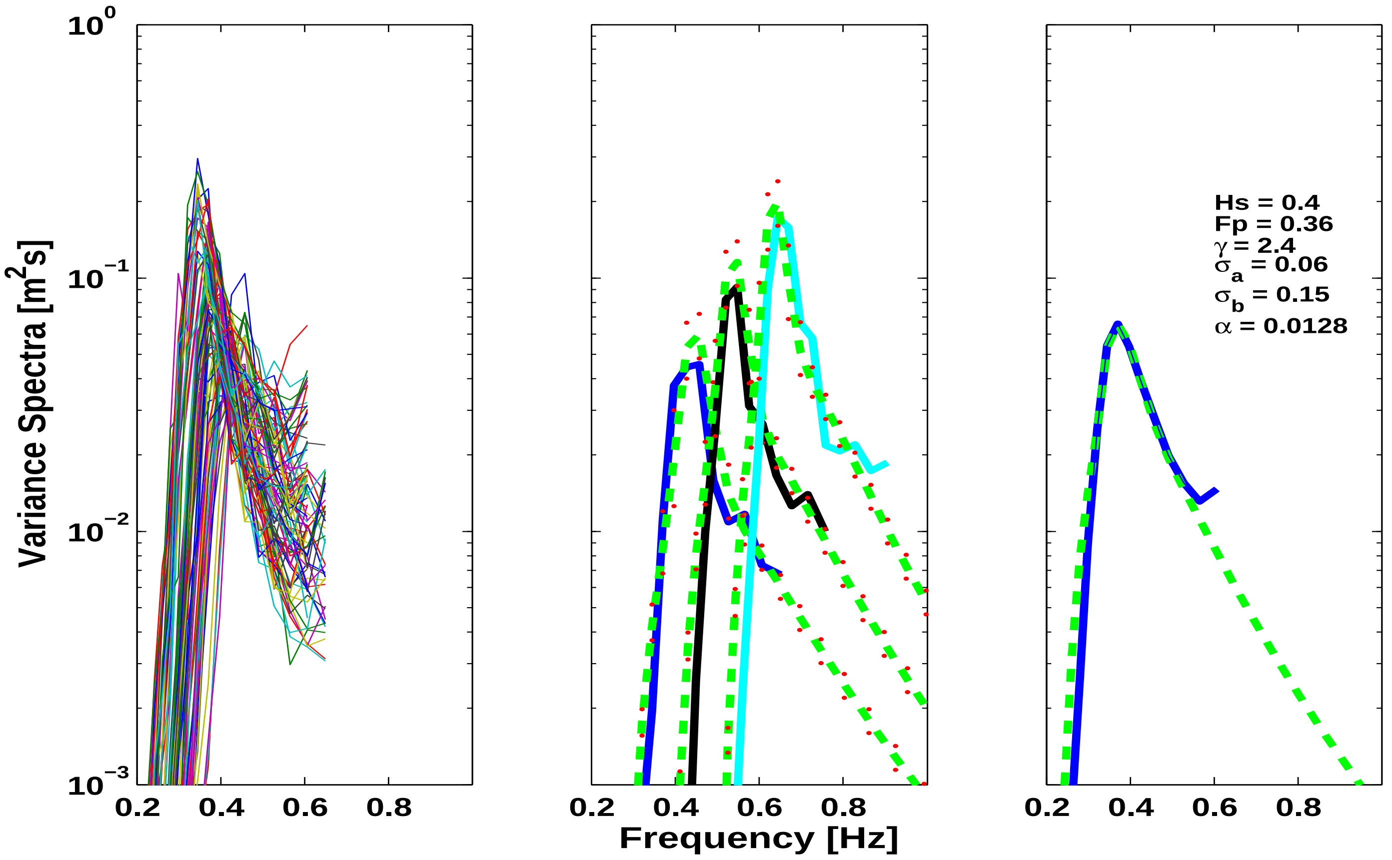

Fig. 14. All observed spectra from the 13-14, November 2004 cruise (sg05; left).Three characteristic spectra evolving during increasing wind (middle). The spectrum farthest right is offset by 0.3 Hz and the middle spectrum offset by 0.15 Hz. The TMA spectra are also plotted (dashed line) with $95\%$ confidence intervals overplotted (.) The mean observed spectra during constant wind direction from the 13-14, November 2004 cruise (solid line;left). The fitted TMA spectrum is overplotted (dashed line) with the mean significant wave height, peak frequency and shape parameters written to the side.

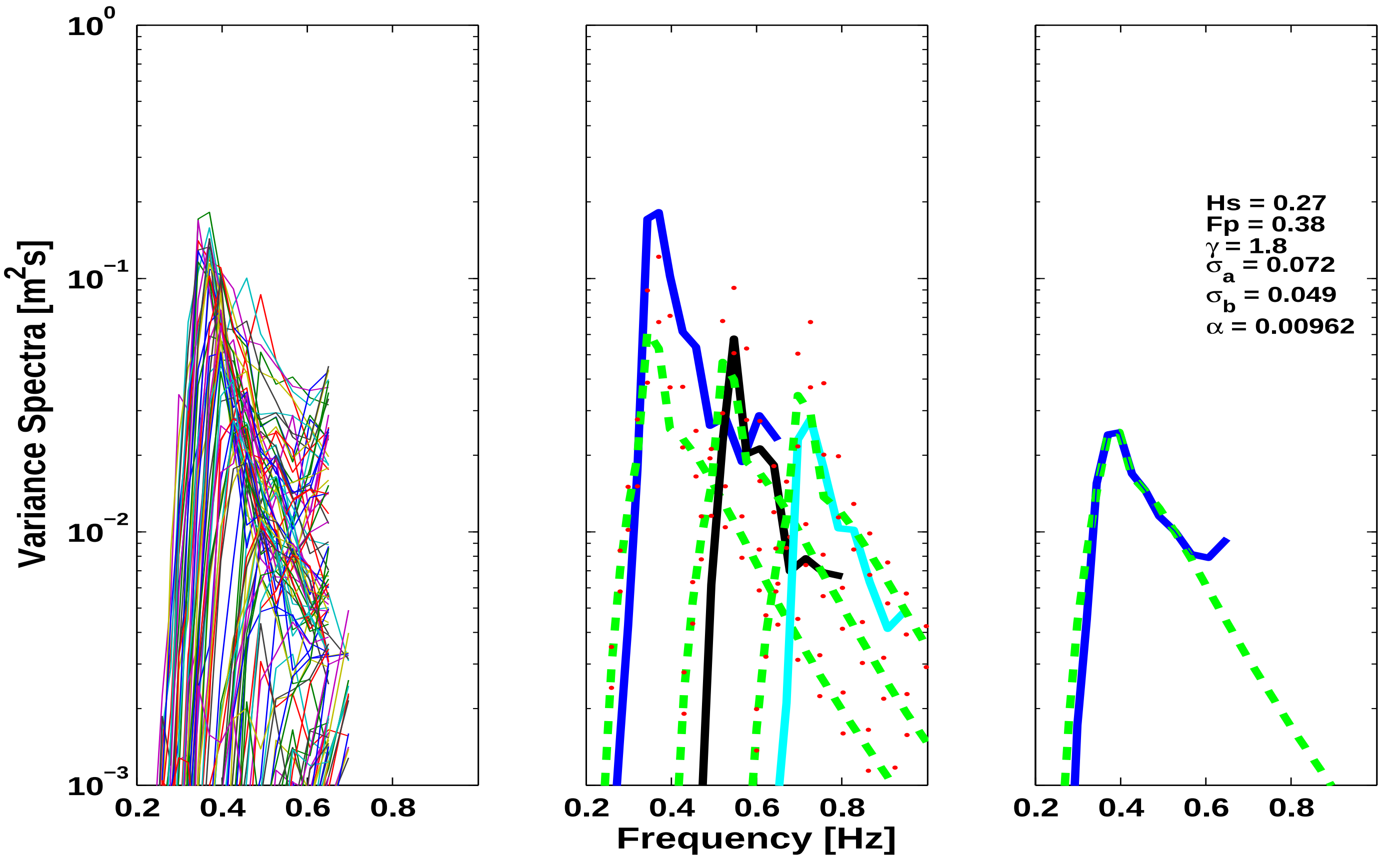

Fig. 15. Similar to Fig. 15. except for the 02-03, April 2005 cruise (sg09)

tions are:

$$\epsilon = 5 \times 10^{-3} \left[\tanh A_1 \tanh[\frac{B_1}{\tanh A_1}]\right]^2 \tag{15}$$

where

$$A_1 = 0.53\delta^{0.75}$$

and

$$B_1 = (5.65 \times 10^{-3})\chi^{0.5}$$

$$\nu = 0.133 \times 10^{-3} \left[\tanh A_2 \tanh[\frac{B_2}{\tanh A_2}]\right]^{-1} \tag{16}$$

where

$$A_2 = 0.833\delta^{0.375}$$

and

$$B_2 = (3.79 \times 10^{-2})\chi^{0.33}$$

Based on observations in shallow (2m depth) Lake George, Australia, Young and Verhagen (YVa; 1996a) proposed two asymptotic power law relations for $\epsilon$ versus $\delta$ and $\nu$ versus $\delta$:

$$\epsilon = 1.06 \times 10^{-3}\delta^{1.3} \tag{17}$$

and

$$\nu = .20\delta^{-0.375} \tag{18}$$

The YVa data set comprise wind and wave data from multiple stations at different fetch lengths and nearly constant depth (2m). The asymptotic limits proposed are based on their full data set. However, the variation in growth with fetch (range: 1-16km) was observed for wind speeds and directions not varying more than $10\%$ within 30 minutes, and YVa used graphical techniques to redefine the relations in (15) & (16) based on their observations.

Their proposed refinements to (15) and (16) are:

$$\epsilon = 3.64 \times 10^{-3} \left[ tanh A_1 tanh[\frac{B_1}{tanh A_1}] \right]^{1.74} \tag{19}$$

where

$$A_1 = 0.493\delta^{0.75}$$

and

$$B_1 = (3.13 \times 10^{-3})\chi^{0.57}$$

$$\nu = 0.133 \left[ tanh A_2 tanh[\frac{B_2}{tanh A_2}] \right]^{-0.37} \tag{20}$$

where

$$A_2 = 0.331\delta^{0.75}$$

and

$$B_2 = (5.215 \times 10^{-4})\chi^{0.73}$$

Young and Babanin (YB; 2005) have further modifed the non-dimensional depth exponent ($\delta^n$) in equation (17) from 1.3 to 1.2 based on the extension of observations to shallower depths ($0.6 < d < 1.15$) than YVa.

The depth and fetch ranges of Lake George (0.5 - 2m depth, fetch: 1-16km) are similar to Galveston Bay (2.5 - 3.5m depth; fetch 3-25 km). The GB data were compared to the asymptotic limits proposed by YV(a) (Eqns. 17-18) and Bretschneider (1958) in Figure c), respectively. The asterisks ($*$) represent GB data, the solid line is the YB limit and the dashed line is the work of Bretschneider. The Galveston Bay observations follow the asymptotic limit of YB in the Lake George depth range, and extend their range out to 3.5m depth. A least sqaures analysis of the GB and YB data yield a new asymptotic limit of $\epsilon$ vs. $\delta$ based on the extension of observations in larger $\delta$. Note, the GB data set was collected in a different environment with completely different wave measurement techniques. The instruments used to measure waves in YVa and YB were surface piercing wave staffs. This is also an indirect confirmation of data between two completely different experiments. The YB and Bretschneider asymptotic limits are plotted with the Galveston Bay observations in Fig. 16.

Figures 17 - 18 show comparisons of empirically modelled and observed wave heights calculated from Equation 19 for two different twenty-four hour cruises using n = 1.74. The empirically modeled relations follow the trend of the observations for periods of steady wind directions (e.g. fetch length) and moderate wind speeds. The relations do not work for periods of rapidly changing wind direction and wind speeds less than 1 m/s. Wind speeds less than 1 m/s cause extremely high values of non-dimensional wave parameters. This is due to the second and fourth inverse powers of the wind speed in the definitions of $\chi$, $\delta$ and $\epsilon$, respectively. Rapid changes in wind directions do not work because $\chi$ is defined using a fetch length set for every $15^o$ interval around the compass. This acts as an "instantaneous" change in fetch length when, for example, the wind direction changes from N to E. Also, the proposed forms from YVa are based on data collected in wind speeds not changing more than $10\%$ over 30 minutes and wind directions $\pm 20\%$ of their instrument array. It is striking that the GB data follow the asymptotic limits proposed in a shallow lake with data collected using completely different measurement techniques since the YVa and YB data were collected with wave staffs. This is not a new finding since Smith, et al. (2001) also show their data to follow the YVa limits from PUV data.

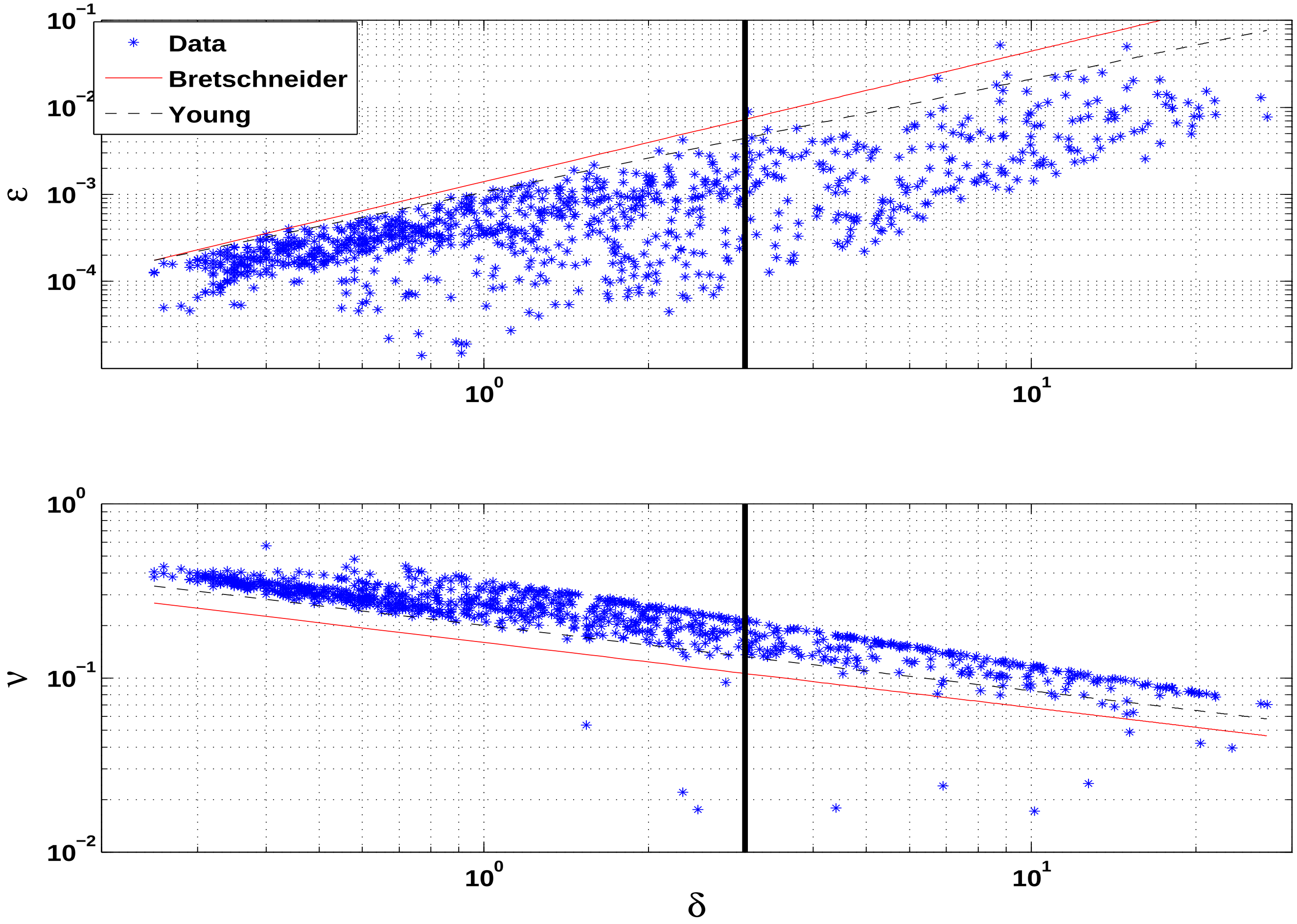

Fig. 16. (Upper) Non-dimensional energy ($\epsilon$) vs. non-dimensional depth ($\delta$). (Lower) Non-dimensional frequency ($\nu$) vs. $\delta$. In both plots the ADV ($*$), ADCP ($\diamond$) are plotted against the proposed asymptotic limits of Young and Verhagen (1996a) (dashed line)) and Bretschneider (solid line).The GB data follow the proposed asymptotic limits of YB and extend their range of observations.

# 4. NUMERICAL MODELING

The physics governing the generation, propogation and dissipation of waves are implemented in third-generation numerical wave models such as WAM and WAVEWATCH (Booij, et al.,1999). These models predict and hindcast waves in time and space, and they are designed for global scales based on explicit numerical schemes. Numerical stability (CFL-condition) limits the time and spatial ranges of the computational domain such that depths less than 20m and horizontal scales of 20-30km are computationally inefficient (Booij, et al.,1999). The third-generation Shallow WAves in the Nearshore model (SWAN) is based on implicit numerical schemes and is not constrained by stability conditions. It is suitable for small-scale shallow regions with time-steps larger than 10 sec on desktop computer. SWAN (version 40.41AB) was implemented in a Galveston Bay computation domain to hindcast the wave field from observed wind data, bathymetry and currents. The model output is compared to the Galveston Bay observations.

## *a. Simulating Waves Nearshore (SWAN) Model*

SWAN is a spectral model. The physics implemented in the numerical code represent the wave spectra calculated from explicit physical processes (source/dissipation terms) governing wave generation and dissipation. It does not require prior knowledge of the wave spectra, and the source/dissipation terms included in the model are: wind-generation, triad and quadruplet wave-wave interactions (non-linear interactions), dissipation due to breaking, whitecapping and bottom friction. The source terms are presented on the right hand side of the action balance equation (cartesian coordinates) proposed by Hasselmann, et al.(1973):

$$\frac{\delta N}{\delta t} + \frac{\delta}{\delta x}(c_x N) + \frac{\delta}{\delta y}(c_y N) + \frac{\delta}{\delta \omega}(c_\omega N) + \frac{\delta}{\delta \theta}(c_\theta N) = \frac{S}{\sigma} \tag{21}$$

where $N$ is the wave action spectral density ($N = \frac{E}{\sigma}$), $\sigma$ is the relative frequency

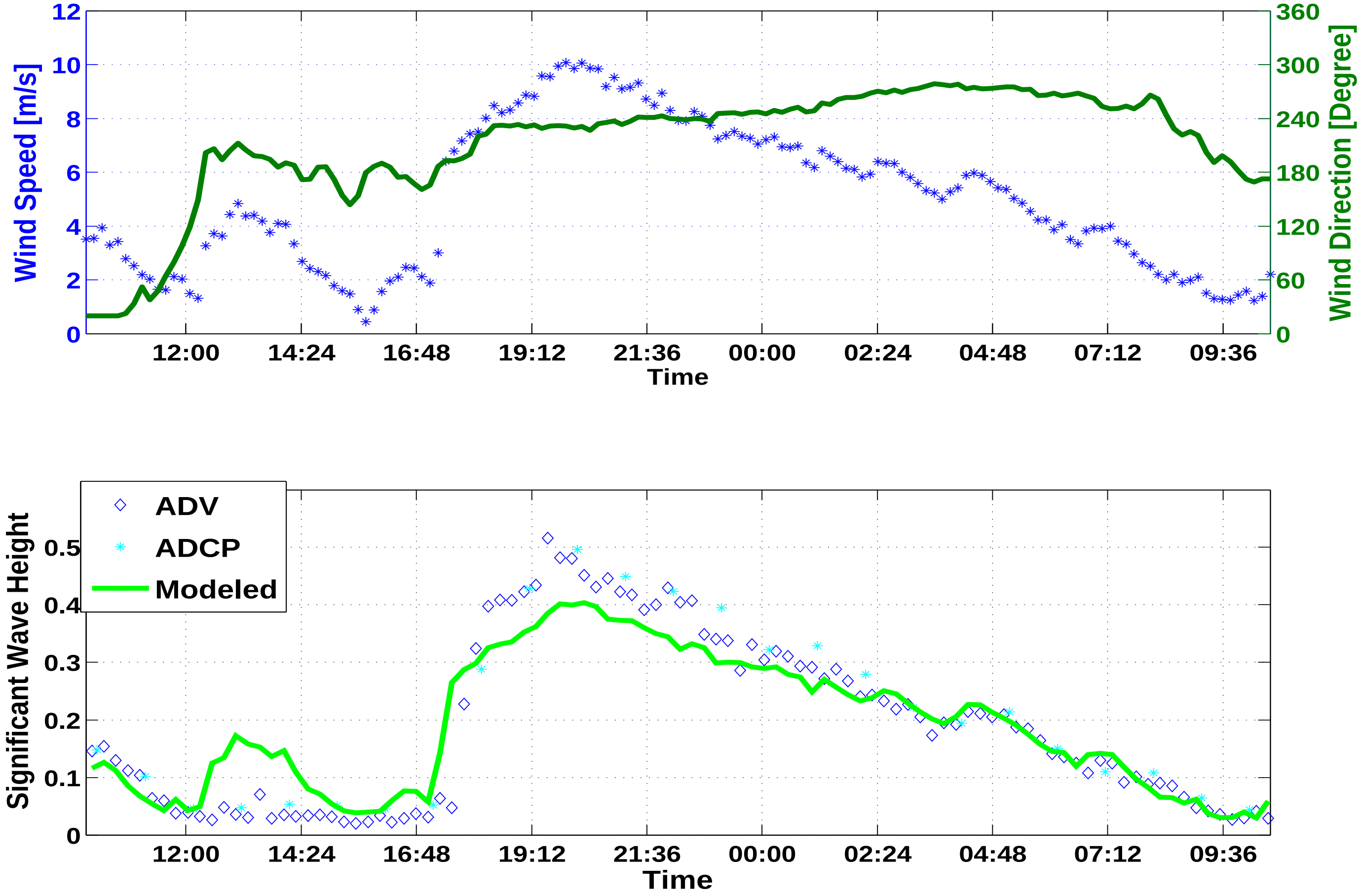

Fig. 17. (Top) Empirically modeled and observed wave heights. The wave heights calculated from the non-dimensional energy follow the trend of the observations; (Middle) Wind speed and wind direction; (Bottom) Wave height vs. wind speed scatter plot. In this case the wind direction is relatively steady throughout the twenty-four sample period and the empirical wave height estimated from Eq. 19 follows the trend of the obervations.

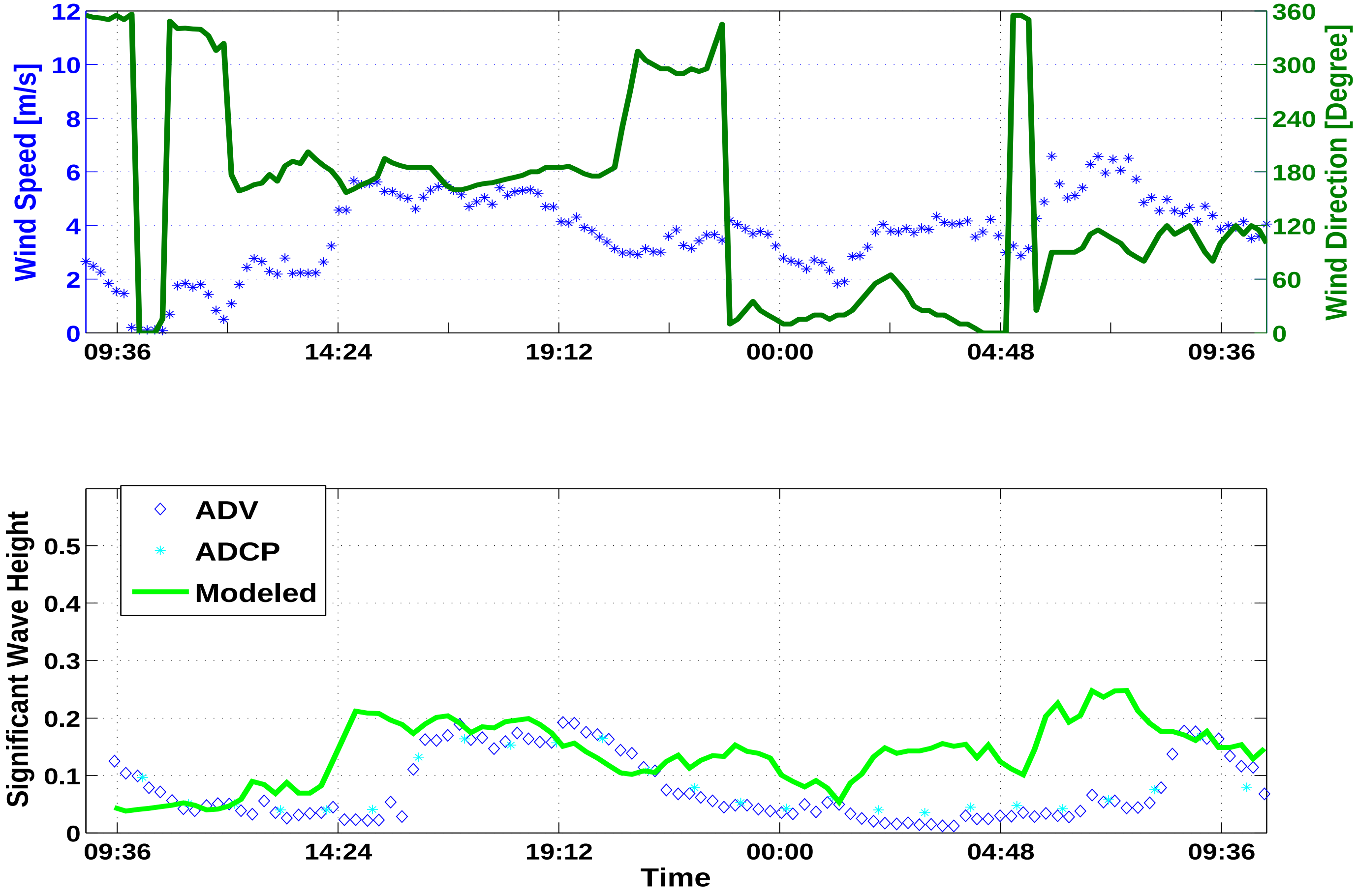

Fig. 18. (Top) Empirically modeled and observed wave heights; (Middle) Wind speed and wind direction; (Bottom) Wave height vs. wind speed scatter plot. The empirical model does not follow the trend of the observations as closely when wind directions shift more often.

(moving with a current), $c$ is the wave propogation speed in the $(x, y, \sigma, \theta)$ space, and $S$ represents the total source terms for generation, dissipation and non-linear interactions ($S = S_{in} + S_{diss} + S_{nl}$), respectively. A general description of the important physical models implemented in SWAN are discussed in the following subsections and are summarized from the SWAN User Manual. For more details refer to the SWAN User's Manual (SWAN, 2006).

### *b. Wind Input*

The wind input in SWAN is expressed as a sum of linear and exponential growth terms:

$$S_{in}(\sigma, \theta) = A + BE(\sigma, \theta) \tag{22}$$

SWAN uses the wind friction velocity defined as $U_*^2 = C_D U_{10}^2$ where $C_D$ is the drag coefficient from Wu (1982):

$$C_D = \begin{cases} 1.2875 \times 10^{-3} & \text{for } U_{10} < 7.5\frac{m}{s} \\ (0.8 + 0.065\frac{s}{m} \times U_{10}) \times 10^{-3} & \text{for } U_{10} \geq 7.5\frac{m}{s} \end{cases} \tag{23}$$

In operational use, the exponential growth term dominates the linear term by at least one order of magnitude (Rogers et al., 2003). The linear term is used to initiate wave action from zero wave energy (Gorman and Neilson, 1999). The linear growth term A was developed by Cavaleri and Malanotte-Rizzoli (1981), and two options are available for the exponential growth term. One is due to Komen (1984) and the second due to Janssen (1991). The linear growth term is:

$$A = \frac{1.5 \times 10^{-3}}{2\pi g^2}(U_* \max[0, \cos(\theta - \theta_w)])^4 H\,, \quad H = \exp\left\{-(\frac{\sigma}{\sigma_{\mathrm{PM}}^*})^{-4}\right\}, \quad \sigma_{\mathrm{PM}}^* = \frac{0.13g}{28U_*}2\pi \tag{24}$$

$\sigma^*_{\mathrm{PM}}$ is the peak frequency of the fully developed sea state according to Pierson and Moskowitz (1964).

### *c. Dissipation Due to Bottom Friction*

Intermediate and shallow water waves with wavelengths equal to one-half of the water depth start to "feel" bottom according to First-order wave theory. The wave energy interacting with the bottom is dissipated through friction, and there are three physical models to describe the dissipation in SWAN: 1) COLLINS model (Collins, 1972), the JONSWAP model (Hasselmann et al, 1973) and the MADSEN model (Madsen et al., 1988). These models all follow the general form:

$$S_{ds.b}(\sigma,\theta) = -C_b \frac{\sigma^2}{g^2 \sinh^2(kd)} E(\sigma,\theta) \tag{25}$$

with $C_b$, a bottom friction coefficient, changing for these three models. The COLLINS $C_b$ is calculated using $C_b = C_f g U_{rms}$ with $C_f = 0.015$, $g$ acceleration due to gravity and $U_{rms}$ is the root-mean square bottom orbital velocity (Collins, 1972). Bouws and Komen (1983) determined $C_b = 0.067$ m$^2$ s$^{-3}$ for wind-seas and MADSEN determined $C_b = f_w \frac{g}{\sqrt{2}} U_{rms}$ where $f_w$ is determined using an eddy-viscosity model based on a bottom roughness length scale.

### *d. Dissipation Due to Whitecapping*

Whitecapping is implemented in SWAN using a model that is dependant on the wave steepness. The formulation of the whitecapping term is:

$$S_{ds.w}(\sigma,\theta) = \Gamma \sigma_* \frac{k}{k^*} E(\sigma,\theta) \tag{26}$$

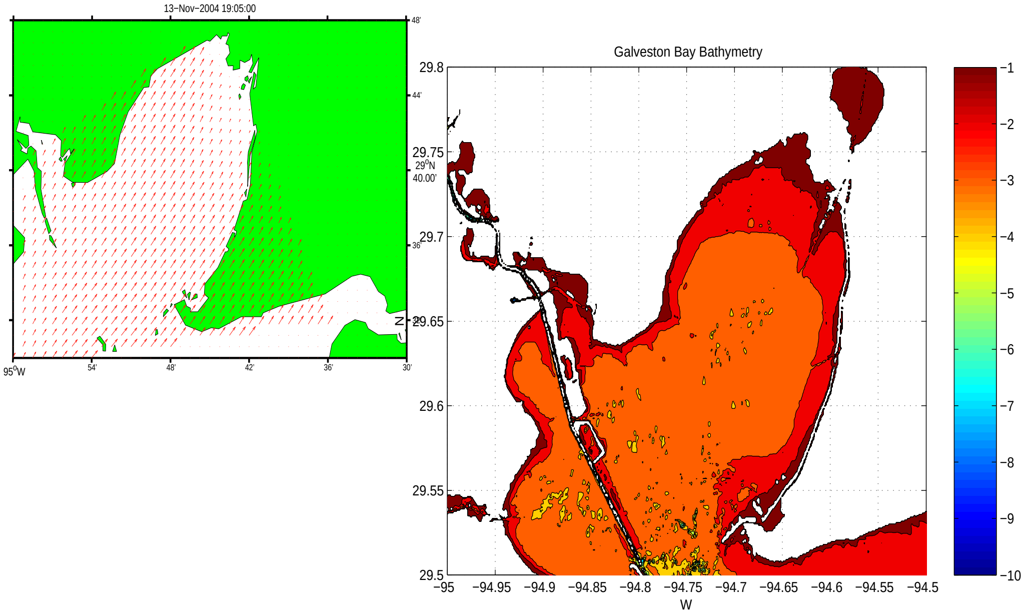

Fig. 19. The upper-left figure shows Trinity Bay with the wind vectors used to force the SWAN model. The wind speeds were taken from four different stations and interpolated to the wind grid. The maximum wind speed was observed at the sampling location and was 7.8 m/s in this snapshot. The larger figure to the right shows the bathymetry of Trinity Bay.

where $\Gamma$ is the wave-steepness, k is the wave number, $k^*$ is the mean wave number and $\sigma^*$ is the mean frequency.

### *e. Dissipation Due to Wave Breaking*

SWAN incorporates a shape-preserving spectral model to account for depth-induced wave breaking. The model is based on the total dissipation measured experimentally from a bore. The formulation is:

$$S_{ds.br}(\sigma,\theta) = -\frac{S_{ds,br,tot}}{E_{tot}} E(\sigma,\theta) \tag{27}$$

where $E_{tot}$ is the total wave energy and $S_{ds,br,tot}$ is the rate of dissipation of $E_{tot}$.

The user controls the activation/deactivation of the source/dissipation terms in SWAN. Past experiences with using and tuning the physical controls were used to guide model runs for Galveston Bay and are listed below:

1. Gorman and Neilson (1999) state “with significant wave heights below 0.5m and periods below 2.4s, triad interactions and depth induced wave breaking are neglible.” This is expected for locally-generated windsea [as noted by Booij et al. (1996)].
2. Zijlema and van der Westhuysen (2005) state that SWAN consistently under-predicts the peak period of wave data, and this problem is under active research.
3. In deep water, whitecapping (dissipation) is “widely believed to be the least accurate” of the physical mechanisms implemented in SWAN and is often used as a closure parameter [Rogers et al. (2003)].
4. “...there is a distinct lower frequency peak in the measured spectra at TR4 and TR5 [2m and 4m depth stations, resepectively], which could not be reproduced in SWAN by local generation.” (Gorman and Neilson, 1999 pp. 214)

### *f. Galveston Bay - SWAN Experiment*

The SWAN model was implemented in both steady-state and unsteady modes in a Galveston Bay computational domain. The computational domain was built with spatial resolution of $\delta x = 140m$ and $\delta y = 140m$. Measured wind speeds and directions were interpolated from four locations on a 100x100m grid and used to force the SWAN model. The wind speeds were converted to ten meters height ($U_{10}$) based on the formulation of the logarithmic wind profile (Smith, 1981) and were input to SWAN. SWAN computes the drag coefficient ($C_D$) and wind friction velocity ($u_*$). An example of the computational grid is plotted in Figure - 19 along with a snapshot of wind vectors on the wind grid.

Bathymetry was input from the NOS archive with 90m resolution and is plotted in Figure 1. Observed currents and bottom friction from the experimental station were input to SWAN on a 100x100m grid. The currents were those observed from the ADV and they were used to calculate bottom friction using the MADSEN model (Madsen et al.,1988). They are distributed homogeneously to each point of the grid (i.e. the bottom friction and currents are homogeneous in space.)

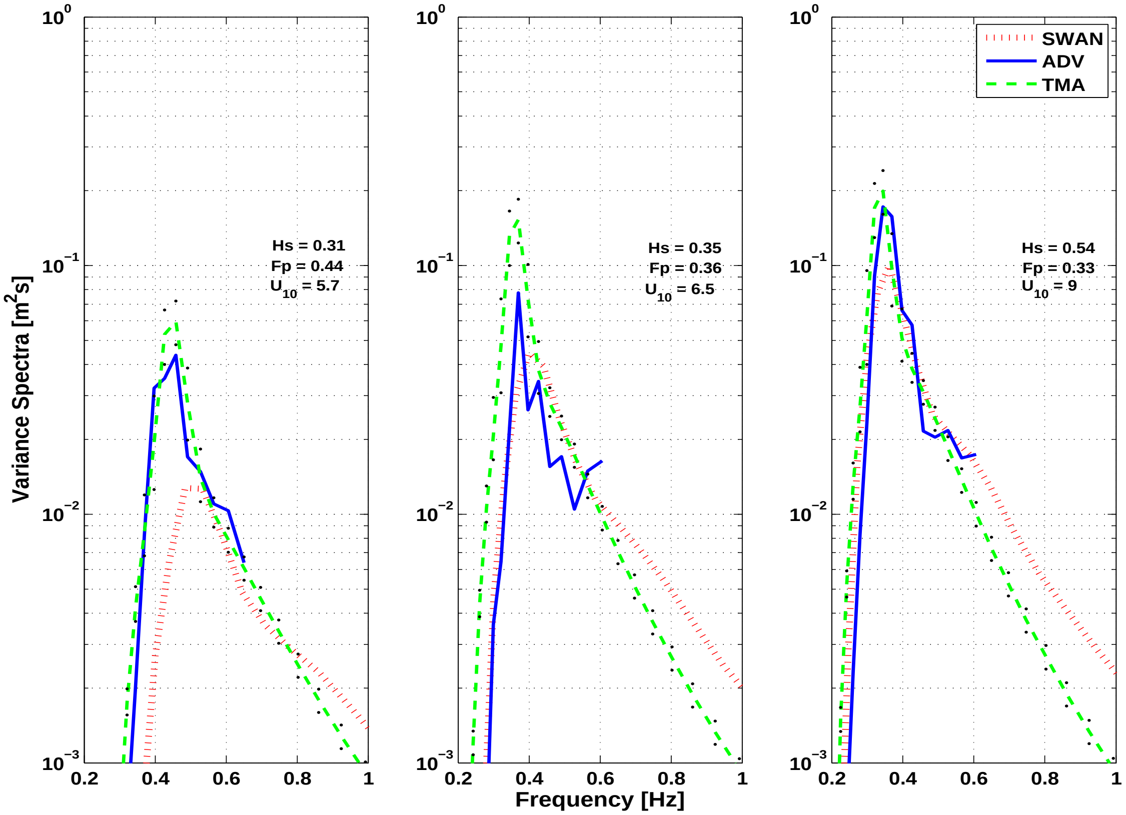

Fig. 20. Three snapshots of the SWAN steady-state spectral output (tick-line) compared to the observed spectra (solid line) and the empirical TMA (——) based on the mean fit parameters for the 13-14, November 2004 cruise.

The SWAN spectral output for the wave growth scenario is presented in Figure f and the output for the decay scenario is plotted in Figure f. In both scenarios, the SWAN output follow the general shape of the observations, but under-predict the observed spectral peaks.

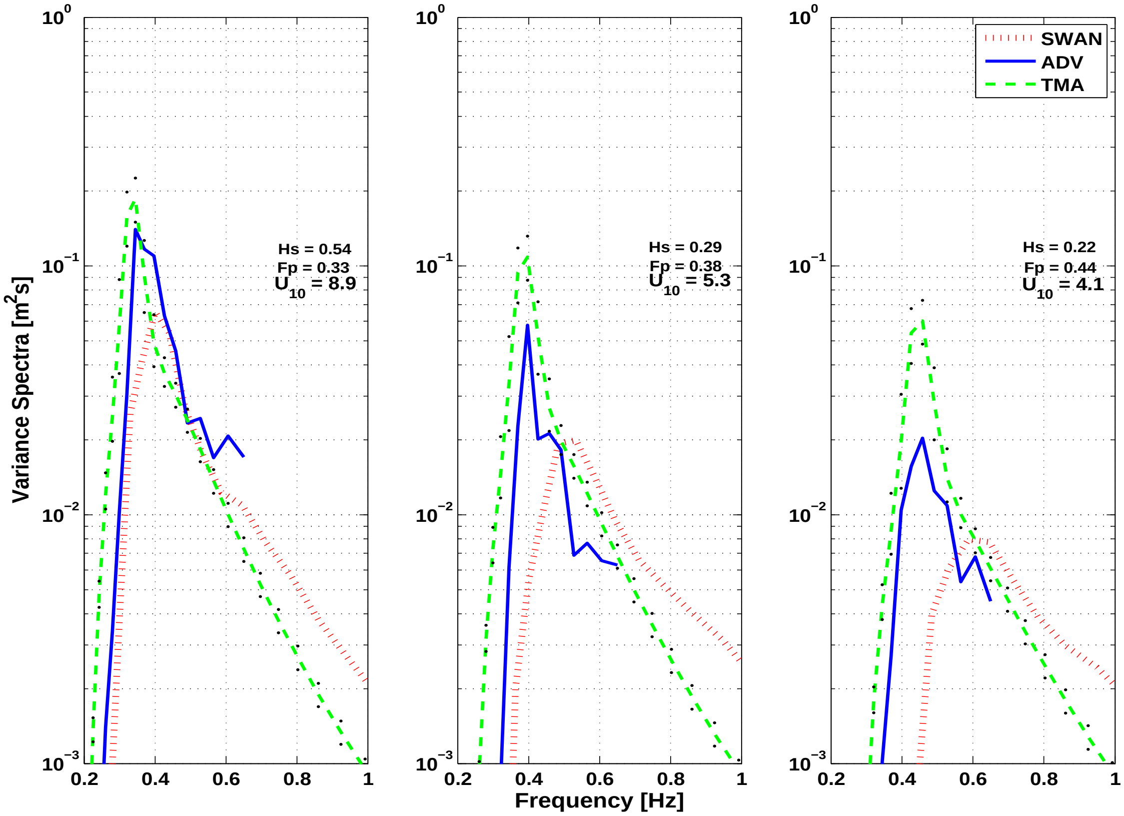

Fig. 21. Similar to f except for the 02-03, April 2005 cruise.

Using SWAN's steady-state mode, modeled spectra were output at the mean sampling location to compare with the observed wave spectra. Two scenarios were chosen to test the Galveston Bay numerical model experiment: 1) wave growth from a sequence of steady-state models with each sequence having increased wind speeds and quasi-steady wind directions (defined here as $\pm 15^o$) and 2) wave decay as a sequence of models with decreasing wind speeds and quasi-steady wind directions. These scenarios are the same used to characterize the TMA spectra (i.e. 13-14, November 2004 (sg05) and 02-03, April 2005 (sg09) in the Wave Characteristics subsection). The observed currents during the wave-growth scenario were in the opposite direction to the wind the entire cruise period. The observed currents changed directions during the period of wave decay in sg09 (Fig. 10). In general, the wave growth scenario represents active generation with little or no change in frequency shifting due to wave-current interactions. The influence of the opposing currents to the bottom friction is unknown since the relative components of bottom frictions due to orbital wave velocites and current velocities were not estimated. The wave decay scenario represents wave energy being dissipated since it is assumed that little or no active wave generation was occuring. The observed currents during the wave decay period were shifting and therefore frequency shifting will occur and again bottom friction conditions were not estimated from the observations. The governing equation for the stationary mode of SWAN is the time invariant form of (21; i.e. $\frac{\delta N}{\delta t} = 0$). This means that the generation and dissipation terms are assumed to yield a steady-state wave field in the computation domain, and the model will carry out computations until the change in wave energy is less than $2\%$ of the previous computation for all grid points. All steady model runs were initiated with zero wave energy. The land and water boundaries are defined in the bathymetry file. Depths above -0.05 m are taken as land, and all wave energy is absorbed at the land boundary.

The non-stationary mode was used to hindcast the time-histories of wave height, direction and peak period for the growth (sg05) and decay (sg09) scenarios. The unsteady model runs were initiated with an initial wave spectrum at each grid point. This was calculated by using the wind speed and direction corresponding to the first computational time-step as the input for a steady mode run. The non-stationary model experiments were run with time steps equal to 10 minutes. There was no observable difference between runs with $\delta t$ = 20 min, 10min, 5min and 1min. In the unsteady mode, the transport of local wave spectrum with time makes more physical sense than the steady-state scenarios because the wave conditions are in an unsteady field of currents and wind speed. The total spectral energy and thus the significant wave height is reproduced almost excactly for both wave scenarios (Figs. 22 & 24). Figure f shows and example of the significant waveheight output over the computational domain at 22:25:25 [CST] on 13-November 2004. In both cases (sg05 and sg09), the peak period is underpredicted. This has been recognized in the literature and it is assumed the result of the non-linear interaction terms (Gorman and Neilson, 1999; Zijlema and van der Westhuysen (2005). The wave directions are in agreement with the wind direction. This was observed visually while sampling.

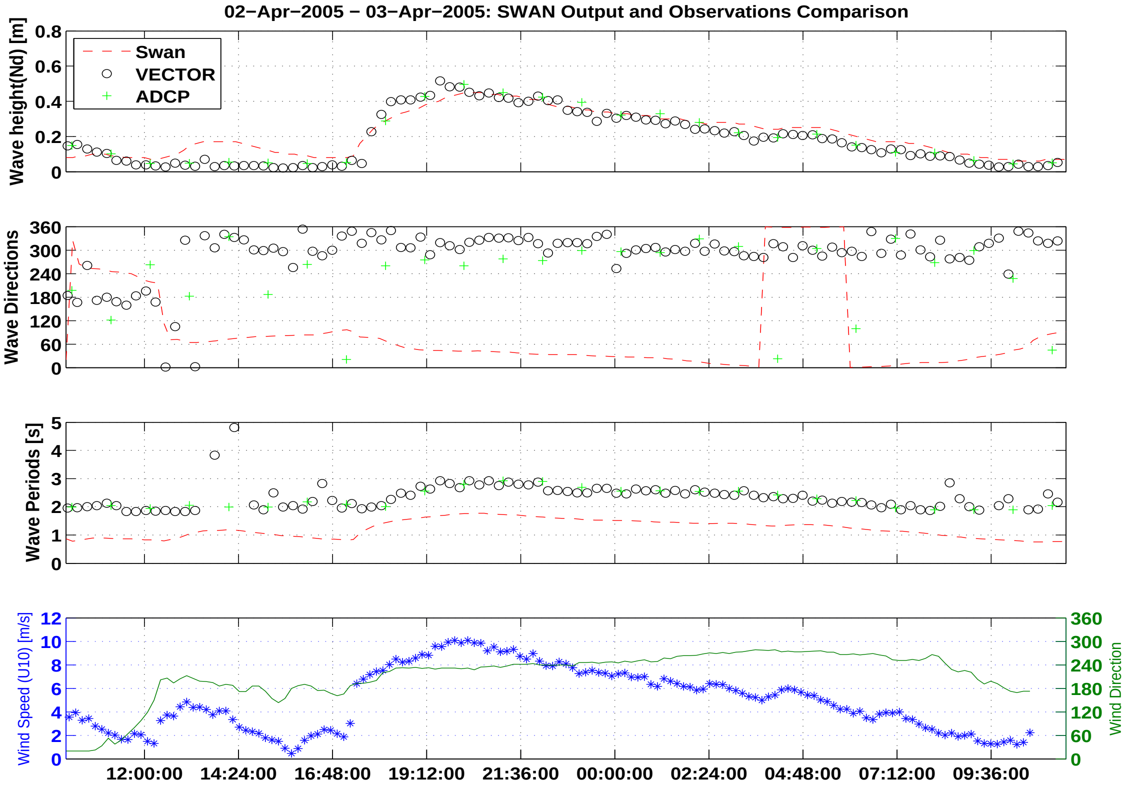

Fig. 22. SWAN non-stationary model output and observations: $H_s$ output (line) overplotted with observed $H_s$ (○ ADV; + ADCP; Upper panel); model wave direction and observed wave direction (middle-upper, same key); modeled peak frequency and observed peak frequency (middle-lower) and the wind speed (left hand axis) and wind direction (left-hand axis) used to force the model (lower).

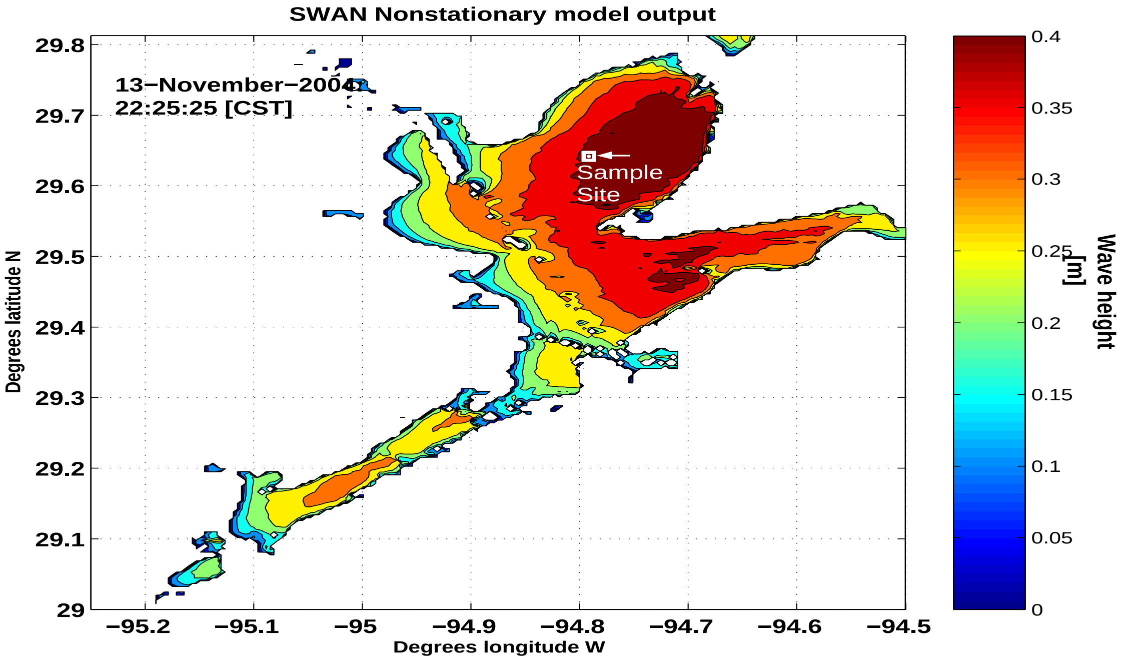

Fig. 23. A snapshot of hindcast wave height contours in Galveston Bay for 13-14 November 2004. The computational domain is $\Delta x = \Delta y = 140$ m.

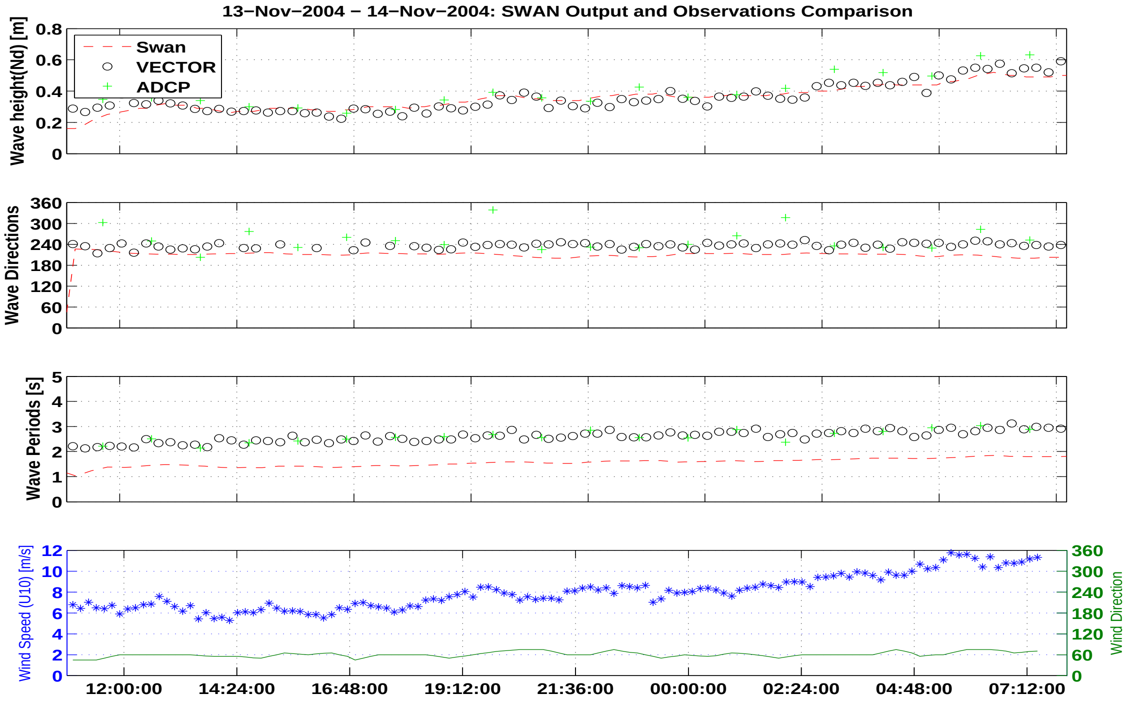

Fig. 24. (Upper) Time series of observations and model wave heights, (Middle) observational and model wave directions and wind speeds and directions (Lower) for 13-14 November 2004.

# 5. CONCLUSIONS

Ten twenty-four hour deployments of two current meters and meteorological sensors yielded wave height, period and directional data from a single location in the shallow estuary, Galveston Bay. GB waves are described with the shallow water TMA spectrum using mean shape paramters:$\alpha = 0.016$, $\gamma = 4.26$, $\sigma_a = 0.063$, $\sigma_b = 0.089$ for a given wave height and period. The observed data were compared with empirically and numerically modeled wave heights, periods and directions. The range of the empirical model is extended to deeper water (from 0.5 - 2m to GB depths of 3.5m) and the GB wave observations compared to the Lake George (YVa and YB) observations are a second verification of the universal applicability of the non-dimensional wave relations since the data were collected using different observation techniques in two different shallow bodies of water. Both the TMA fit and the empirical model based on the asymptotic limit of wave growth in shallow fetch-limited water has direct application to current engineering projects in the bay. Specifically, a marsh restoration project in West Bay. The observations in GB were from 3m depth, and it is assumed that the empirical relation will work in the more shallow depth ranges observed by YVa and YB.

The SWAN model was compared to wave observations at a single location during quasi-steady wind-directions (i.e. $\pm 15^o$) and changing wind speeds (increasing and decreasing winds). The model results during steady-state runs were output as a sequence of growing and decaying wave spectra. In general, the model spectra did not reproduce the observed wave spectra. The model spectra were generally wider and less peaked than the observations, and during wind speeds less than 6 m/s the model output yielded peak periods almost one-half times the observed peak. Assuming the observed spectrum is representative of the physical processes describing the wave generation and dissipation, the generation and dissipation terms are not properly represented in the model experiment presented. In the unsteady mode, the wave spectra are also not represented, however the total wave energy is captured. The significant wave heights (calculated from the total energy) reproduce the observations almost exactly for the increasing and decreasing wind scenarios. The peak period is consistently under-predicted by nearly one-half times the observed period and the modeled direction is in general agreement with the observed wave direction.

In conclusion, the Galveston Bay waves were descibed using three methods: an empirical spectrum, an empirical wave-hindcast model and a numerical model (SWAN) representing wave generation and dissipation processes in time and space. Given a wind speed, fetch and depth, the maximum wave height and peak period can be estimated from the empirical wave-hindcast model. Using these estimates the wave spectrum can be accurately represented using the TMA model with the mean shape parameters and 95% confidence determined in the results. This has direct application for determining the energy near the bottom boundary for any sediment transport, nutrient transport and offshore structure applications (e.g. wind turbines, gas platforms). The SWAN model accurately predicts the total wave energy in the GB computational domain. The spectral shape is not well represented in both the steady and unsteady modes and therefore does not accurately produce the physical processes assumed to underly the wave spectrum. The empirical model is currently a more useful tool to describe the waves in Galveston Bay and it is more time efficient than the numerical model, SWAN.

# REFERENCES

Bishop C.T. and M.A. Donelan, 1987: Measuring waves with pressure transducers. *Coastal Engineering,* **11**, 309–328.

Bouws E., H. Gunther, W. Rosenthal and C.L. Vincent, 1985. Similarity of the wind wave spectrum in finite depth water 1. Spectral form. *Journal of Geophysical Research*, **90**, 975-986.

Bottema, M., J.P. de Waal, and E.J. Regeling. 2002: Some applications of the Lake Ijssel/Lake Sloten wave data set. *Proc. 28th International Conf. Coastal Engineering 2002.* Ed. J.M. Smith. Cardiff, Wales. **1**, 413–425.

Bretschneider, C.L., 1954: Field investigation of wave energy loss in shallow water ocean waves. Tech. Memo. No. 46. U.S. Beach Erosion Board

Bretschneider, C.L. and Reid, R.O., 1954: Modification of wave height due to bottom friction, percolation, and refraction, Tech. Memo. No. 45. U.S. Beach Erosion Board

CERC, 1984: *Shore Protection Manual*. U.S. Army Coastal Engineer Research Center. 2 Volumes.

Chen, Q., H. Zhao, K. Hu, and S.L. Douglass.,2005: Prediction of wind waves in a shallow estuary. *Journal of Waterway, Port, Coastal and Ocean Engineering*. **131:4**, 137–148.

Donelan, M.A., J.Hamilton and W.H.Hui.1985:Directional spectra of wind-generated waves. *Philosophical Transactions of the Royal Society London*, **A315**, 509-562.

Gordon, L. and A. Lorhmann. 2001: Near-shore Doppler current meter spectra, Ocean wave measurement and analysis. *Proc. of the 4th International Symposium, WAVES 2001*, September 2-6, 2001, San Francisco; edited by Billy L. Edge and Michael Hemsley.

Gorman, R.M. and C.G. Neilson, 1999: Modelling shallow water wave generatiion and transformation in an intertidal estuary. *Coastal Engineering*, **36**, 187-217.

Hasselmann, K.; Barnett, T. P.; Bouws, E.; Carlson, H.; Cartwright, D. E.; Enke, K.; Ewing, J. A.; Gienapp, H.; Hasselmann, D. E.; Kruseman, P.; Meerburg, A.; Muller, P.; Olbers, D. J.; Richter, K.; Sell, W.; Walden, H. 1973: Measurements of wind-wave growth and swell decay during the joint North Sea wave project (JONSWAP). *Deutschen Hydrographischen Zeitschrift Supplement A* **8**: 1-95.

Ijima, T. and Tang,F.L.W., 1966. Numerical calculations of wind waves in shallow water. *Proc. 10th Conf. on Coastal Engineering*, Tokyo. ASCE, New York, **2**, 38–45.

Janssen, P.A.E.M., 1991: Quasi-Linear theory of wind-wave generation applied to wave forecasting, *Journal of Physical Oceanography*, **21**, 1631 - 1642.

Jin, K.. and Z. Ji, 2001: Calibration and verification of a spectral wind-wave model for Lake Okeechobee. *Ocean Engineering*, **28**, 571–584.

Kitaigorodskii, S. A. 1962: Applications of the theory of similarity to the analysis of wind-generated wave motion as a stochastic process. *Bulletin Academy of Sciences, USSR Geophysics Series* **5**: 410–420.

Kitaigorodskii, S. A., V.P. Krasitskii and M.M. Zaslavskii: 1975: On Phillips' theory of equilibrium range in the spectra of wind-generated gravity waves *Journal of Physical Oceanography* **1**: 73-80.

Kitaigorodskii, S. A.: 1983: On the theory of the equilibrium range in the spectrum of wind-generated gravity waves *Journal of Physical Oceanography* **13**: 816–827.

Lin, W., L.P. Sanford, and S.E. Suttles., 2002: Wave measurement and modeling in Chesapeake Bay. *Continental Shelf Research*, **22**, 2673 – 2686.

Liu, P.C., 1983: A representation for the frequency spectrum of wind-generated waves. *Ocean Engineering*, **6**, 429-441.

Liu, P.C., 1987: Assessing wind wave spectrum representations in a shallow lake. *Ocean Engineering*, **14**, 39-50.

MASE-SWAN, 2006: Swan Model Output:
$http://www.tamug.edu/mase/Wave_file/Galveston.htm$.

Pierson W.J. and L. Moskowitz 1964:A proposed spectral form for fully developed wind seas based on the similarity theory of S.A. Kitaigorodskii. *Journal of Geophysical Research*, **69**, 5181–5190.

Phillips, O.M. 1958: The equilibrium range in the spectrum of wind-generated waves. *Journal of Fluid Mechanics*, **4**, 426 – 434

Ravens, T. 2006: The design of erosion resistant marshes. *Texas Sea Grant Researcher Conference*, Abstract.Galveston, Texas. October 5, 2006.

Rogers, W.E., P.A. Hwang and D.W. Wang, 2003: Investigation of wave growth and decay in the SWAN model: Three regional-scale applications. *Journal of Physical Oceanography*, **33**, 366–389.

Smith, M. J., C.L. Stevens, R.M. Gorman, J.A. McGregor, and C.G. Neilson, 2001: Wind-wave development across a large shallow intertidal estuary: a case study of Manukau Harbour, New Zealand. *New Zealand Journal of Marine and Freshwater Research*, **35**: 985–1000

Smith, J.M. 2002: Wave pressure gauge analysis with current. *Journal of Waterway, Port, Coastal and Ocean Engineering*, **128:6**, 271–275.

Sverdrup H.U., and W. H. Munk, *Wind, Sea and Swell; Theory of Relations for Forecasting*, U.S. Hydrographic Office (H.O.) Pub. No. 601, 1947

SWAN, 2006. *The SWAN User Manual* SWAN Cycle III Version 40.51. Delft University of Technology.

Young, I. R. and A.V. Babanin, 2005: The form of the asymptotic depth-limited wind wave frequency spectrum. *Journal of Geophysical Research* **111**: C06031

Young, I. R. and L.A. Verhagen, 1996a: The growth of fetch limited waves in water of finite depth. 1. Total energy and peak frequency. *Coastal Engineering* **29**: 47–78.

Young, I. R. and L.A. Verhagen, 1996b: The growth of fetch limited waves in water of finite depth. 2. Spectral evolution. *Coastal Engineering* **29**: 79–99.

Zijlema,M. and A.J. van der Westhuysen, 2005: On convergence behaviour and numerical accuracy in stationary SWAN simulations of nearshore wind wave spectra. *Coastal Engineering*, **52**, 237–256.

# APPENDIX A

The time histories of wind vectors (upper) current vectors (ADCP (upper middle); ADV (lower middle) and water depth (lower) showing the tidal changes with time (Figures - 25 - 33. These plots are for reference.

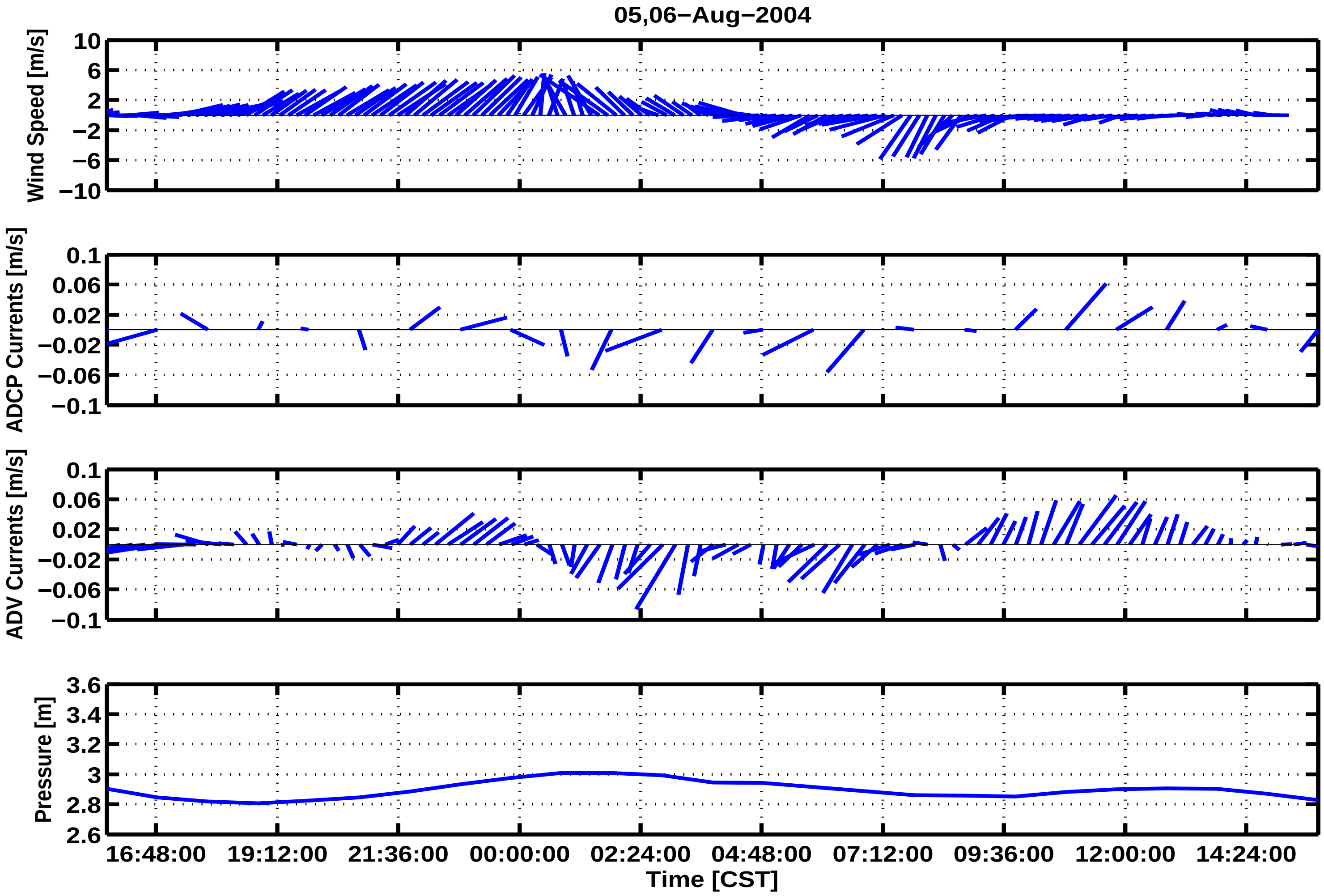

Fig. 25. Time-series of wind vectors (upper), burst-averaged ADV current velocities (middle-upper), burst-averaged ADCP current velocities (middle-lower) and burst-averaged (every 15 min) depth from the ADV during 05–06, August 2004.

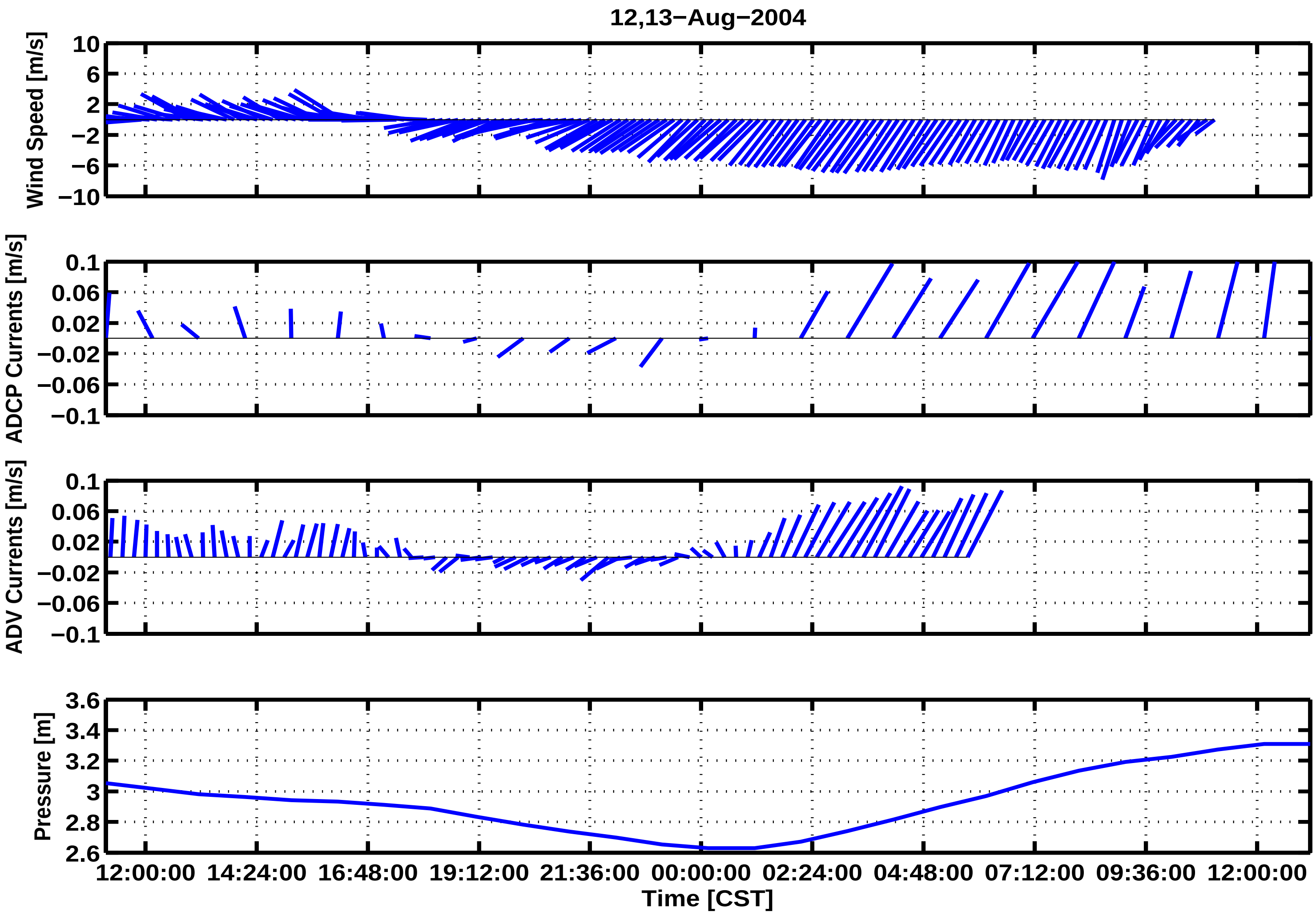

Fig. 26. Similar to Fig. 25 except observed during 12–13, August 2004.

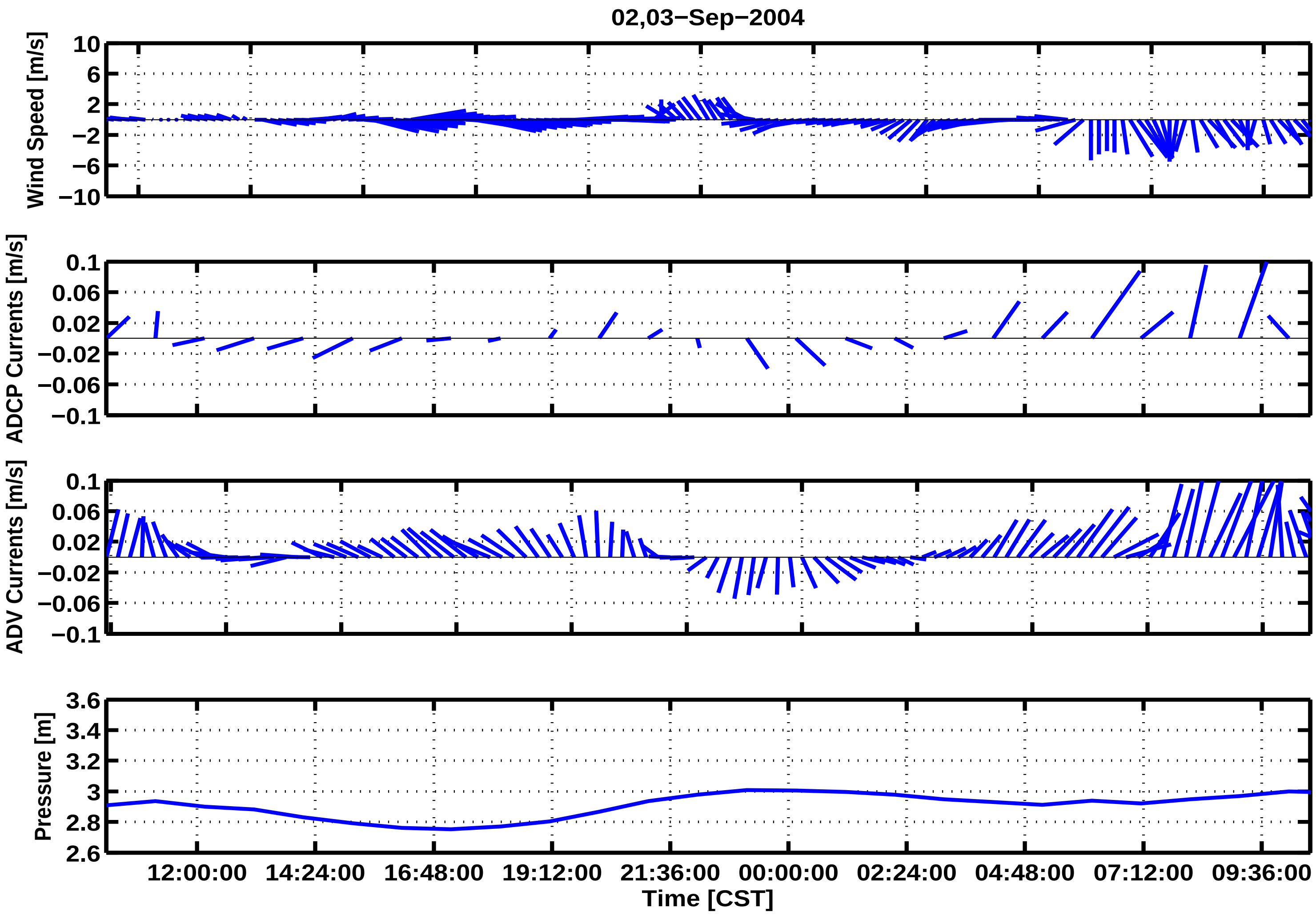

Fig. 27. Similar to Fig. 25 except observed during 02–03, September 2004.

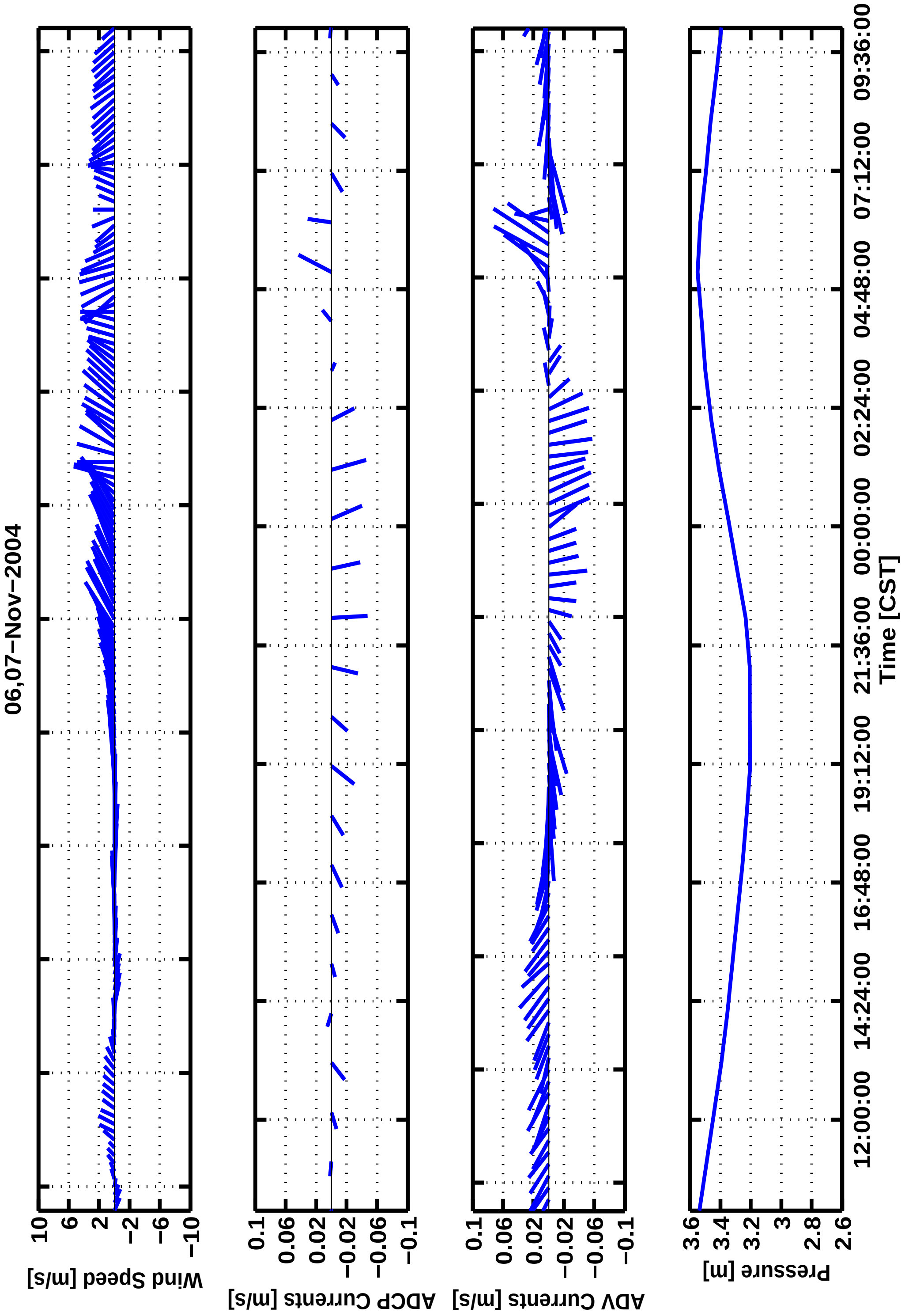

Fig. 28. Similar to Fig. 25 except observed during 06–07, November 2004.

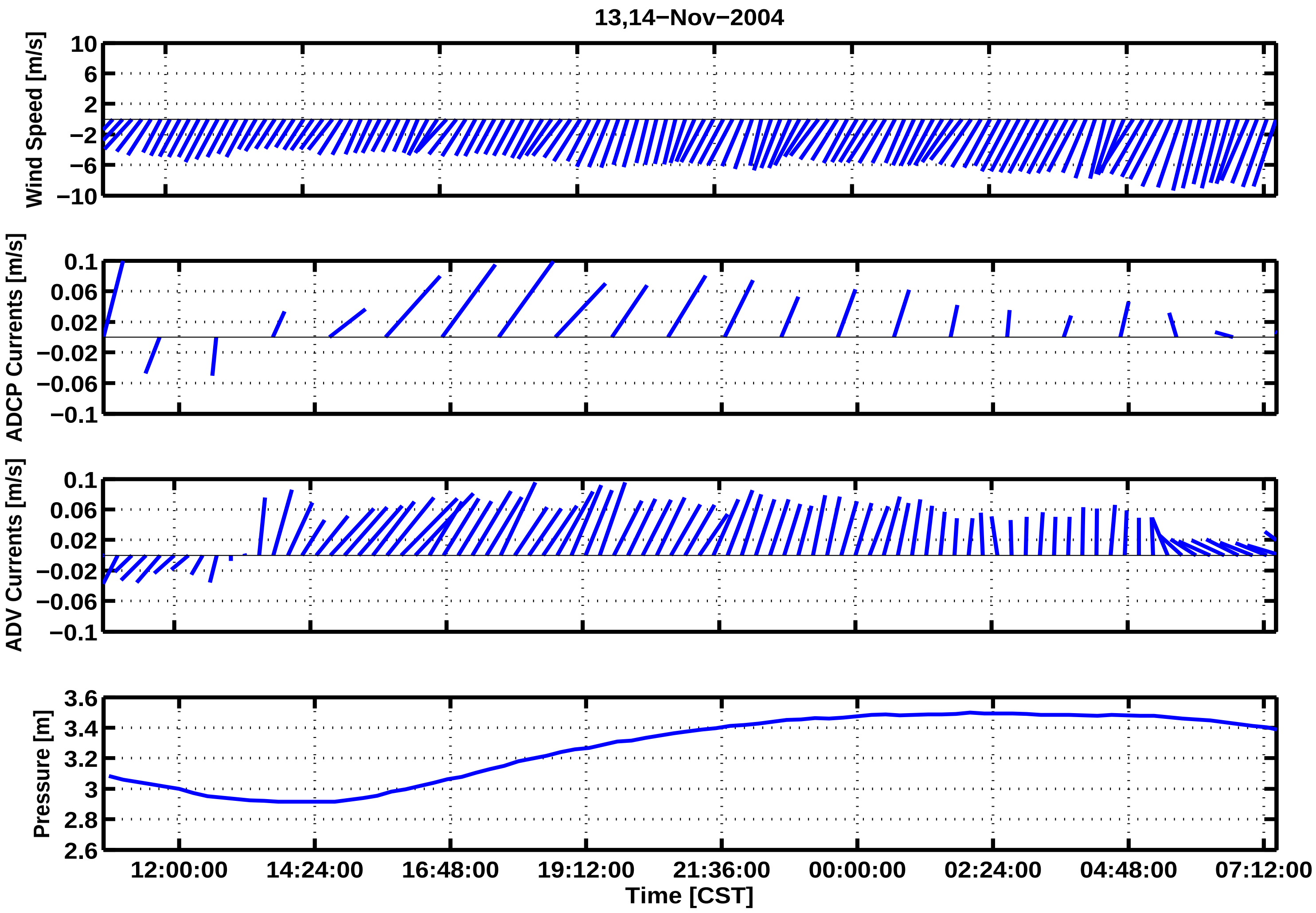

Fig. 29. Similar to Fig. 25 except observed during 13–14, November 2004.

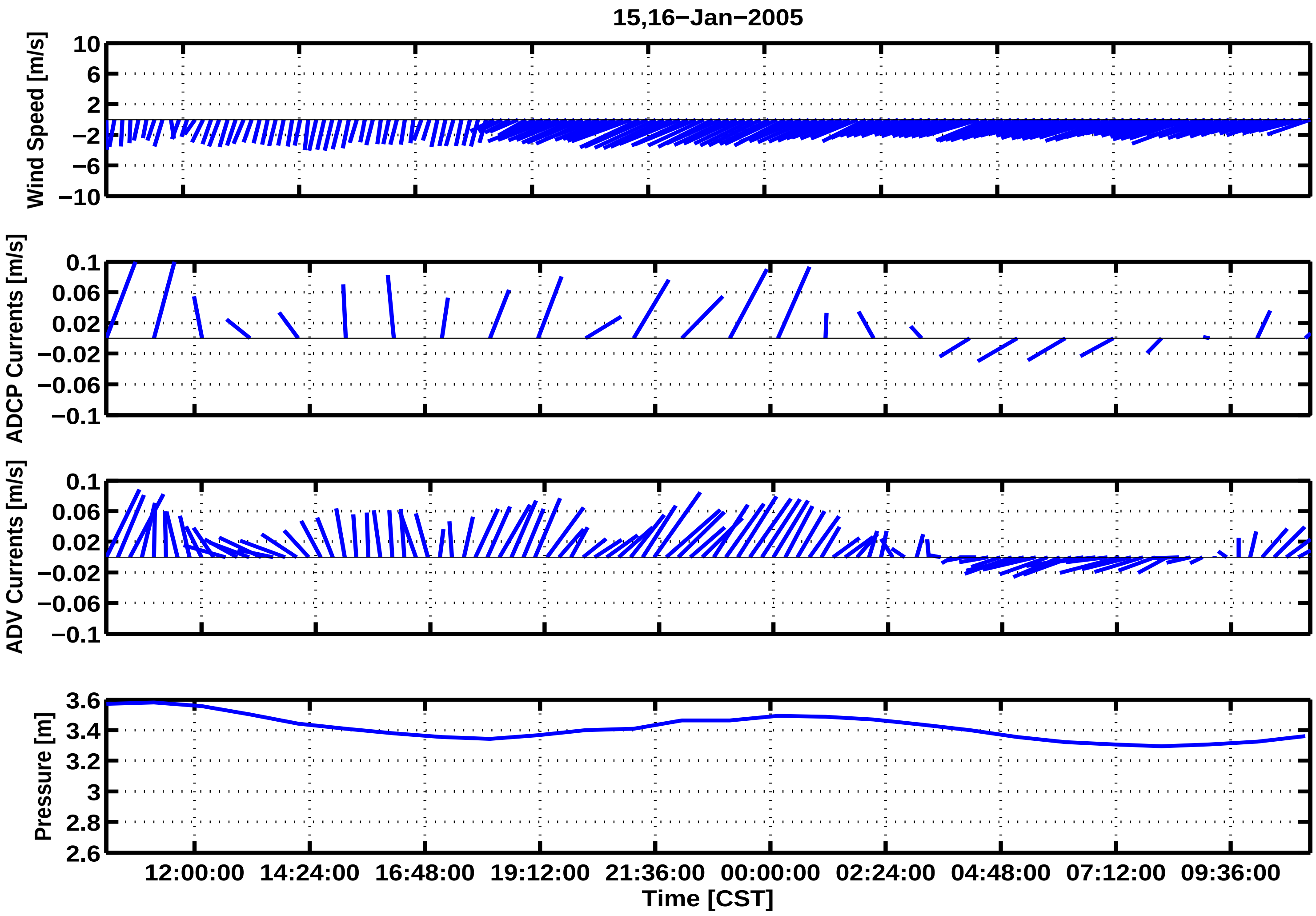

Fig. 30. Similar to Fig. 25 except observed during 15–16, January 2005.

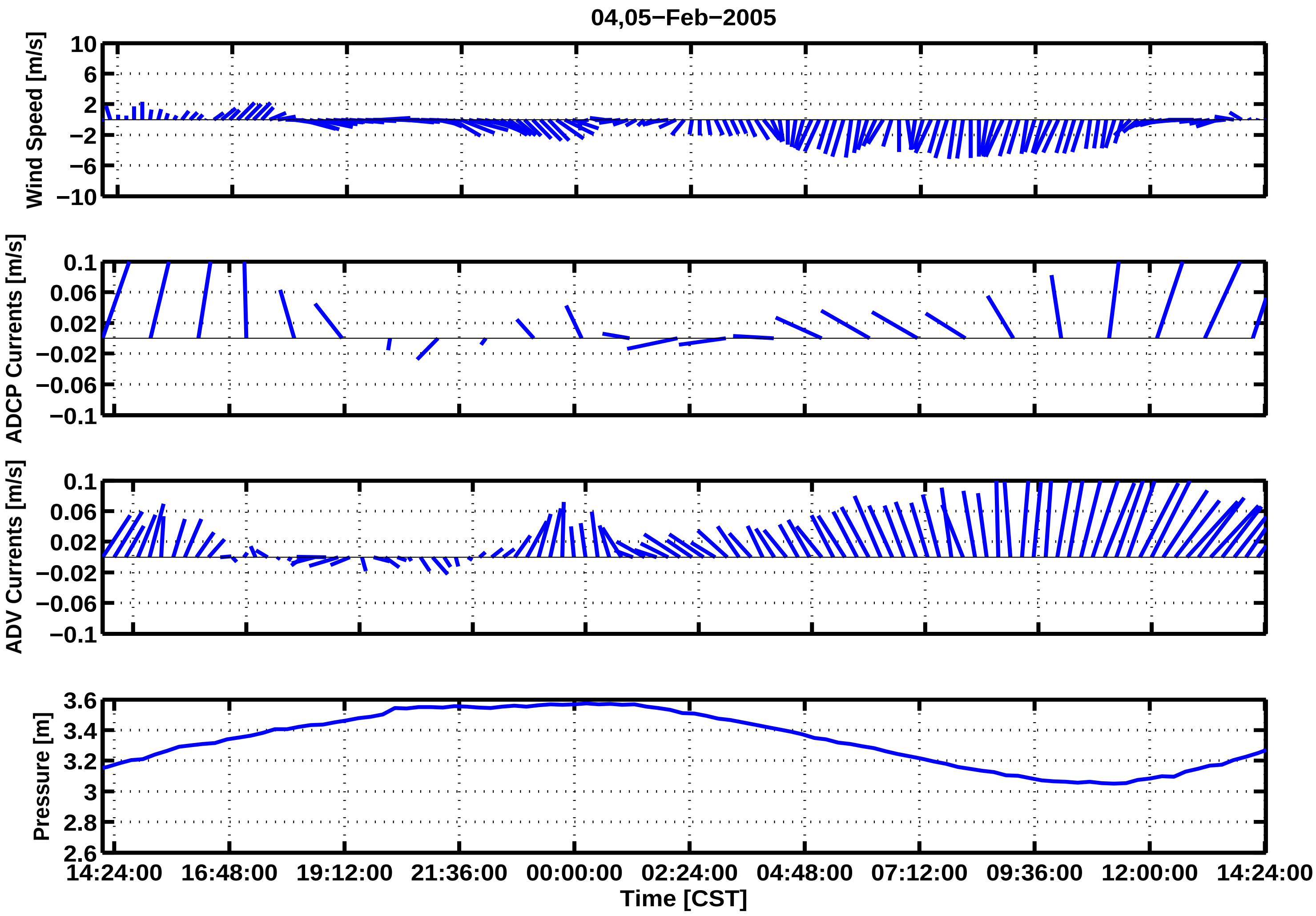

Fig. 31. Similar to Fig. 25 except observed during 04–05, February 2005.

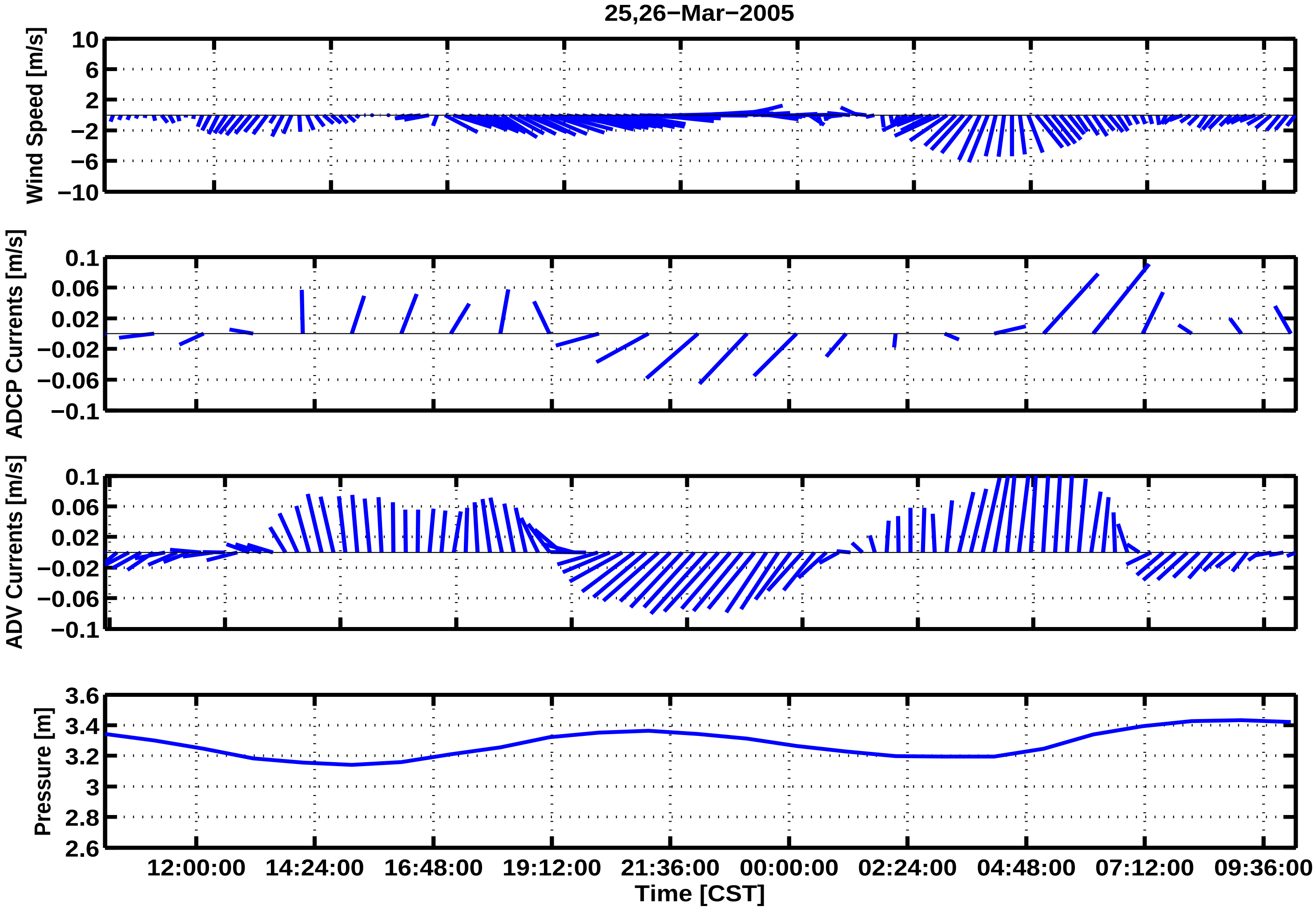

Fig. 32. Similar to Fig. 25 except observed during 25–26, March 2005.

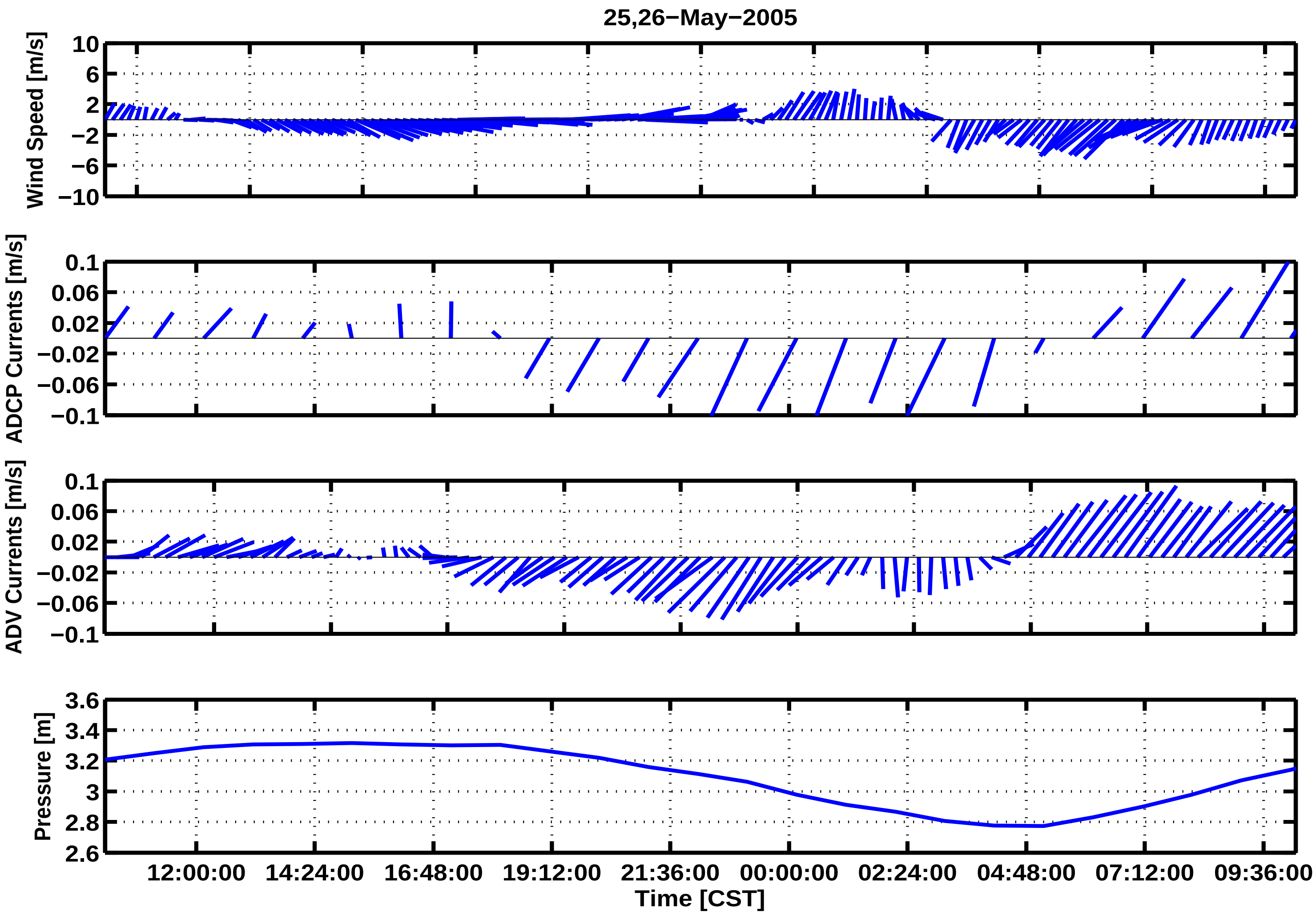

Fig. 33. Similar to Fig. 25 except observed during 25–26, May 2005.

# APPENDIX B

The time histories of wave height, period and direction estimates are presented in this appendix (Figures - 35 - 43. The wind speeds are overplotted on the wave height panel (upper) and wind directions overplotted with wave direction estimates (lower panel). In general the wave heights and wind speeds correlate and the wave directions correlate with the wind directions. This is a simplified verification of the wind-wave estimates in Galveston Bay.

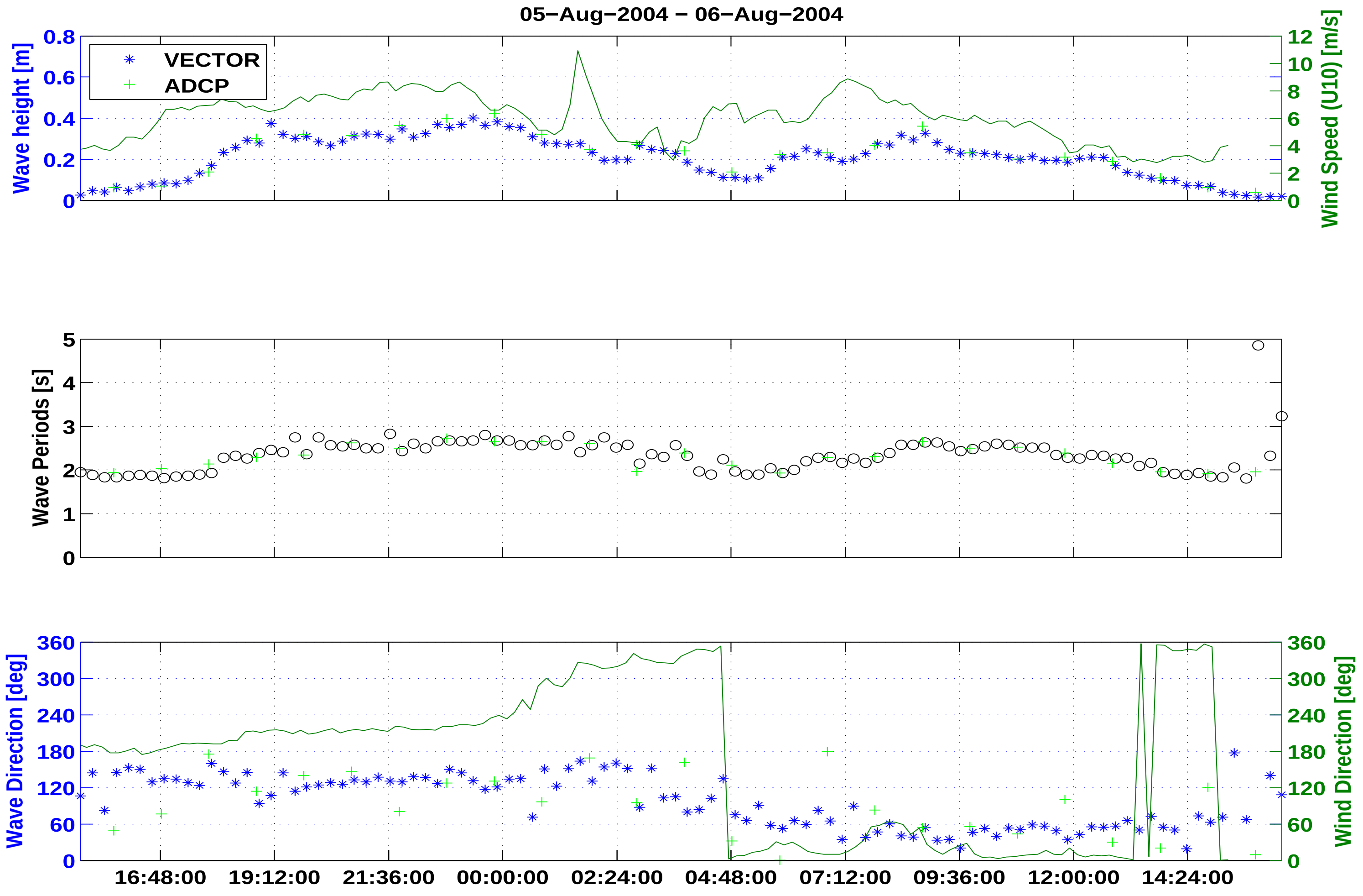

Fig. 34. Time series of observed wind speeds (solid line-right-hand axis) and $H_s$ (ADV, $\circ$; ADCP, $+$; Upper), peak period [s](middle), and wind (line) and wave directions (lower). The ADV and ADCP markers are the same for the direction subplot. The observations were made 05-06, August 2004.

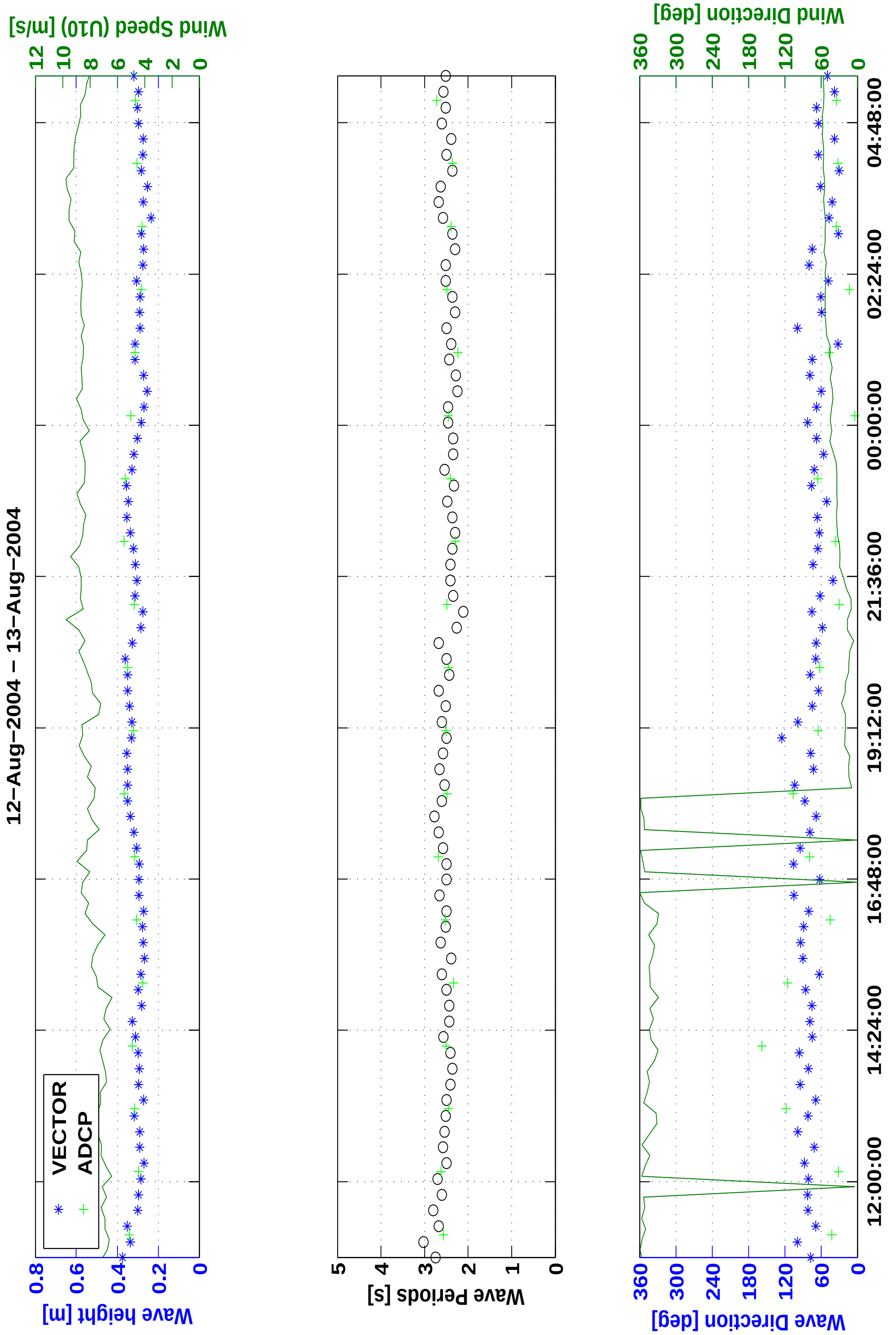

Fig. 35. Similar to Fig. 34 except observed during 12–13, August 2004.

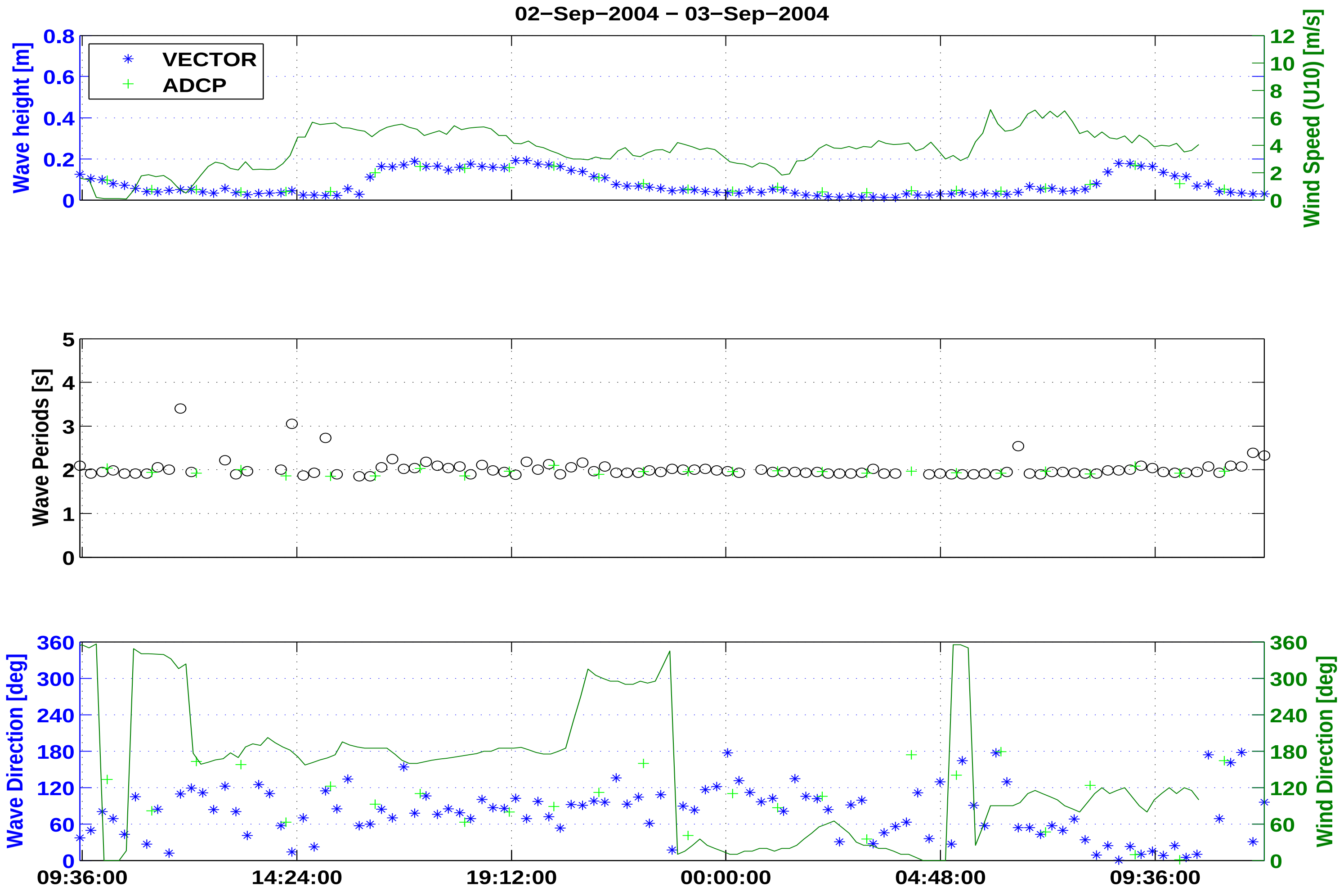

Fig. 36. Similar to Fig. 34 except observed during 02–03, September 2004.

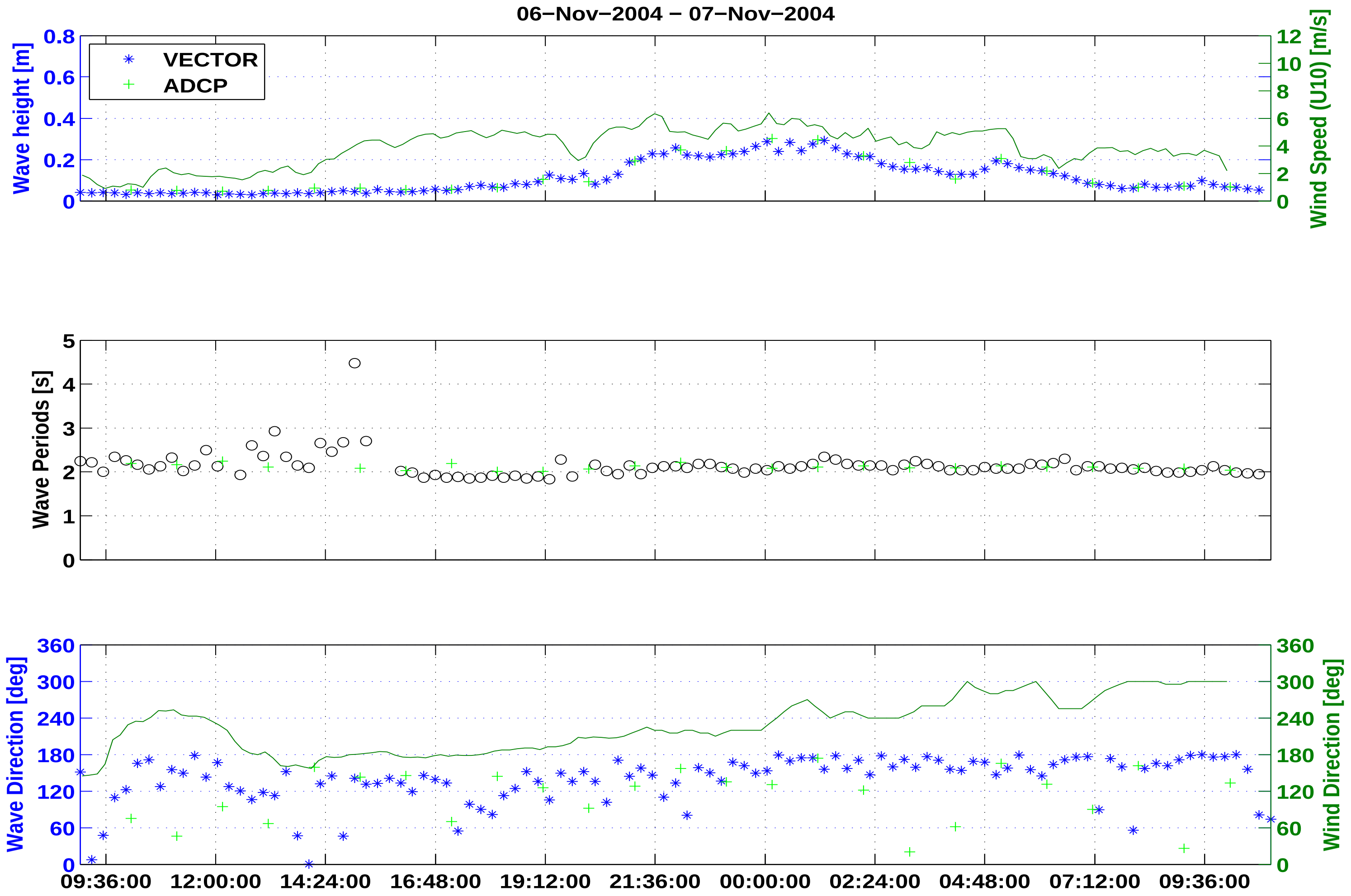

Fig. 37. Similar to Fig. 34 except observed during 06–07, November 2004.

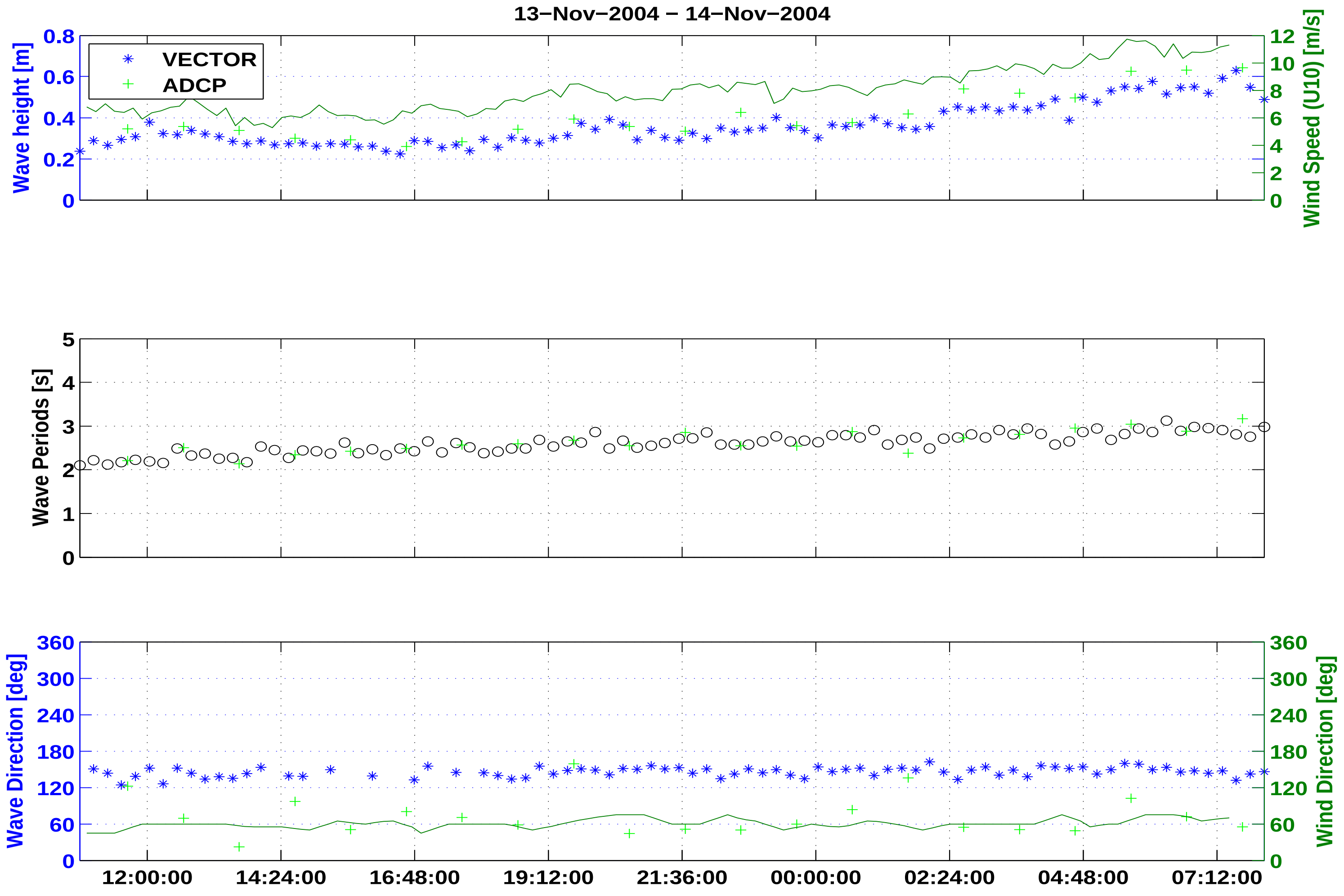

Fig. 38. Similar to Fig. 34 except observed during 13–14, November 2004.

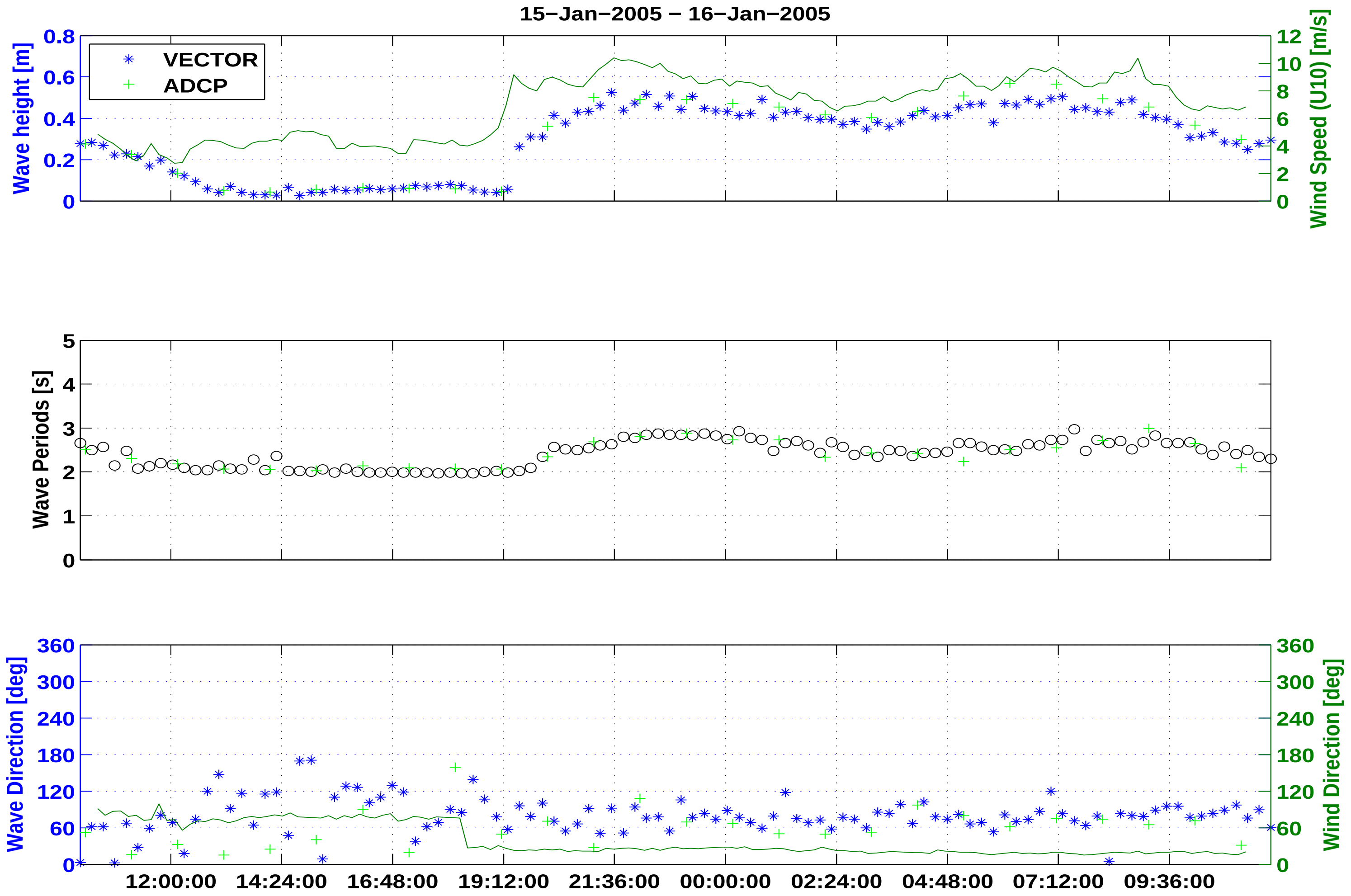

Fig. 39. Similar to Fig. 34 except observed during 15–16, January 2005.

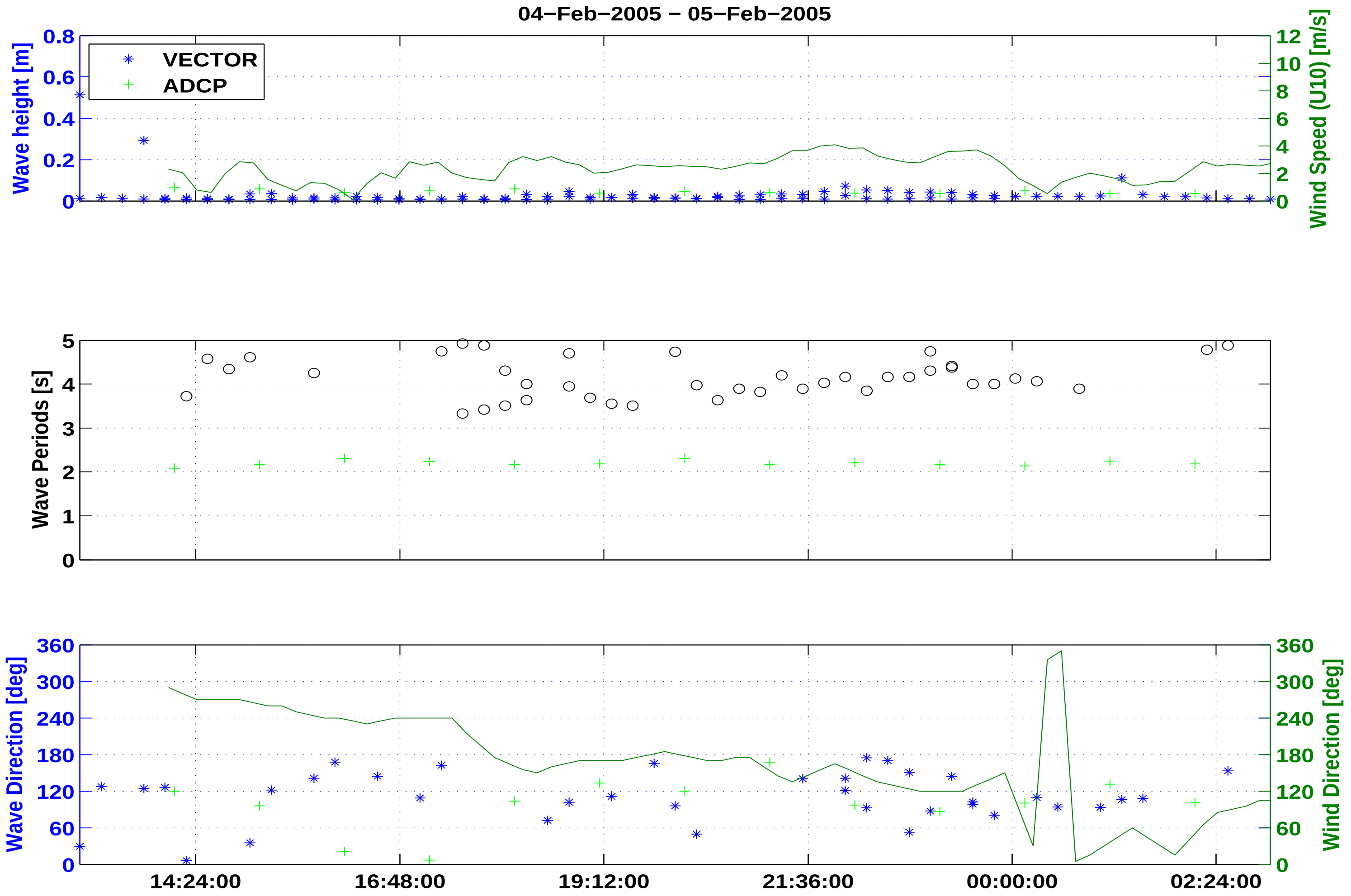

Fig. 40. Similar to Fig. 34 except observed during 04–05, February 2005.

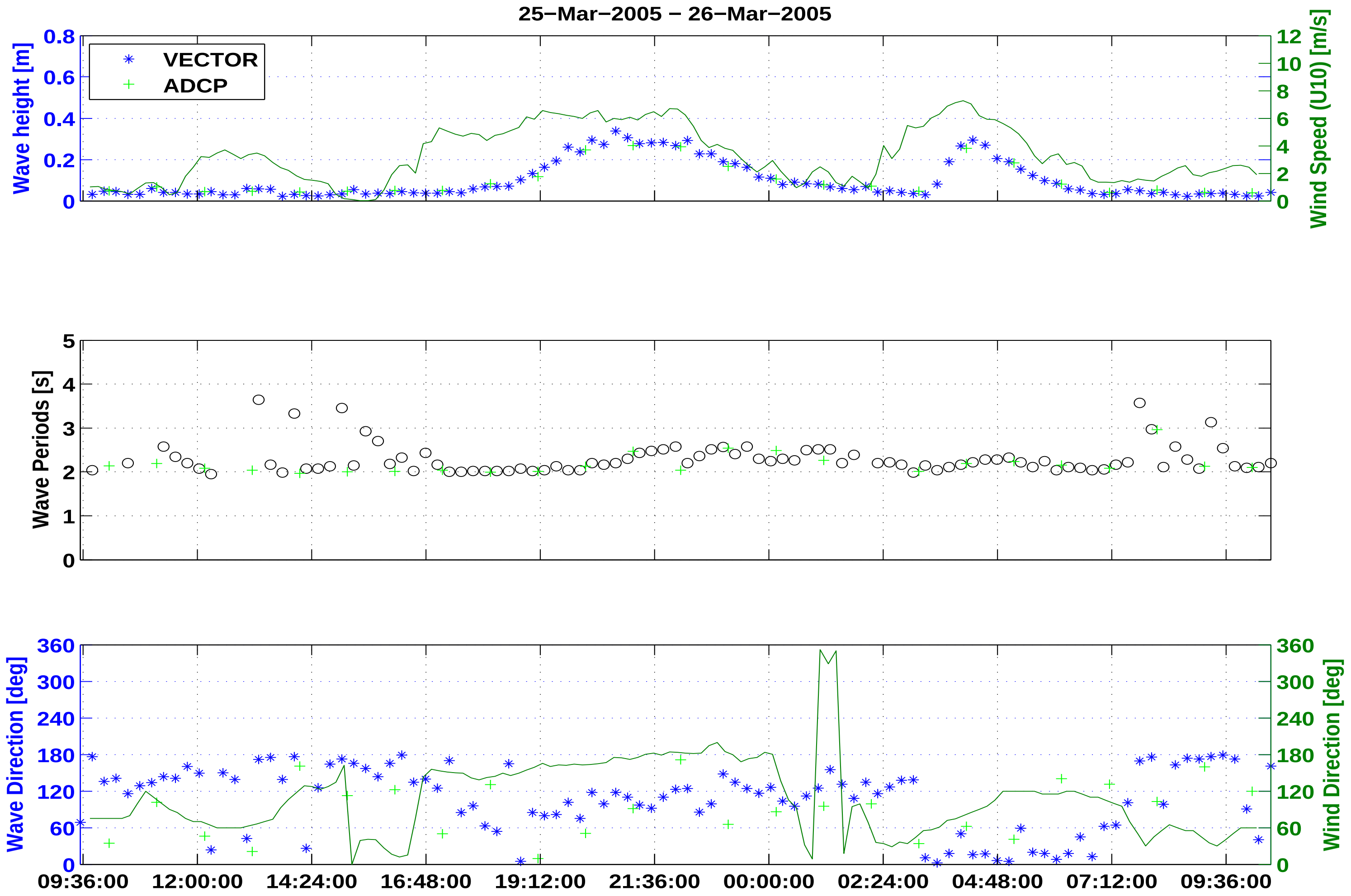

Fig. 41. Similar to Fig. 34 except observed during 25–26, March 2005..

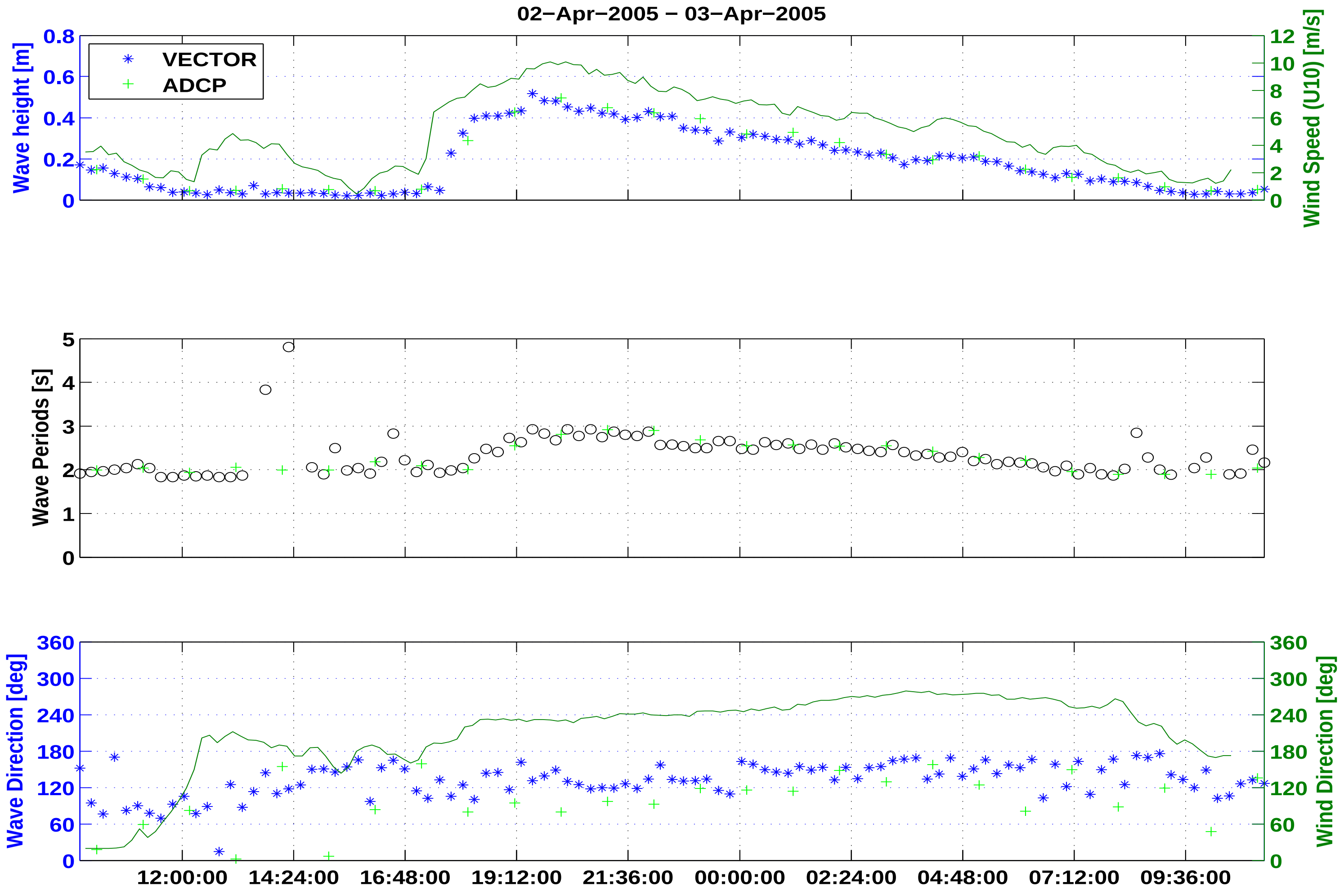

Fig. 42. Similar to Fig. 34 except observed during 02–03, April 2005.

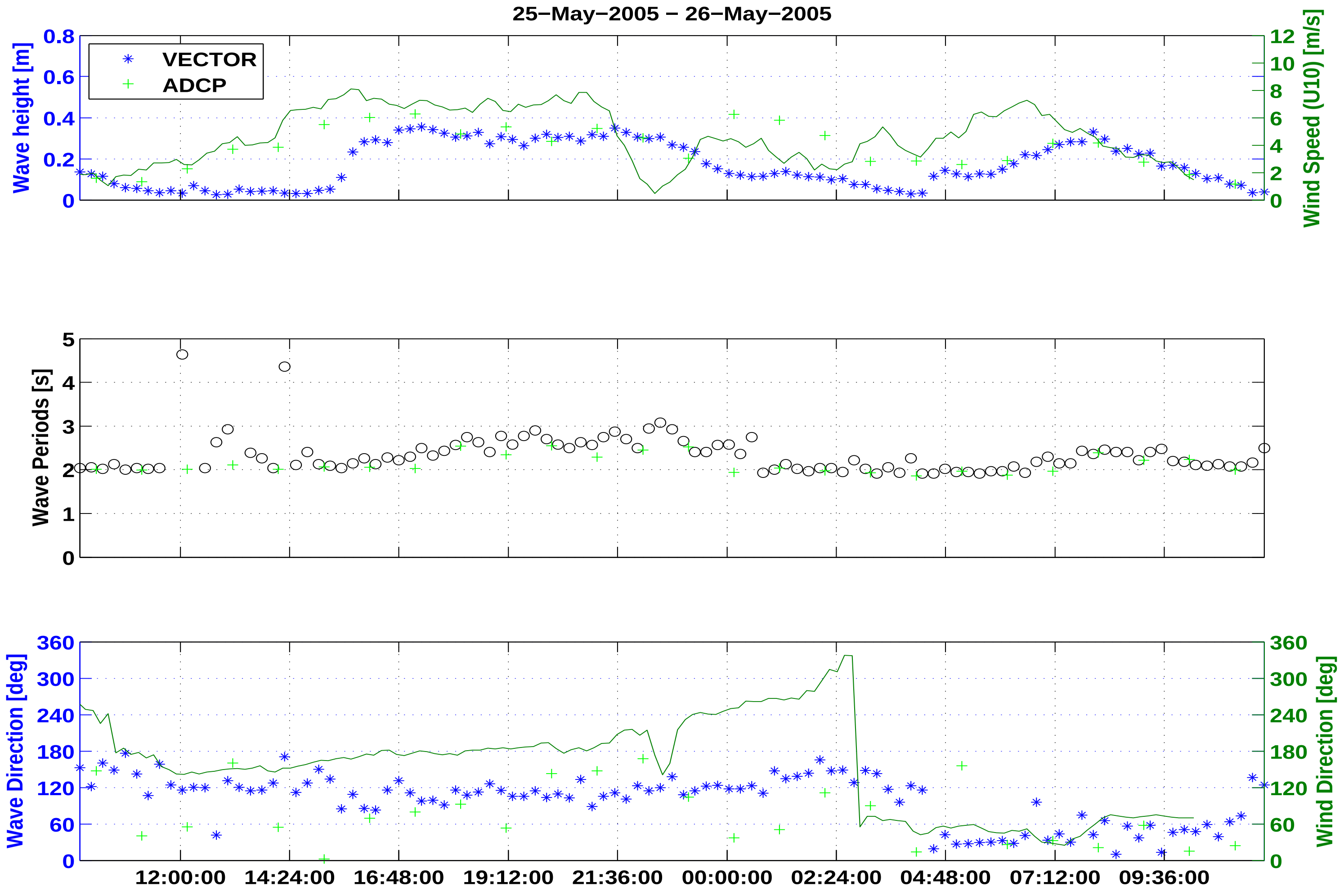

Fig. 43. Similar to Fig. 34 except observed during 25–26, May 2005.

# VITA

Keith Wade Dupuis

*Permanent Address*
2425 Date
Port Arthur, TX 77642
Email: kdupuis@gmail.com

*Educational Background:*

2004 B.S. in Marine Sciences, Texas A&M University at Galveston

2006 M.S. in Oceanography, Texas A&M University, College Station, TX